RICE UNIVERSITY

Teleseismic Imaging of the Crust and Upper Mantle in the Western United States

by

Kaijian Liu

A THESIS SUBMITTED
IN PARTIAL FULFILLMENT OF THE
REQUIREMENTS FOR THE DEGREE

Doctor of Philosophy

APPROVED, THESIS COMMITTEE:

Alan Levander, Carey Croneis Professor
Earth Science

Fenglin Niu, Professor
Earth Science

Cin-Ty A. Lee, Professor
Earth Science

David Alexander, Professor
Physics and Astronomy

HOUSTON, TEXAS

APRIL 2012

ABSTRACT

Teleseismic Imaging of the Crust and Upper Mantle in the Western United States

by

Kaijian Liu

High-resolution seismic images of lithospheric structures allow us to infer the tectonics that modified the lithosphere. We apply such methods to understand Cenozoic modification of the lithosphere by tectonic and magmatic processes in the tectonically active western United States. Using USArray Transportable and Flexible Array data, we present high-resolution images for three regions in this thesis. (1) In the Mendocino triple junction, we use a joint inversion of Rayleigh-wave dispersion data and receiver functions to obtain a new crust and upper Vs model to ~150km depth. The model shows four distinct, young lithosphere-asthenosphere boundary systems. A low-Vs anomaly beneath the Great Valley-Sierra Nevada reconciles existing slab window models with the mantle-wedge geochemical signatures in Coast Range volcanics, and explains the ~3 Myr delay of the onset of volcanism after slab removal. Uppermost mantle low velocities provide evidence for forearc mantle serpentinization extending along the Cascadia margin. (2) In the Colorado Plateau, a Rayleigh wave tomography model sheds light on the volcanism along the margins and plateau uplift. Strong upper mantle heterogeneity across the plateau edge results from the combined effect of a ~200-400 K temperature difference and ~1% partial melt. A ring of low velocities under the plateau periphery suggests that the rehydrated Proterozoic lithosphere is progressively removed by convective processes. Particularly, a high-Vs anomaly imaged

beneath the western plateau adds evidence for a downwelling/delamination hypothesis [*Levander et al*., 2011]. Thermo-chemical edge-driven convection causing localized lithospheric downwelling provides uplift along the margins and magmatic encroachment into the plateau center. (3) In the final study, we developed a 3-D teleseismic scattering wave imaging technique based on the Kirchhoff approximation and 3-D inverse Generalized Radon Transform. Synthetic tests demonstrate higher resolution imaging for continuous, irregular interfaces or localized scatterers, in comparison to conventional methods. Applied to the High Lava Plains dataset, the transmission coefficient structure shows a deepening Moho near 117.6°W and three negative events that correlate well with the Rayleigh wave low-Vs zones. Images made with the Mendocino data clearly show rapidly decreasing lithosphere-asthenosphere boundary depths from the subduction to transform regime.

ACKNOWLEDGMENTS

I am deeply indebted to my advisor, Dr. Alan Levander, for his close guidance, valuable advice, patient editing and helpful discussions throughout my PhD project in the past six years. I have benefited a lot from his extensive knowledge of seismology and tectonics, as well as his enthusiasm for geoscience. Without his great support and expertise, this thesis would not have been possible.

I would also like to thank my thesis committee Dr. Fenglin Niu, Dr. David Alexander, and Dr. Cin-Ty Lee for their constructive comments. I would like to give a special thanks to Fenglin for teaching me the surface wave code as a start to my CP project and to David who gave very detailed and insightful comments on my presentation and thesis.

I am also grateful for many amazing research resources shared in the seismology community. I greatly appreciate Don Forsyth, Yingjie Yang and Aibing Li for sharing the two-plane wave code, Robert Herrmann and Charles Ammon for the CPS package, and Shawn Larsen (LLNL) for the E3D code. For the MTJ project, I would thank Robert Porritt and Richard Allen for providing the ANT data, Yongbo Zhai for the CCP data, and Matt Fouch for the SKS splits. I also acknowledge Meghan Miller, Iain Bailey, and Mary Reid for their collaboration on the CP project. I would like to express my sincere gratitude to Aimin Cao, Yang He, Michael Bostock, Stephane Rondenay, and Fred Pearce for sharing part of their 2-D/3-D GRT work, and especially Brandon Schmandt for preprocessing the HLP data. I acknowledge the HLP group (Matt Fouch, David James, Chin-Wu Chen, Lara Wagner and Kevin Eagar etc.) for their field efforts and sharing the seismic results.

I would like to thank many colleagues at Rice for their discussion and support. Special thanks go to my officemates Sally Thurner and Jen Gabler for editing all my papers and my thesis. I enjoyed research discussions with them as well as many other STAR members such as Huafeng Liu, Imma Palomeras, Jeniffer Masy, Min Chen, Jianxiong Chen, Emily Chin, Tao Huang, and former STAR members Aimin Cao, Xin Cheng, Yang He, Max Bezada, Elizabeth Vanacore, Yongbo Zhai, and Xinling Wang.

The seismic data (USArray, FAME and HLP) used in this study were acquired from the IRIS DMC. This thesis work was supported by the NSF CMG Program (grant DMS-0620821), NSF EarthScope program (grant EAR-0844760, 0844741, 0642474, 0746379) and the Rice-BP HPC Graduate Fellowship.

Finally, I would like to thank my parents Tianwang Liu and Xiumei Zheng, my two younger brothers Kaibao Liu and Kaiyuan Liu and other family members for their love and unconditional support all the time. Special thanks to Fanping Kong for her support. I dedicate this thesis to my grandfather Mingtian Liu who passed away a month before my defense.

TABLE OF CONTENTS

Chapter 1 INTRODUCTION

1.1 Brief tectonic history and motivations

The complex crust and upper mantle in the tectonically active western United States (WUS) primarily results from Cenozoic modifications to the Paleozoic continental margin of North America [e.g., *Lipman*, 1992; *Lee et al.*, 2001; *Humphreys et al.*, 2003]. After Paleoproterozoic assembly by progressive accretion of island arc terranes [*Karlstrom and Humphreys*, 1998], the WUS continental lithosphere was significantly modified by a series of major volcanic-tectonic events, e.g., shortening, extension, rifting, uplift, and magmatism. Much of the deformation is related to the Farallon plate subduction beneath North America since ~150 Ma [*Humphreys et al*., 2003]. The rapid subduction and flattening of the Farallon slab controlled the widespread basement-cored uplift (crustal shortening and thickening) during the Laramide orogeny (~70-45 Ma). Slab flattening hydrated the base of the North American lithosphere during the Laramide [e.g., *Saleeby*, 2003; *Humphreys et al*., 2003; *English et al*., 2003], which depressed the peridotite solidus for subsequent melting [*Lee*, 2005]. It also caused an eastward sweep of arc volcanism starting from the trench [*Coney and Reynolds*, 1977; *Snyder et al*., 1976]. Large-scale volcanism and extension in the Basin and Range Province (BRP) and Rio Grande Rift (RGR) were triggered by post-subduction gravitational collapse and the ascent of hot asthenosphere after flat slab removal ~30 Ma [*Dickinson and Snyder*, 1978; *Humphreys*, 1995]. Since then, small-scale convection in the back arc and orogenic belt [e.g., *Hyndman et al*., 2005; *Humphreys*, 2009], along with dynamic mantle upwelling [e.g., *Liu et al*., 2010], have continued to modify the unstable

WUS lithosphere. In this thesis, my particular interest focuses on the western and eastern ends of the flat slab domain and its tectonic consequence.

In the westernmost US, near the Pacific coast, a remnant of the Farallon plate (the Juan de Fuca-Gorda plate) is still subducting beneath North America along the Cascadian subduction zone (Figure 1.1a). At the southern edge of subduction, the Mendocino triple junction (MTJ) formed the intersection of the Gorda, Pacific and North American plates ~25-29 Ma when the Pacific-Farallon ridge collided with the trench [*Atwater*, 1970]. The northwestward migration of the MTJ, forming the San Andreas Fault, is the progressive subduction-to-transform transition, which has profoundly modified the western margin of the WUS. The migration of the triple junction created two distinct, Quaternary volcanic systems (Cascade and Coast Range volcanic centers) and opened a slab window structure [*Dickinson and Snyder*, 1979] with very complicated lithosphere-asthenosphere boundary (LAB) systems (e.g., mantle wedge, slab-gap, oceanic slab). The relation between the young lithospheric evolution and the surface volcanism is still unclear. Moreover, the pathways of the asthenosphere filling the slab-free region are still debated, with two mantle sources identified: (1) subcontinental [e.g., *Johnson ad O'Neil*, 1984; *Liu and Furlong*, 1992; *Whitlock et al*., 2001], or (2) suboceanic [e.g., *Cole and Basu*, 1995; *Zandt and Humphreys*, 2008]. The MTJ region provides a natural laboratory to examine lithospheric evolution associated with slab removal in an active tectonic setting.

Along the eastern margin of the WUS, west of the sloping Great Plains, magmatism and extension from the extended BRP and RGR are currently migrating into the relatively

undeformed Colorado Plateau (CP) across its borders [*Roy et al*., 2009]. The CP is a tectonically stable physiographic province west of the Rocky Mountain front (easternmost extent of slab flattening), the source of whose high elevation (1.8-2 km) remains a topic of debate (Figure 1.1a). A variety of CP uplift mechanisms have been proposed in the past, including buoyancy sources from 1) thermal expansion [*Thompson and Zoback*, 1979], 2) lithospheric thinning [*Bird*, 1979; *Spencer*, 1996; *Lastowka et al*., 2001], and 3) crustal thickening [*Morgan and Swanberg*, 1985; *McQuarrie and Chase*, 2000]. The debated uplift mechanism has motivated recent geodynamic and seismologic efforts, such as the dynamic uplift [*Moucha et al*., 2008, 2009; *Liu et al*., 2010], thermal expansion by side heating [*Roy et al*., 2009], as well as small-scale convection in forms of either edge-driven convection [*van Wijk et al*., 2008, 2010] or delamination-style downwelling [*Levander et al*., 2011]. Another question has been raised regarding the stability of the CP. It may remain intact due to its depleted, less dense Proterozoic lithospheric core [*Lee et al.*, 2001], or it may become unstable from the base and sides of the lithosphere. Evidence of late Cenozoic magmatism and uplift along the margins suggests future destabilization of the plateau may occur by convective removal of the lithospheric core either by edge erosion [*van Wijk et al*., 2008, 2010] or a series of 'dripping' events [*Levander et al*., 2011; *Obrebski et al*., 2011], or both.

In both the MTJ and CP tectonic regions, active source profiles and body-wave tomography were completed prior to this thesis work, but are limited to either crustal or a deeper upper mantle scale, respectively. Higher-resolution seismic images with better vertical constraints (e.g., from surface waves and receiver functions) of the lower crust and shallow upper mantle

are needed to examine the effects of the tectonic and magmatic history on the modern lithospheric/sub-lithospheric structure in the WUS (Figure 1.1a).

1.2 USArray and new opportunities

The deployment of the USArray Transportable Array (TA) with average station spacing of ~70 km began in the western United States in 2004. The TA network, consisting of ~400 broadband seismographs with an average residence time of ~1.8-2 years per station (Figure 1.1b), moves eastward to investigate the North American lithosphere at the continental scale [e.g., *Levander et al*., 1999, *Ekstrom et al*., 1999, *Meltzer et al*., 1999]. By the end of 2011, the TA had moved out of the WUS region discussed in this thesis. The TA network has both high-quality broadband data and a regular geometry, which provide global seismologists unparalleled opportunities to construct more detailed crust and upper mantle images, leading to better knowledge of the lithospheric evolution of the WUS. Combined with the regional experiments, e.g., the Flexible Array Mendocino Experiment (FAME) and High Lava Plains (HLP) seismic experiments (Figure 1.1b), the USArray data will further improve the resolution of images with various tomographic and converted wave imaging techniques.

A number of body wave [e.g., *Burdick et al.*, 2008, 2010; *Sigloch et al*., 2008; *Sigloch*, 2011; *Roth et al.*, 2008; *Obrebski et al.*, 2010, 2011; *Schmandt and Humphreys*, 2010; *Tian et al*., 2011; *James et al.*, 2011], surface wave [e.g., *Yang and Ritzwoller*, 2008; *Pollitz*, 2008 *Pollitz and Snoke*, 2010; *Lin et al*., 2009; *Lin and Ritzwoller*, 2011] and ambient noise [e.g., *Bensen et al*., 2009; *Moschetti et al*., 2010] tomography models have been published using the USArray data. These new tomography results provide unprecedented, high-resolution P-wave velocity (Vp) and/or S-wave velocity (Vs) volumes of the WUS crust and mantle.

Meanwhile, scattered wave imaging using the receiver function (RF) technique [*Langston*, 1979] with USArray data has also greatly improved the quality of the discontinuity imaging from the Moho and LAB to the transition zone discontinuities [e.g., *Kumar et al.*, 2005; *Cao and Levander*, 2010; *Pavlis*, 2011; *Levander et al*., 2011; *Levander and Miller*, submitted]. Resulting from the USArray and Flexible Array data, these new models, together with the geodynamic modeling, have significantly improved our understanding of the large lithospheric heterogeneities and instabilities beneath the WUS. For example, widespread small-scale convective processes (edge-driven convection, lithospheric drip, plumes etc.) have been proposed in many recent studies. These include (1) the edge-driven convective processes in form of fast velocity anomalies beneath the RGR-western Great Plains [*Gao et al*., 2004], the Great Basin-CP boundary [*Sine et al*., 2008], and (2) the lithospheric drips beneath the southern Sierra Nevada [*Zandt et al*., 2004], Wallowa Mountains [*Hale et al.*, 2005], Great Basin [*West et al.*, 2009] and western CP [*Levander et al*., 2011].

1.3 The present study

Adding to the growing set of high-resolution images using USArray data, we present better resolved seismic images for three key regions in the tectonically and magmatically active WUS: the MTJ in the west, the CP in the east, and the HLP in the Cascadia backarc (Figure 1.1). Vertical resolution, especially in the shallow mantle, is greatly improved using the surface wave tomography and/or the scattered wave data in this study. We focus on these representative regions to better understand how deformation and magmatism have altered the continental lithosphere in the WUS. Furthermore, although the seismology community has made much progress in obtaining high-resolution seismic images of the WUS, we developed a new teleseismic imaging method, presented in Chapter 4, to image more complicated

structures that are poorly resolved by the existing methods, which we apply to the MTJ and HLP data. This method provides interface images that complement tomography methods described in Chapter 2 and 3. Scattered waves play a key role in teleseismic imaging due to the deployment of increasingly dense broadband seismograph arrays. The widely used common conversion point (CCP) stacking of RFs to determine structure is limited due to its formulation for perfectly layered media, which ignores the effects of dipping layers and diffractions from 3-D heterogeneities. At the end of this chapter, we discuss the method's advantages, particularly the full use of three component data, as well as the resolution limitations caused by incomplete illumination in earthquake seismology.

These three chapters (2, 3, 4) are a collection of several reformatted papers published or submitted during my thesis work. The joint inversion study in the MTJ region (Chapter 2) is based on an *EPSL* paper [*Liu et al*., 2012] as well as the unpublished surface wave data results and phase velocity maps. Chapter 3 is based on the Rayleigh wave tomography study on the CP published in G^3 [*Liu et al*., 2011]. Some of these results are included as essential elements in three other papers [*Levander et al., Nature*, 2011; *Bailey et al., JGR*, 2012; *Reid et al., Geolog*y, 2012]. The last chapter is based on the 3-D Kirchhoff migration manuscript [*Liu and Levander*, 2012] submitted to *GJI*.

Figure 1.1 (a) Tectonic features of the western United States on topography (unit: km). In the western margin, the MTJ marks the intersection of three plates: the Juan de Fuca-Gorda, Pacific and North America. North of it, the Juan de Fuca-Gorda plate is subducting beneath the North American plate along the Cascadian margin. In its south, the strike-slip boundary between the Pacific and North America dominates along the San Andreas Fault. The Colorado Plateau is in west of the Rocky Mountain Front and tilted Great Plains, surrounded by the extended Basin and Range Province in the west and south, the Rio Grande Rift in the southeast, and the Southern Rocky Mountains in the north and northeast. MFZ=Mendocino Fracture Zone, MTJ=Mendocino triple junction, GV=Great Valley, SN=Sierra Nevada, HLP=High Lava Plains. (b) Distribution of USArray and other flexible array stations. The black, red and green boxes mark the regional studies in this thesis.

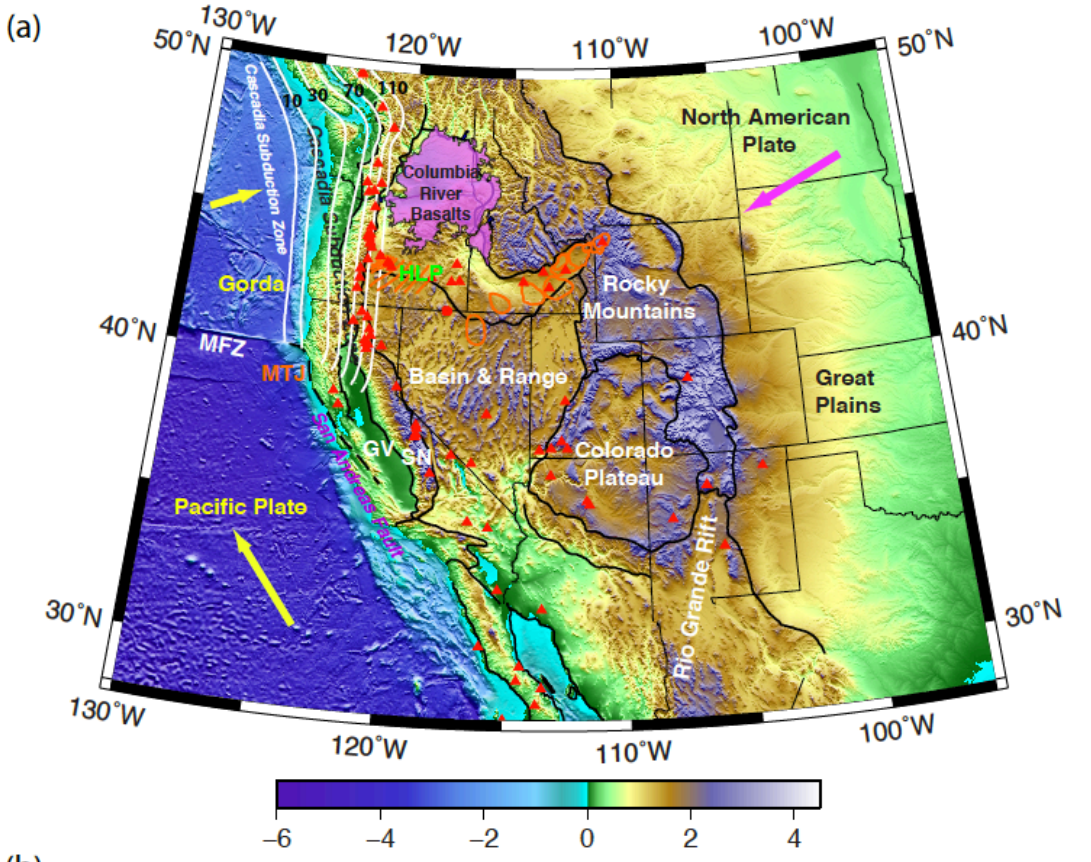
(a)
130°W
120°W
110°W
100°W
50°N
40°N
30°N
Cascadia Subduction Zone
10
30
70
110
Columbia River Basalts
North American Plate
Gorda
HLP
Rocky Mountains
MFZ
MTJ
Basin & Range
Great Plains
GV
SN
Colorado Plateau
Pacific Plate
Rio Grande Rift
−6
−4
−2
0
2
4

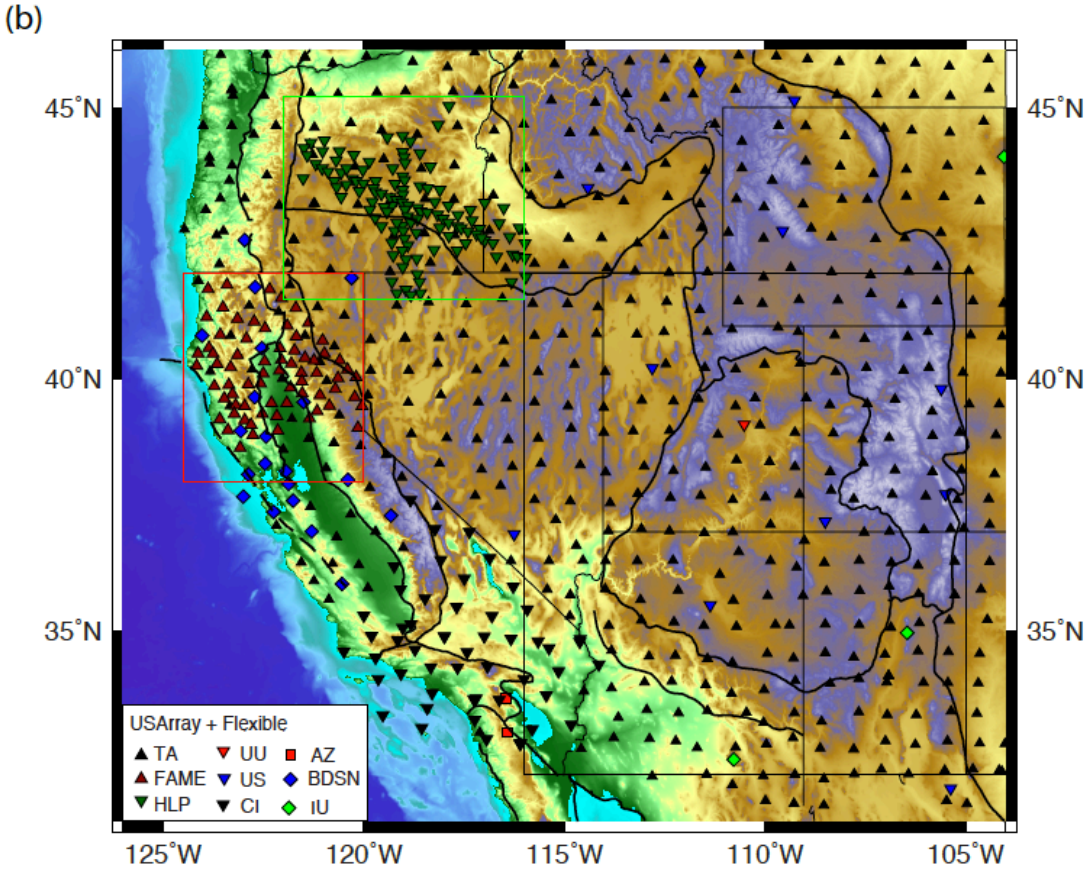
(b)
45°N
40°N
35°N
125°W
120°W
115°W
110°W
105°W
USArray + Flexible
TA
FAME
HLP
UU
US
CI
AZ
BDSN
IU

Chapter 2 ASTHENOSPHERIC FLOW AND LITHOSPHERIC EVOLUTION NEAR THE MENDOCINO TRIPLE JUNCTION: RAYLEIGH WAVE TOMOGRAPHY AND JOINT INVERSION OF DISPERSION CURVES AND PS RECEIVER FUNCTIONS

The migration of the Mendocino Triple Junction (MTJ) in northern California creates a complicated LAB system at shallow depths (<60 km), following the progressive transition from Cascadia subduction to San Andreas transform motion. It provides a natural laboratory to examine lithospheric evolution associated with slab removal in an active tectonic setting. However, pathways of the asthenospheric sources that fill the slab-free region created by the triple junction migration remain unclear. Previous active source profiles and body-wave tomography are limited to either crustal or a deeper upper mantle scale, respectively. In this study, we analyze the fundamental-mode Rayleigh wave phase velocities from finite-frequency Rayleigh wave tomography, and present a 3-D Vs model from joint inversion of ambient noise (8-30 s) and ballistic Rayleigh wave dispersion curves (22-100 s), as well as Ps RFs, using 111 stations from the FAME, USArray TA and the Berkeley Digital Seismic Network (BDSN). In the crust, we have observed the low-Vs Franciscan Complex in the Coast Ranges and the relatively high-Vs Great Valley ophiolite abutting the low-Vs Sierran basement. The low-Vs uppermost mantle imaged near the sudden steepening of the subducted oceanic slab extends seismic evidence for forearc mantle serpentinization further south along the Cascadia margin. In addition to the Gorda asthenosphere, the joint inversion Vs model further identifies three other young asthenospheres resulting from different partial melting mechanisms. Northward motion of the MTJ causes asthenospheric flow both from under the Gorda plate and from the cooling former mantle wedge left under the Great Valley

and Sierra Nevada, imaged from the joint inversion as a relatively deep (>75 km) low-Vs anomaly. These two mantle flows appear to begin mixing ~100 km south of the southern edge of the Gorda plate in the slab window region. We speculate that the latter provides the wedge-type geochemical signature seen in the Coast Range volcanic rocks, reconciling slab window models and volcanic geochemistry. This 'staggered' upwelling model proposed here also explains the ~3 Myr delay in onset of volcanism after triple junction migration.

2.1 Introduction

The MTJ is a transform-transform-trench triple junction forming the intersection of the Pacific, North American and Gorda plates in northern California [*Dickinson and Snyder*, 1979; *Furlong and Schwartz*, 2004] (Figure 2.1). It was formed ~25-29 Ma by the impingement of the Pacific-Farallon ridge on the North American trench, initiating San Andreas fault (SAF) strike-slip motion [*Atwater*, 1970]. North of the MTJ, the subduction of the young Gorda plate beneath North America forms the southern terminus of the Cascadia subduction zone. The northwestward migration of the MTJ, resulting in the progressive replacement of the subduction zone by the transform margin, has profoundly altered the lithospheric structure of the western North American plate boundary through a variety of tectonic and magmatic processes [*Dickinson*, 1997]. The MTJ region has two distinct volcanic systems: the southernmost Cascade Quaternary volcanic centers (e.g. Mount Shasta and Lassen Peak), resulting from mantle wedge melting above the Gorda plate [*Leeman et al.*, 2005] and the northern Coast Range volcanic system, consisting of isolated volcanic centers with northward decreasing ages aligned along the strike of the range, the youngest being the Clear Lake volcanic fields (~2-0.1 Ma) [*Dickinson*, 1997; *Furlong and Schwartz*, 2004; *Johnson and O'Neil*, 1984]. Northern coastal California near the MTJ is the site of

subduction, accretionary wedge formation, thrusting, and strike-slip faults. Basement rocks primarily consist of the Mesozoic-Cenozoic Franciscan Complex in the Coast Ranges, a forearc basin with an ophiolitic basement under thick sediments in the Great Valley [*Godfrey and Klemperer,* 1998; *Godfrey et al*., 1997], and the Sierra Nevada plutonic and Cascadia volcanic arc rocks (Figure 2.1). The Franciscan Complex is mainly divided into three parallel metasedimentary belts with increasing age and metamorphic grade inland [*Blake et al*., 1985] before the thrust faulting contact with the Klamath terrane [*Beaudoin et al.,* 1996, 1998].

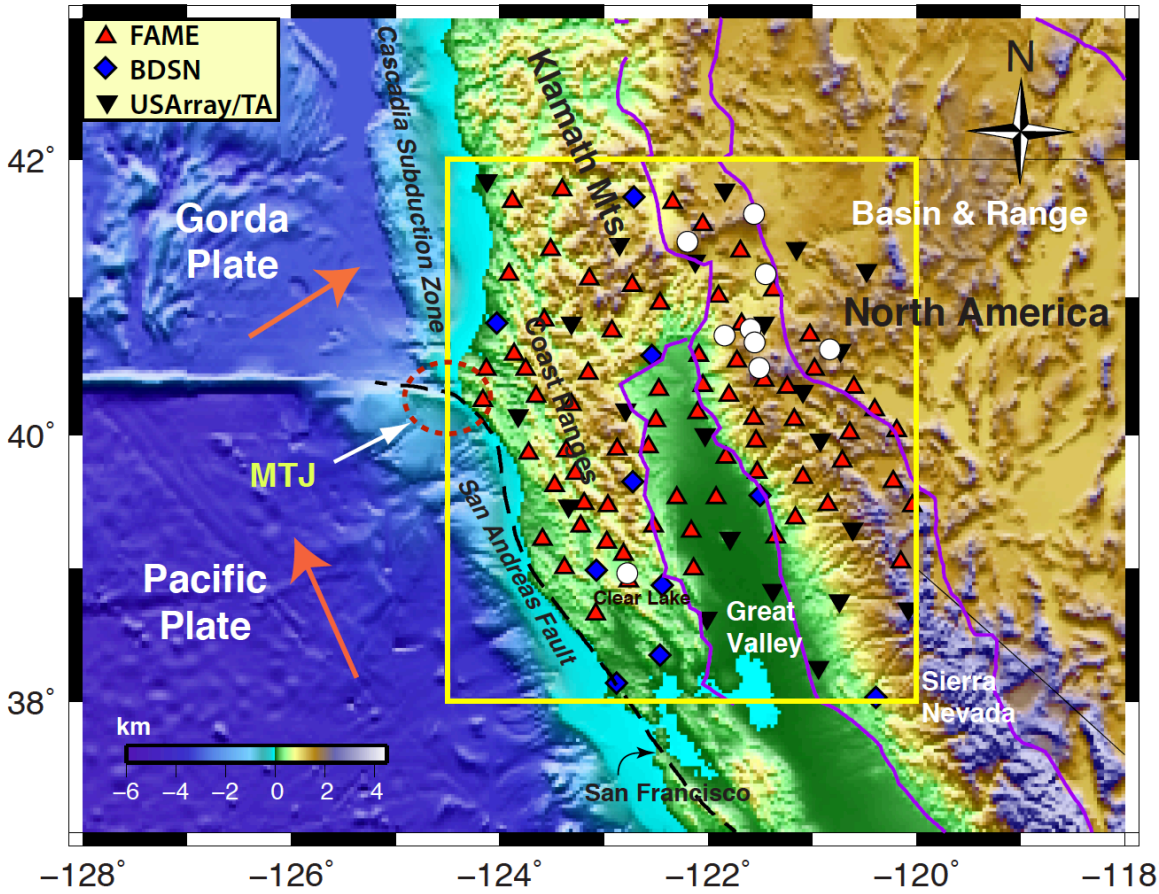

Figure 2.1 Study region (yellow box) with topography and principal tectonic features. We analyzed broadband data from 75 FAME stations (red triangles), 22 USArray/TA stations (dark inverse triangles), and 14 Berkeley Digital Seismic Network (BDSN) stations (blue diamonds). Volcanoes are plotted as white dots, including Clear Lake, in the Coast Ranges, and Mt. Shasta and Lassen Peak in the Cascade Ranges. Dark dashed line shows the SAF along the Pacific-North American plate boundary. Purple lines mark the major tectonic boundaries. Orange arrows indicate Pacific and Gorda plate motions relative to North America.

The northwestward migrating MTJ leaves in its wake a lithospheric gap at the southern edge of the Gorda plate (SEDGE) [*Dickinson and Snyder*, 1979; *Furlong and Schwartz*, 2004; *Levander et al.*, 1998; *Liu and Furlong*, 1992], thought to be filled by asthenospheric flow, the subject of this chapter. Coast Range volcanism and toroidal mantle flow are attributed to flow into the gap [*Eakin et al.*, 2010; *Zandt and Humphreys*, 2008]. Evidence supporting this model includes surface heat flow [*Lachenbruch and Sass*, 1980], patterns of volcanism [*Dickinson*, 1997], active and passive source seismic images [*Beaudoin et al*., 1996, 1998; *Benz et al*., 1992; *Levander et al*., 1998; *Zhai*, 2010], and geodynamic modeling [*Liu and Furlong*, 1992; *Zandt and Furlong*, 1982]. The origin of the slab window asthenosphere and the flow paths into the gap following slab removal are debated [*Cole and Basu*, 1995; *Hole et al.*, 1998; *Schmitt et al.*, 2006; *Whitlock et al.*, 2001]. Previous mantle upwelling models fall into two categories, involving either subcontinental [*Johnson and O'Neil*, 1984; *Liu and Furlong*, 1992; *Schmitt et al.*, 2006; *Whitlock et al.*, 2001] or suboceanic [*Cole and Basu*, 1995; *Zandt and Humphreys*, 2008; *Zhai*, 2010] sources.

Seismic converted wave imaging, tomography, and SKS split times can be used to identify the slab window structure, asthenospheric seismic velocities, and the directions of mantle flow in the MTJ region. In this study, we constructed a 3-D Vs model by the joint inversion of Ps RFs and fundamental-mode Rayleigh wave dispersion data (8-100 s) from the EarthScope flexible and transportable arrays (Figure 2.1). The ambient noise data are mainly sensitive to crustal-scale structure, while vertical resolution of ballistic Rayleigh wave dispersion data go to lower crust and upper mantle. Both datasets provide constraints on the absolute value of shear velocity. In contrast, the RFs provide complementary constraint on

the impedance contrast, instead of absolute Vs value. Thus, the joint inversion provides better vertical resolution of upper mantle structures in the resolution gap, which exists from roughly the Moho to the asthenosphere, between teleseismic body-wave tomography [*Benz et al.*, 1992; *Obrebski et al.*, 2010; *Schmandt and Humphreys*, 2010] and active seismic studies [*Beaudoin et al.*, 1996, 1998; *Henstock et al*., 1997; *Levander et al*., 1998].

2.2 FAME and USArray datasets

We used data from the FAME network, which consists of 75 broadband seismic stations deployed in northern California from July 2007 to June 2009. Additionally, we incorporated data from 22 USArray TA and 14 BDSN stations, as they have temporal overlap with the FAME experiment (Figure 2.1). Using a total of 111 stations, we first measured fundamental-mode Rayleigh wave phase velocities (22-100 s). The resulting phase velocities were combined with short-periods (8-30 s) from an ambient noise tomography (ANT) study [*Porritt et al.*, 2011], yielding broader band surface wave dispersion curves (8-100 s). We inverted for the isotropic Vs structure using the joint inversion of the combined dispersion curves and the Ps RFs [*Zhai*, 2010] made with data from the same stations.

2.2.1 Ballistic Rayleigh wave phase velocity (22-100 s)

We use 224 teleseismic earthquakes with epicentral distance between 30° and 120°, magnitude > 5.5 and depths < 70 km (Figure 2.2a, b). To account for the nonplanar energy in the fundamental-mode Rayleigh wavefield caused by multipathing or small-scale scattering, we applied the modified two-plane wave technique [*Forsyth and Li*, 2005; *Liu et al*., 2011; *Yang and Forsyth*, 2006b], which incorporates finite-frequency sensitivity kernels for both amplitude and phase. Here, the recorded wavefield is represented approximately by the sum

of two interfering plane waves. We inverted the Rayleigh wave phase velocities for 13 frequency bands from 22 to 100 s (Figure 2.2b) based on a grid of 0.25°×0.25° near the MTJ region. The combination of the FAME, USArray/TA and the BDSN stations provides dense enough coverage to resolve the relatively short wavelength phase velocity variations. We will provide details of surface wave data analysis and phase velocity inversion and discuss the depth-dependent vertical resolution and finite-frequency effect in section 2.4.

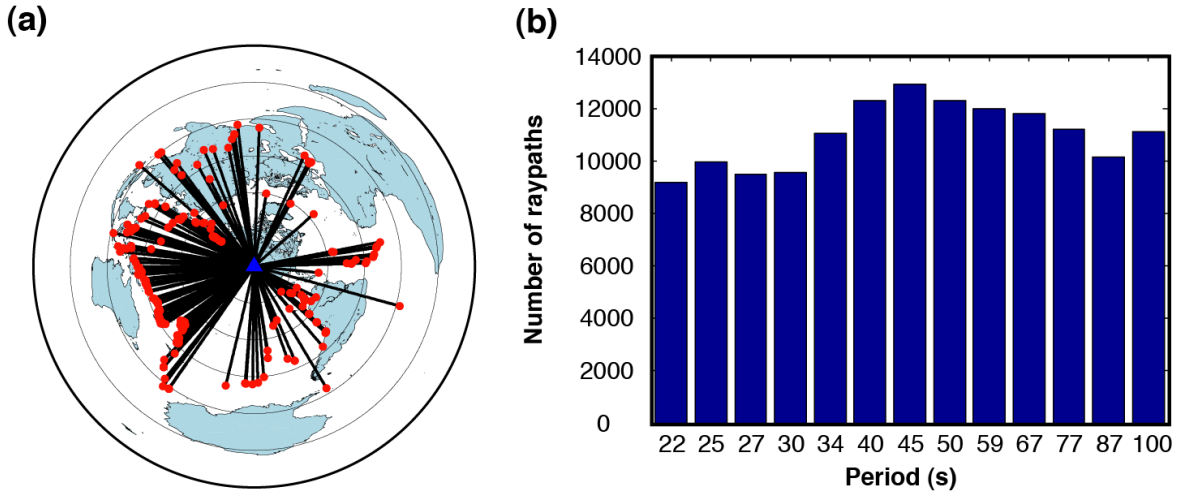

Figure 2.2 (a) Azimuthal and distance distribution of the 224 teleseismic events (red dots) for the finite-frequency Rayleigh wave tomography. (b). Number of raypaths for each period (frequency) band from 22 to 100 s in the surface wave study.

2.2.2 Ambient noise dispersion data (8-30 s)

Ambient noise tomography computes the cross-correlation waveform of seismic noise between station pairs as an estimate of the Green's functions to extract the inter-station phase [*Bensen et al.*, 2007; *Shapiro et al.*, 2005; *Snieder*, 2004; *Yao et al.*, 2006]. The ANT provides shorter-period dispersion data (8-30 s) than the ballistic earthquake tomography described above, which greatly increases the study's sensitivity to crustal Vs [*Porritt et al.*, 2011]. In the overlapping period range (22-30 s), there is good consistency between the ballistic and ANT phase velocities (see Figure 2.11).

2.2.3 Ps receiver function

We include the Ps RFs (1 and 2 Hz), generated using FAME data [*Zhai*, 2010], in a joint phase velocity/RF inversion to provide a stronger constraint on lithospheric discontinuities. The station-gather RFs were made from 186 teleseismic events ($35°\leq\Delta\leq90°$, Mw>5.7) using time-domain iterative deconvolution technique [*Ligorria and Ammon*, 1999]. In our joint inversion, we selected two overlapping frequency band RFs with hi-cut frequencies of 1 and 2 Hz. The RFs increase sensitivity to the underlying discontinuity structure, while use of two different frequencies improves our ability to differentiate between first order discontinuities and Vs gradients, which both cause P-to-S conversions [*Julia et al.*, 2000]. To enhance the signal-to-noise ratio, we divided the RFs under each station into three groups with different ray parameters (<0.05 s/km; 0.05-0.06 s/km; >0.06 s/km). After the Ps time move-out correction [*Rondenay*, 2009] was applied and assuming the 1-D background Tectonic North America (TNA) shear model [*Grand and Helmberger*, 1984], we stacked the three RF groups individually at the central ray parameters of 0.045, 0.055 and 0.065 s/km, as well as collectively at 0.05 s/km (Figure 2.3a). This stacking reduces sensitivity to deep discontinuities and crustal reverberations while enhancing the shallow conversion signals; therefore, we used short time windows from -5 to 10 s (equivalent to ~100 km depth) for both RF bands (Figure 2.3a and 2.4). The short windows prevent modeling multiple reflections. Crustal multiples are poorly predicted by simple 1-D models in the presence of rapid crustal thickness changes in both coast normal and coast parallel directions. The significant signals (Moho and LAB) are contained within the first 10 seconds after P, since LAB depths in this region are typically <100 km [*Li et al*., 2007; *Zhai*, 2010].

2.3 Joint inversion method

To reduce the nonuniqueness of the Vs inversion from each single dataset, we jointly invert the Vs structure beneath each station from the three independent observations (e.g., Figure 2.3): (1) 22-100 s phase velocity from Rayleigh wave tomography, (2) 8-30 s phase velocity from ANT [*Porritt et al.*, 2011], and (3) Ps RFs at low (1 Hz) and high (2 Hz) frequency bands [Zhai, 2010]. The dispersion curves from the first two observations provide complementary constraint on the absolute Vs from the shallow crust to the upper mantle, while the Ps RFs are primarily sensitive to the shear impedance variations with depth. The combined constraints significantly decrease the nonuniqueness of the Vs inversion, and thus improve the model reliability for the crust and upper mantle. The joint inversion also helps refine Moho and LAB depth estimates in regions of ambiguity in the RF images.

We used the *Computer Programs in Seismology* package [*Herrmann and Ammon*, 2002] to invert the 1-D Vs models beneath the 111 stations (Figure 2.3). We modified the cost function here to include all three datasets with assigned weight for the joint inversion:

$$\frac{1-p}{N_{rf}N_{pts}}\sum_{i=1}^{N_{rf}}\sum_{j=1}^{N_{pts}}\left\|\varepsilon_{ij}^{rf}\right\|^2+\frac{p}{N_{dsp}}\left\{w_{RWT}\sum_{i=1}^{N_{RWT}}\left\|\varepsilon_i^{RWT}\right\|^2+w_{ANT}\sum_{i=1}^{N_{ANT}}\left\|\varepsilon_i^{ANT}\right\|^2\right\} \tag{2.1}$$

where $\varepsilon_i \equiv \left(d_i^{OBS}-d_i^{PRE}\right)/\sigma_i$ is the relative residual between the observed and synthetic data, N_{rf}, N_{dsp}, N_{RWT}, N_{ANT} are the total numbers of RFs, periods at which dispersion was measured, ballistic phase and ANT phase velocities, respectively. N_{pts} is the total number of sampling points in each RF, and p is the influence factor controlling the constraining weight given to the RF and dispersion data (Figure 2.4a). In order to avoid overemphasis of the ANT data due to closer period sampling, we assigned different weights to the dispersion data from

earthquake tomography and ANT analysis in the form of $w_i = N_{dsp}/2N_i$ (*i*=*RWT*, *ANT*). 30 iterations were used for the nonlinear inversion for the Vs model starting from the TNA model with no *a priori* crustal structure (Figure 2.3b). A slight increase of the weight term at the Moho depth estimated from the RFs allowed the possibility of large velocity variations under smoothing regularization. If the *a priori* Moho depth differs greatly from the true model, the iterative inversion will search for the true depth. The joint inversion also helps to improve the Moho and LAB depth estimates with respect to those made from RFs alone.

After completion of the station-by-station joint inversion, the 1-D Vs profiles were collected into a 3-D volume and interpolated onto a regular grid. Although the interpolation smoothes out sharp velocity changes, the lateral resolution in the 3-D volume is as good as the station spacing (~35km) allows. The horizontal resolution is controlled by a number of factors, including the wavelengths of the surface waves used in the tomography, the assumption that all the signals can be described by two-plane waves (resolution estimated as inter-station spacing of ~35 km for periods <40 s) [*Yang et al*., 2008], and the 1-D inversion. Vertical resolution is controlled by a combination of the Rayleigh wave's vertical averaging of velocity, the RF's ability to identify sharp gradients, and the weight given to each in the inversion (Figure 2.4a). For the dispersion data, the constraint on the absolute Vs at different periods decays with depth, with the sensitivity peaks located at depths of ~⅓ wavelength [e.g., *Liu et al.*, 2011]. The RF's vertical resolution is no better than ¼ wavelength; therefore, a 1 Hz shear wave at the Moho would be unable to distinguish between an impedance (Vs times density) gradient occurring over about 1 km and a step in impedance.

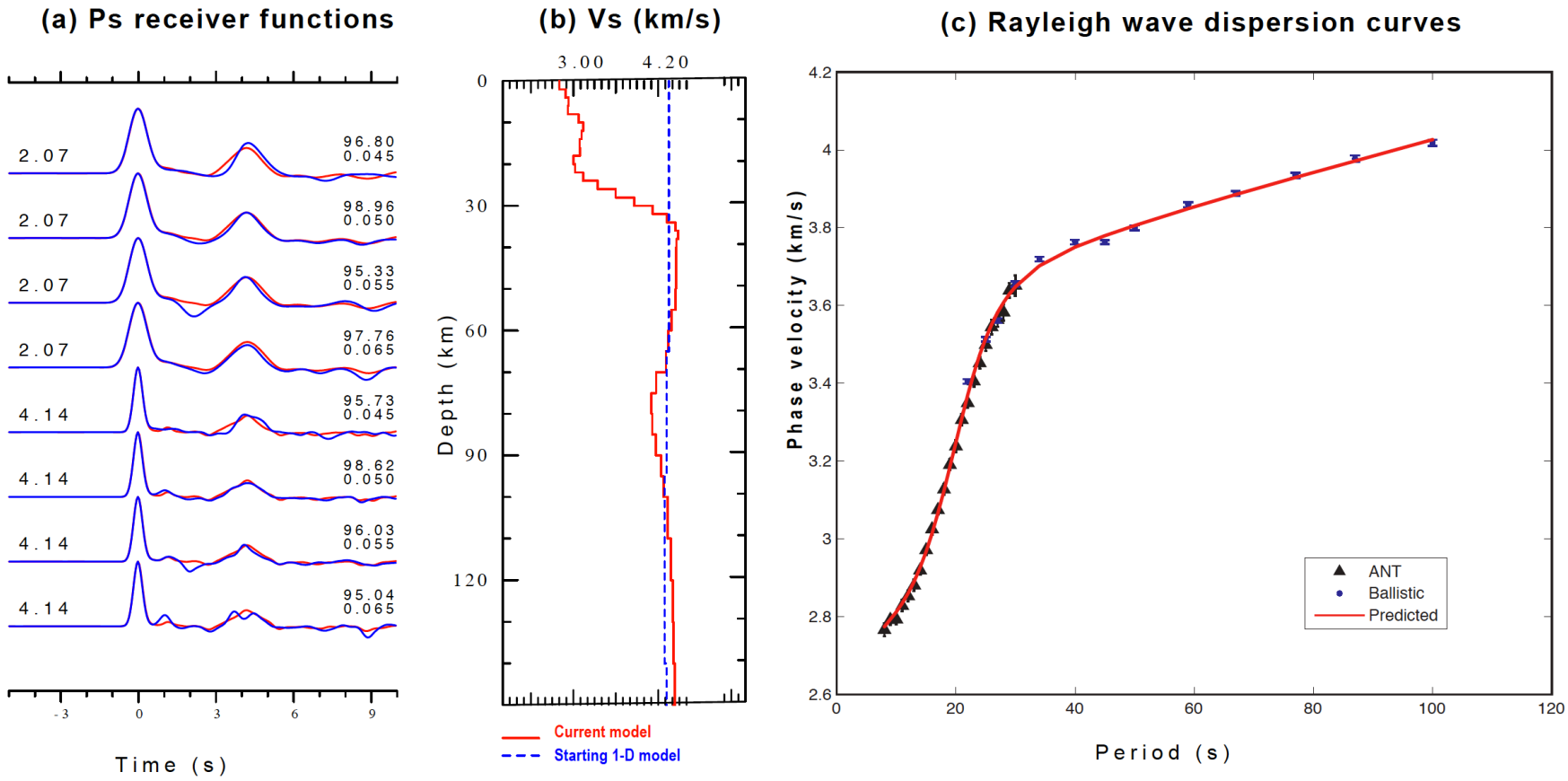

Figure 2.3 One example of a Rayleigh wave-RF joint inversion at station XQ.ME39. (a) We use 1 and 2 Hz (corresponding Gaussian widths of 2.07 and 4.14, respectively) Ps RFs binned at 0.045, 0.050, 0.055 and 0.065 s/km. Red and blue are the predicted and observed RFs, respectively. Top four traces are the 1 Hz RFs, and bottom four are the 2 Hz RFs. Each trace includes Gaussian filter parameters on the left, and percentage of model fit and ray parameter on the right. (b) The starting Vs model for the joint inversion is a constant velocity using the uppermost mantle velocity from the TNA model (dashed blue line) with no *a priori* information for the crustal thickness and velocities. Red line is the final Vs model after 30 iterations. (c) Both ANT (dark triangles) and ballistic (blue dots) Rayleigh wave phase velocities are used in the joint inversion, while the predicted dispersion curve (red) is calculated from the final Vs model from (b).

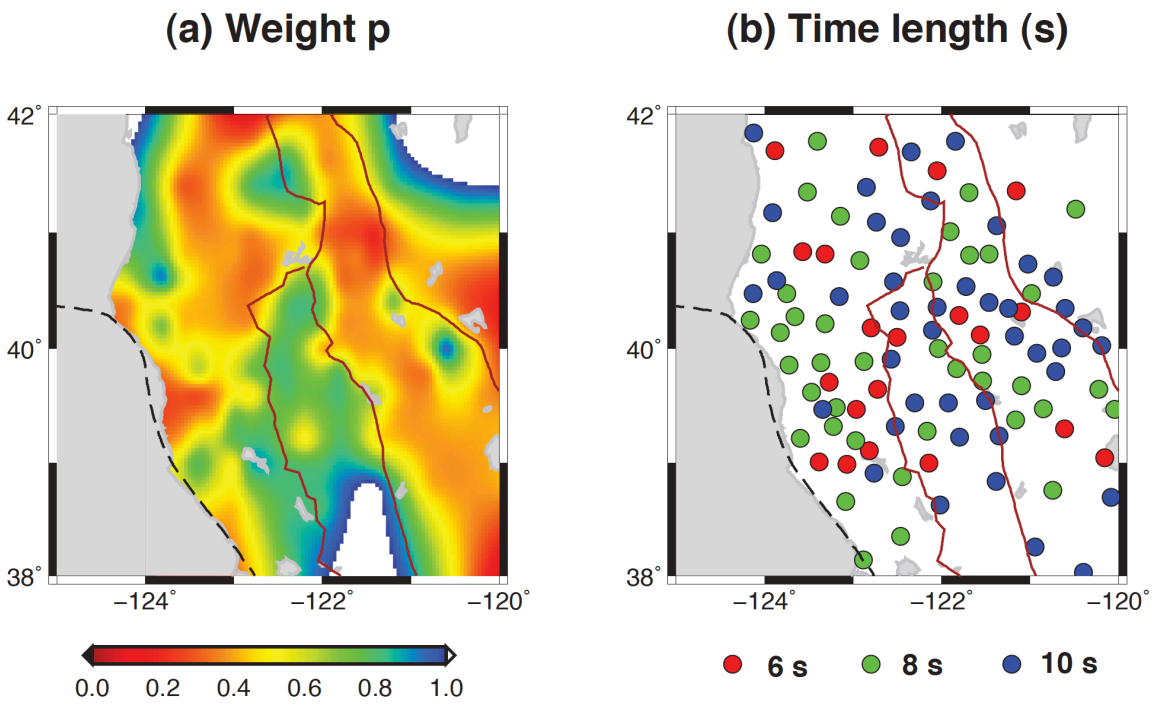

Figure 2.4 (a) Weight parameter p (0-1) used for the joint inversion; (b) Length of time window after direct P wave arrivals in the RFs at each station.

2.4 Finite-frequency Rayleigh wave tomography

2.4.1 Surface wave data processing

We use a total of 224 teleseismic ($30° \leq \Delta \leq 120°$) earthquakes with magnitude ≥ 5.5 and foci ≤ 70 km (Figure 2.2). The dense station coverage (~35 km) and good azimuthal distribution of sources (Figure 2.2) provide an unprecedented opportunity to resolve the lateral variation of phase velocity within the 5°×5° MTJ region. Using a total of 111 stations, we extracted the fundamental-mode Rayleigh wave phases and amplitudes from the vertical components centered at thirteen period bands (22, 25, 27, 30, 34, 40, 45, 50, 59, 67, 77, 87 and 100 s). The surface waveforms below 22 s are too complicated to be simply represented by a two-plane-wave approximation used in this study.

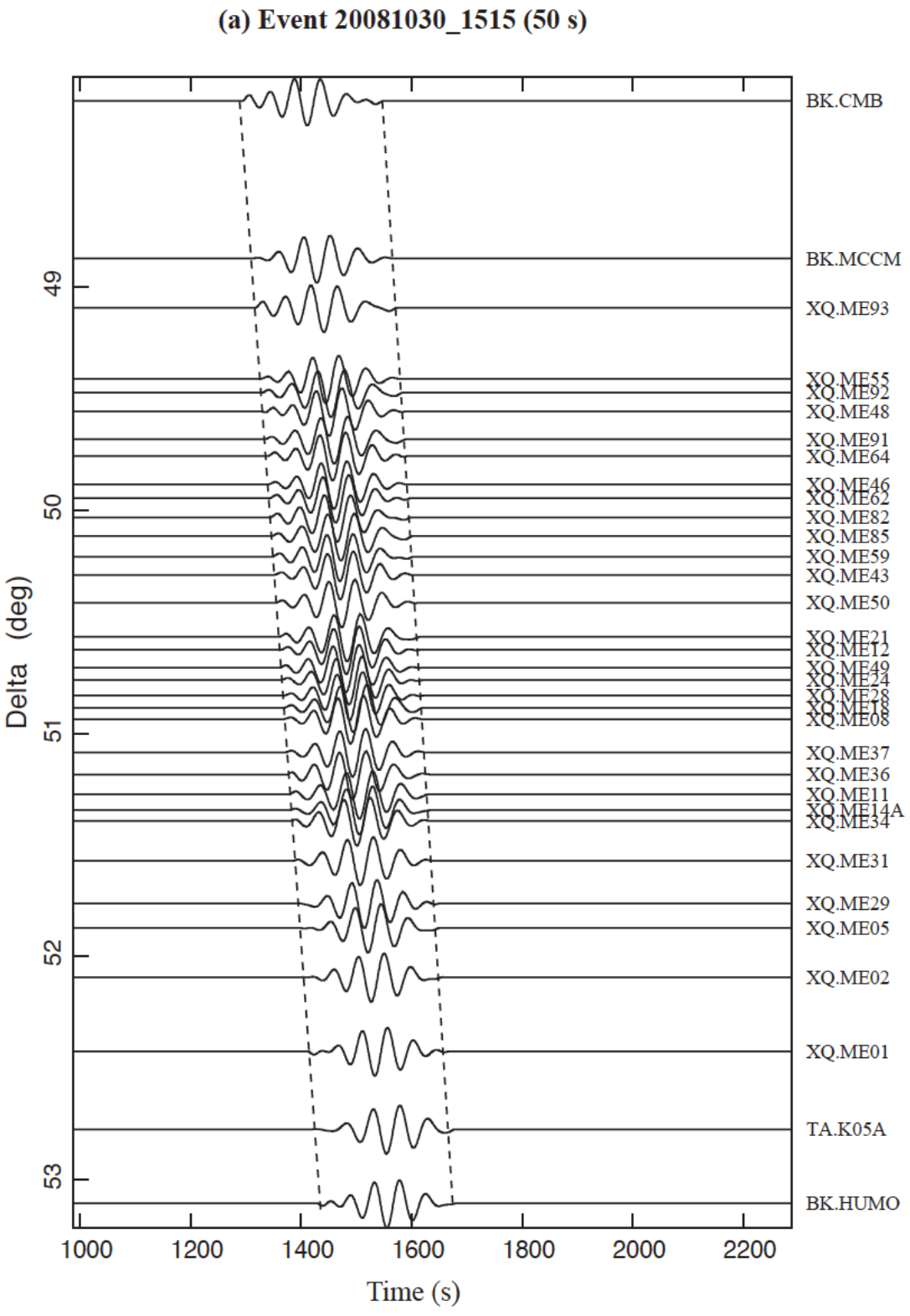

Figure 2.5 Example of filtered Rayleigh wavefield for one single event (Mw=6.0, longitude 108.25°W, latitude 9°S, epicentral distance 50.5°). (a) Filtered wavefields after time windowing (two dashed lines as the start and end time) plotted in the order of epicentral distance.

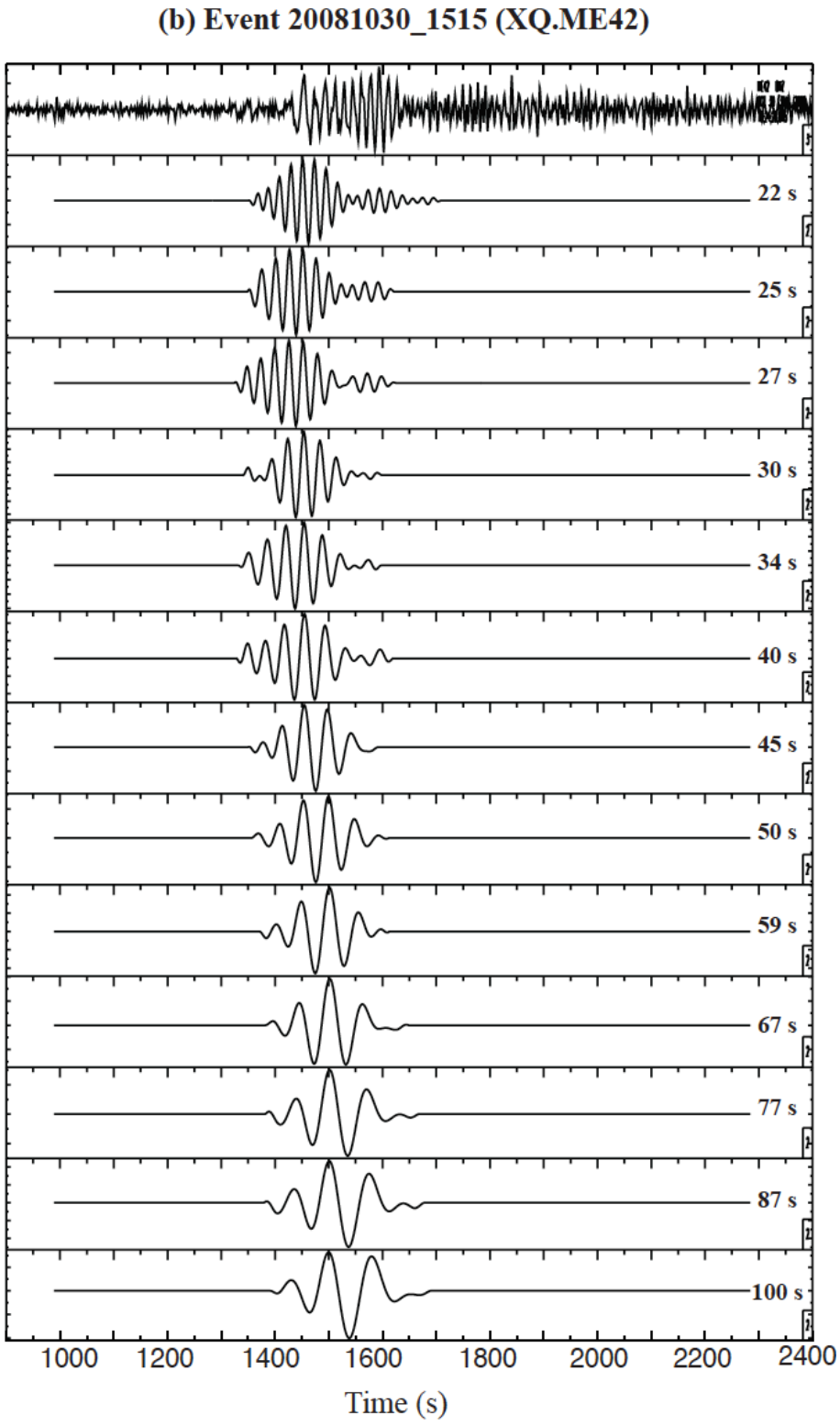

Figure 2.5 (cont.). (b) Thirteen wavefields for one single station (XQ.ME42: longitude 123.3°W latitude = 39.7°N) after bandpass filtering and time windowing from 22 to 100 s. The top trace is the raw data.

After correcting instrument responses to reference stations, we manually selected time windows with various lengths to isolate the fundamental modes from high modes or other phases. Figure 2.5 shows an example of windowed traces filtered by narrow-bandwidth Butterworth filters for each frequency band. For quality control, we kept traces with highly coherent seismograms by the order of epicentral distance (e.g., Figure 2.5a) and eliminated those with low signal-to-noise ratios (SNRs) or overcomplicated wavefields.

2.4.2 Finite-frequency two-plane wave tomography

We use a two-plane wave technique (TPWT) to invert the phase velocities [*Forsyth and Li*, 2005; *Yang and Forsyth*, 2006b]. It assumes that the incoming wavefields result from relatively simple interference of two independent plane waves, allowing certain deviations from the great circle path. This Rayleigh wave tomography better resolves the lateral heterogeneity for a regional-scale investigation than the traditional techniques assuming a single propagating wave. Meanwhile, it improves the inversion stability since it requires much fewer model parameters than the Hermite-Gaussian expansion method to characterize the wavefields [*Friederich and Wielandt*, 1995].

To account for multipathing and localized scattering effects, we incorporate the 2-D sensitivity kernels [*Yang and Forsyth*, 2006b] to resolve the wavelength-scale structures. The kernels account for off-azimuth structures due to finite-frequency effects of surface wave propagation. The phase and amplitude kernels $K_A^c(r,\omega)$ and $K_\phi^c(r,\omega)$ are defined as

$$\begin{pmatrix} \delta\varphi \\ \delta A / A \end{pmatrix} = \iint \begin{pmatrix} K_\varphi^c(r,\omega) \\ K_A^c(r,\omega) \end{pmatrix} \frac{\delta c}{c} dx^2 \tag{2.2}$$

in which δc, $\delta\phi$, δA means the perturbations of phase velocity, phase delay and amplitude, respectively. The kernel calculation is based on the Born approximation [*Yang and Forsyth*, 2006b; *Zhou et al.*, 2004]. The effective width of kernels increases as the period becomes longer (Figure 2.6). We notice that the largest wavelength of ~400 km (period of 100 s) is comparable to the dimension of the study area, reaching upper limit of lateral resolution.

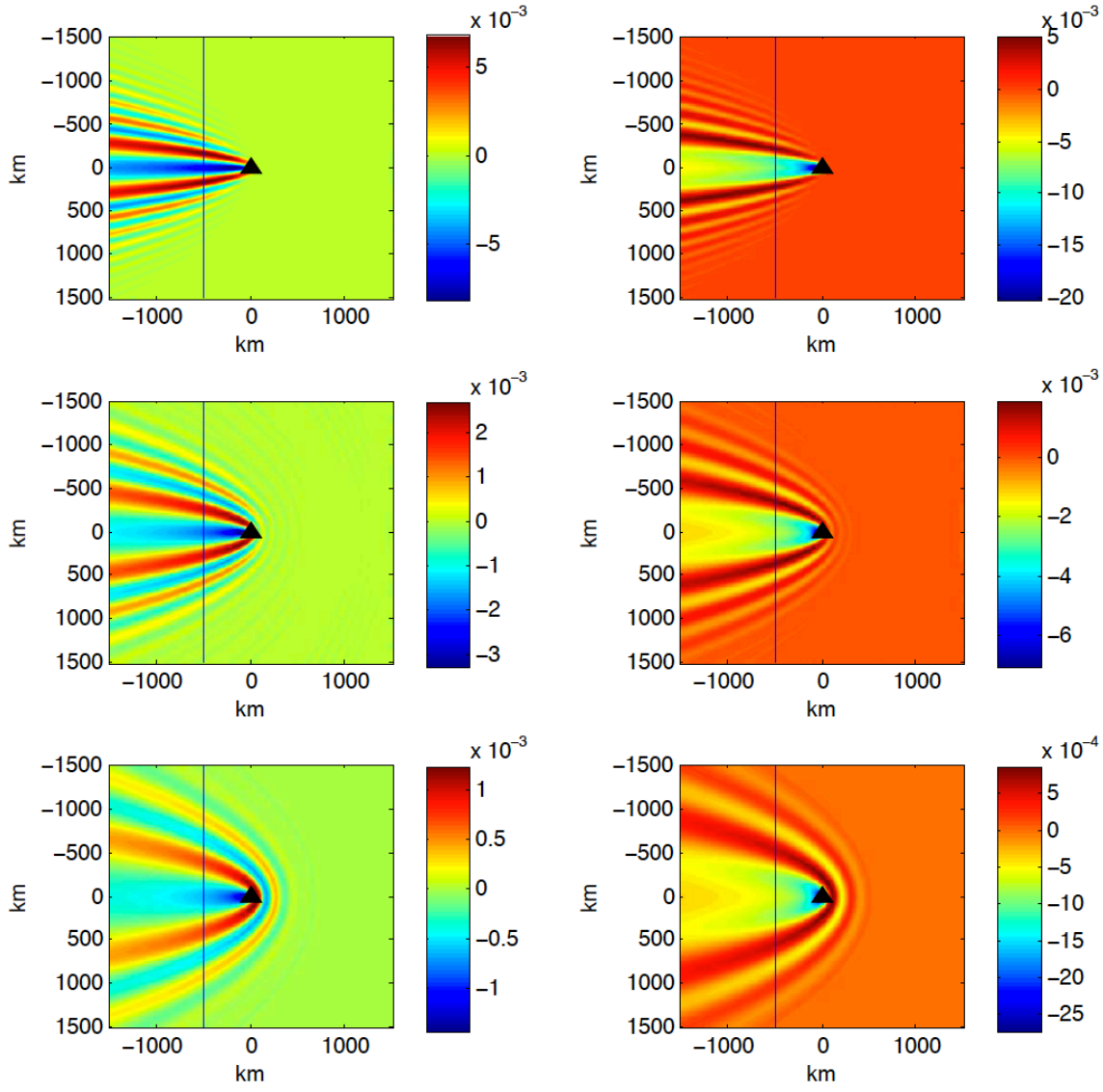

Figure 2.6 Amplitude (left) and phase (right) sensitivity kernels for an assuming plane wave incident at the receiver side.

2.4.3 Parameterization and inversion

The phase velocity maps (22-100 s) were inverted over 585 nodes on an evenly spaced 0.25° grid with doubled spaced boundary nodes to absorb the traveltime residues (Figure 2.7). We use a Gaussian averaging function (smoothing length of 50 km) to both calculate the traveltime delay and smooth the sensitivity kernels. The FAME array dimension is very small compared to the source-receiver distance. Thus, the wavefront distortion and source radiation pattern do not greatly affect the simple two-plane wave approximation.

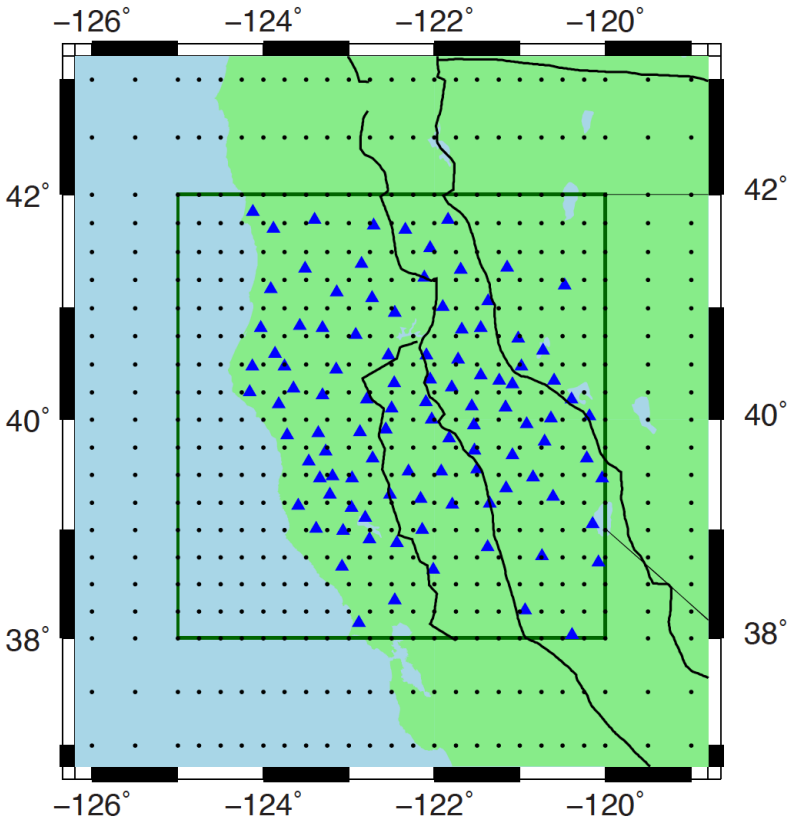

Figure 2.7 Gridnode distribution for the inversion of phase velocity coefficients and wave parameters. The blue triangles are the seismic stations. Spacing of the gridnode doubled outside the receiver-covered region (green box).

We inverted the phase velocity perturbations and wave parameters (amplitudes, initial phases and deviation angles) using both simulated annealing and a generalized iterative inversion

scheme [*Forsyth and Li*, 2005; *Tarantola and Valette*, 1982]. Starting from the phase velocities estimated from the 1-D TNA model, we applied a two-stage iterative inversion with smoothing and minimum length regularization to obtain both the average (1-D) and nodal (2-D) phase velocity coefficients. Typically, less than 10 iterations are needed for the 2-D inversion.

2.4.4 Validity of two-plane wave approximation

The good fit between the predicted and observed amplitude and phase data suggests that the two-plane wave interference is a good approximation for recorded wavefields in the period range (22-100 s). The amplitude ratios (most < 0.4, Figure 2.8a, c) and deviation angles from the great circle path (most < 5°, Figure 2.8b, d) suggest that the dominant energy travels along near the azimuthal direction, while the secondary waves complement to resolve the multipathing or scattering effects. Both amplitude and phase data are well predicted, as shown in Figure 2.8e, f. We also note that the inversion has no obvious azimuthal preference (Figure 2.8a, b). The inversion shows that the period band of 45 s has the one of the smallest RMS phase misfit (0.90 s) to recover the wave and velocity parameters among the thirteen bands. This band has the maximum number of observations and ranks for the velocity parameters (Table 1).

2.4.5 Phase velocity maps (22-100 s)

The average phase velocities (Figure 2.9) generally increase with period from 3.50 km/s at 22 s to 3.99 km/s at 100 s. The Rayleigh waves are mainly sensitive to Vs, compared to Vp and density. From the sensitivity profiles (inset of Figure 2.9), the short-period (<40 s) dispersion data are mainly sensitive to the crust, while the longer periods (>40 s) mostly sense the upper

mantle structure. The sensitivity peaks become broader and weaker as the period increases. Our 1-D dispersion curve obtained from the TPWT shows good agreement with the ANT results in the overlapping range of 22-40 s, as discussed below.

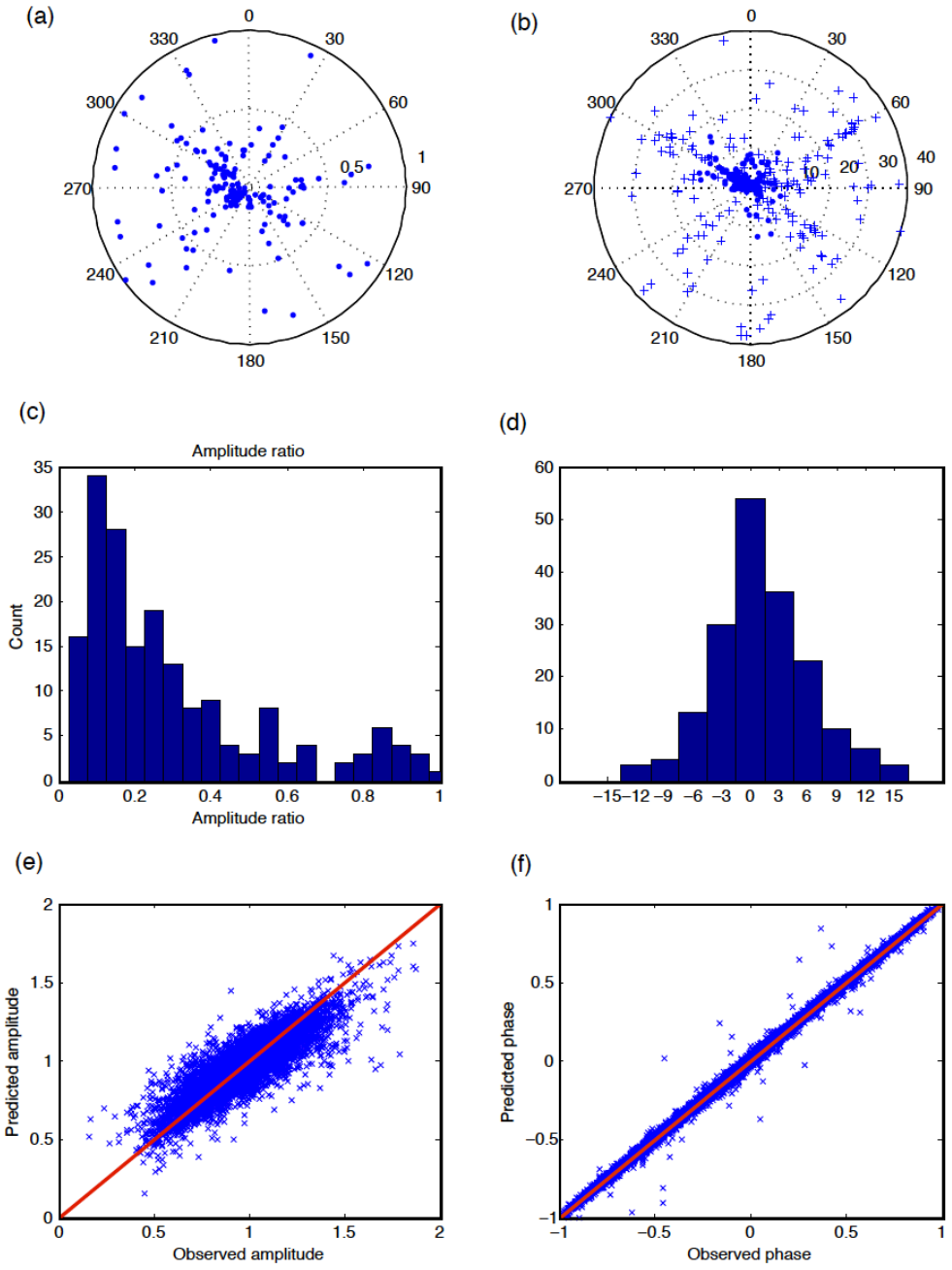

Figure 2.8 Validity of two-plane wave approximation. (a) and (b) are the distribution of amplitude ratios (primary/secondary wave) and deviation angles from the great circle path, respectively. (c) and (d) are the corresponding histograms. (e) and (f) shows the fits between the observed and predicted amplitudes and normalized phases, respectively.

Table 2.1 Phase velocity inversion parameters and results

Period (s)	Number of Observations	Total Rank	Velocity Rank	RMS Phase Misfit (s)	RMS Amplitude Misfit
22	18378	1230.7	412.3	1.05	0.198
25	19926	1281.4	417.8	1.11	0.186
27	19000	1249.5	427.3	1.04	0.161
30	19106	1232.2	424.8	0.94	0.135
34	22086	1362.7	414.7	0.96	0.122
40	24574	1465.2	426.1	0.82	0.102
45	25868	1567.8	455.6	0.90	0.094
50	24600	1468.7	414.2	0.99	0.092
59	23976	1401.4	389.3	1.08	0.090
67	23604	1376.5	401.3	0.96	0.075
77	22416	1267.2	363.6	1.00	0.077
87	20288	1160.2	347.0	1.06	0.070
100	22216	1200.3	324.1	1.27	0.076

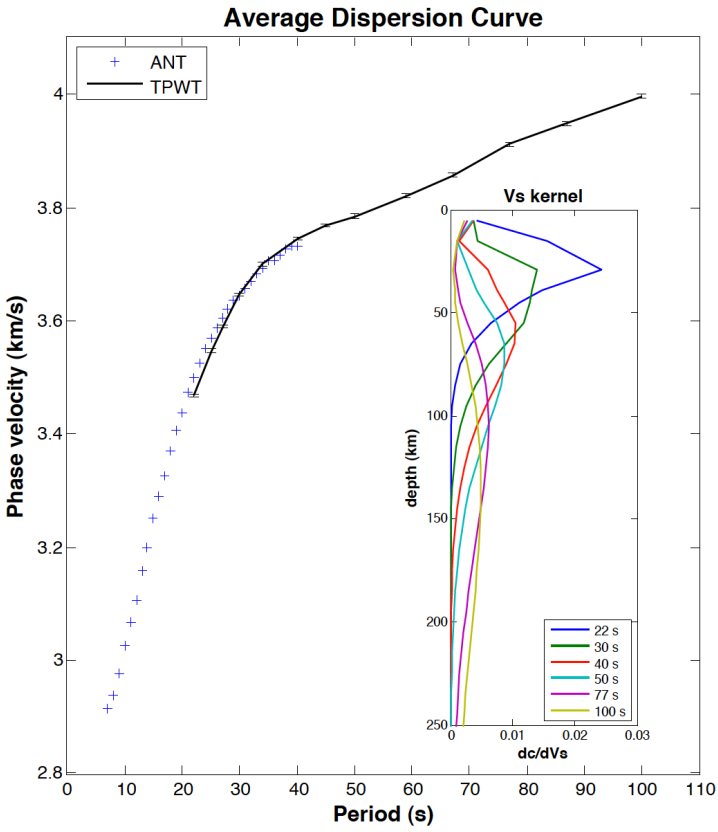

Figure 2.9 The average dispersion curve for the MTJ region. Dark points with error bars are the average ballistic phase velocities, while the '+'s are the ANT measurements. Inset is the sensitivity profiles of phase velocity with respect to the Vs structure at 22, 30, 40, 50, 77, and 100 s.

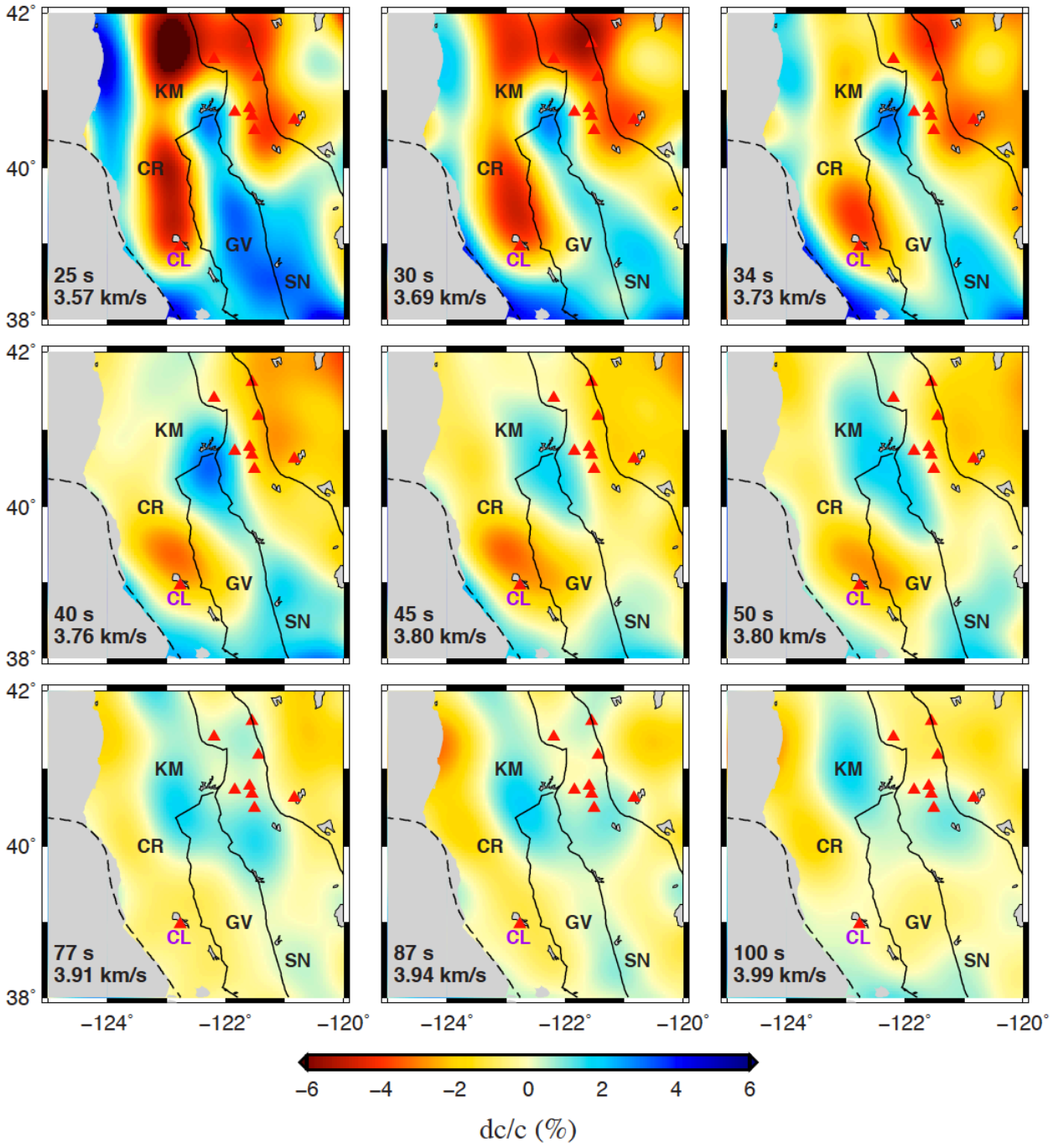

Figure 2.10 Phase velocity perturbations with respect to the average dispersion curve for the MTJ region at 25, 30, 34, 40, 45, 50, 77, 87, and 100 s. Red triangles are the Cenozoic volcanoes at southern Cascades and northern Coast Ranges.

Examining phase velocity perturbations from the regional averages, we consistently observe that at short periods (e.g., 25, 30, 34 s in Figure 2.10) there are continuous low-phase velocity anomalies under the Klamath Mountains, Cascadia volcanoes, Clear Lake and its north in the Coast Ranges. A high phase velocity anomaly that covers the Sierra Nevada mountains and a large part of the Great Valley penetrates the continuous low phase velocity anomalies, terminating at the northernmost boundary of the Great Valley. At mid-periods (e.g., 40, 45 and 50 s in Figure 2.10), the Clear Lake low phase-velocity anomaly extends eastwards across the Coast Range thrust at the range-valley boundary. Phase velocities in the Cascadia arc volcanoes are relatively low. North of Clear Lake is a high phase velocity anomaly that occupies the northernmost valley and extends further northward. In the higher band of 77-100 s (Figure 2.10), the high-phase-velocity anomaly extends farther east beneath the arc volcanoes, while, to the west, the low-phase-velocity anomaly becomes a little stronger. The phase velocity contrast decreases as the period increases due to the vertical averaging effect of surface waves, while maintaining consistent anomalous patterns. The standard deviation map at 22 s (Figure 2.11c) indicates the center of the study region is best resolved while the outer border with sparse or no station coverage remains poorly resolved.

2.4.6 Comparison with ambient noise data

The TPWT phase velocities agree well with the ANT results [*Porritt et al.*, 2011] at the overlapping period range (22-40 s). These two methods use different signals, the former using the ballistic surface wavetrains from teleseismic sources, while the latter using estimated Green's functions from the regional noise cross-correlations between stations. For example at 22 s (Figure 2.11), phase velocity maps from both methods shows consistent features of two striking low-phase-velocity anomalies under the Klamath block and northern

Coast Ranges, to the west of the high-velocity anomaly in the eastern Great Valley. The agreement between them is observed not only for average phase velocities (Figure 2.9), but also for individual dispersion curves at each station.

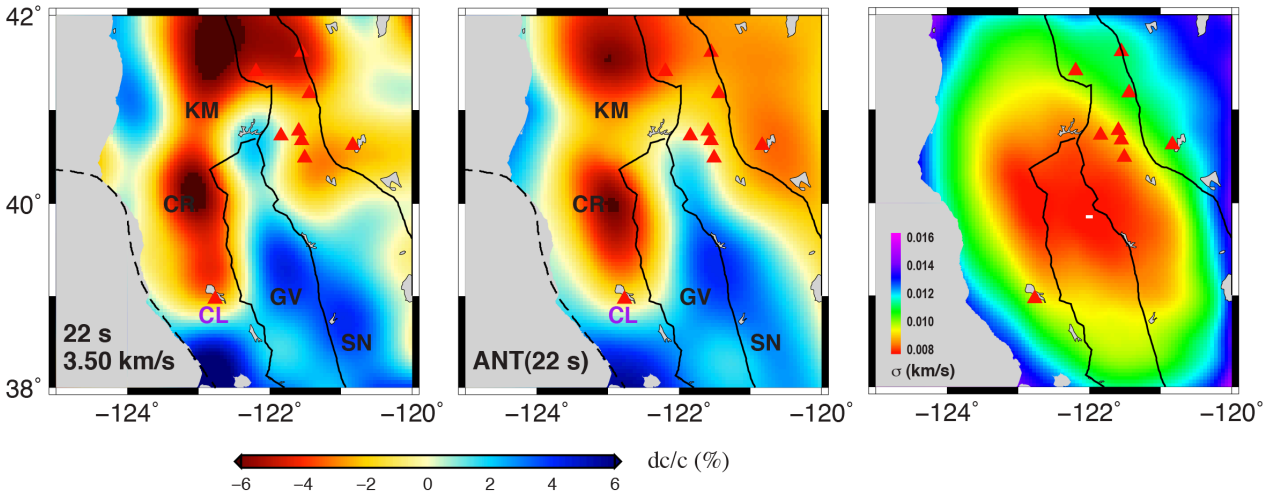

Figure 2.11 Comparison of ballistic and ANT phase velocities at 22 s. The right panel is twice of the standard deviation at 22 s using TPWT. Red triangles are the same as Figure 2.10.

The small discrepancies (Figure 2.11) between these two methods could be attributed to the different inversion stabilities. At short periods (<20 s), the ANT has better resolution than TPWT, the latter being strongly contaminated due to distortion and multipathing effects. However, at long periods (>35 s), the ANT Green's functions have weaker energy with relatively low SNRs, resulting in large uncertainties to estimate the inter-station dispersion relations. Moreover, at longer periods (>30 s), the increasing wavelength significantly reduces the number of station pairs for the ANT analysis. On the contrary, teleseismic signals used in the TPWT are relatively clean with high SNRs, especially at ~40-50 s.

2.5 Joint inversion result and discussion

2.5.1 Crustal heterogeneity: Franciscan Complex, ophiolite, and crustal melt

The crustal heterogeneity revealed by the joint inversion Vs model correlates well with surface geological features and reflects the complicated tectonic history in the accretionary wedge near the continental margin. The upper crustal low-Vs values (<3.0 km/s) in the Coast Ranges (Figure 2.12a and 2.13) are Franciscan Complex accretionary wedge, low to high-grade metamorphic rocks [*Blake et al.*, 1985]. Along the Coast Range Fault (10 and 20 km depth, Figure 2.12a), the Franciscan Complex is juxtaposed against the Klamath block, which has higher velocities (3.4-3.6 km/s), reflecting the Trinity ultramafic sheet and North Fork ophiolite [*Thurber et al.*, 2009; *Zucca et al.*, 1986]. The low-velocity layer underlying the Klamath block is most likely accretionary wedge sedimentary rocks, or possibly peridotite serpentinized under low-temperature conditions. In the Great Valley, the shallow low-Vs layer is an average of the thick sedimentary basin and the underlying crust, since we do not account directly for the basin in the starting model. The underlying high-velocity body in the valley (20 and 26 km depth, Figure 2.12a) is interpreted as the Great Valley ophiolite, probably resulting from back arc obduction of oceanic crust/mantle over the continental material during the Jurassic orogeny [*Godfrey and Klemperer*, 1998]. The ophiolite under the Great Valley can be distinguished from the lower Vs Sierran basement which is either the Foothills Metamorphic Complex and/or the intrusive batholith [*Godfrey and Klemperer*, 1998; *Godfrey et al.*, 1997]. Under the Cascadia volcanoes such as Lassen Peak and Mt. Shasta, the pronounced low-velocity layer (Vs~3.0 km/s) in the crust (e.g. Figure 2.12a) suggests crustal partial melt above the mantle wedge.

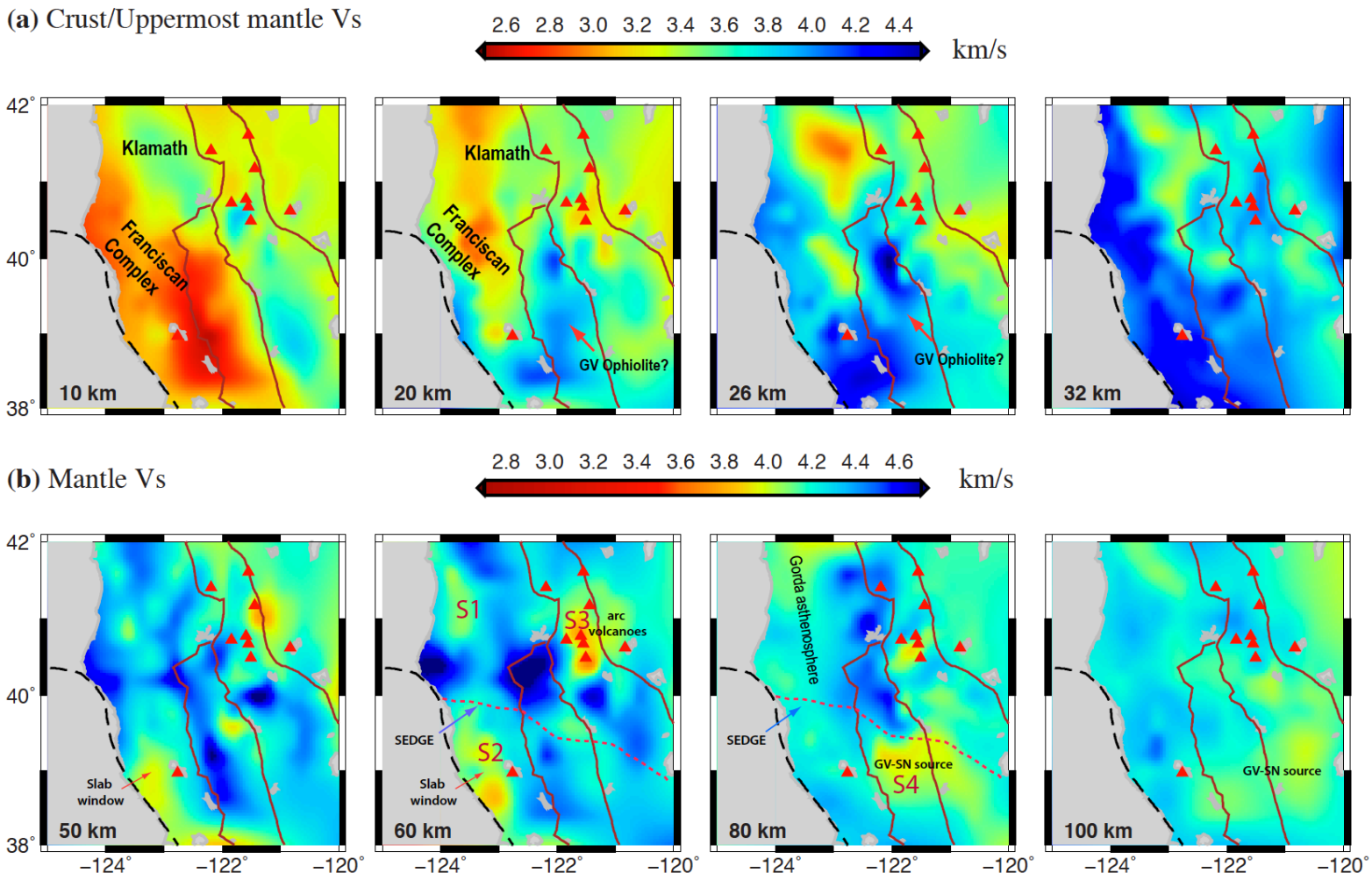

Figure 2.12 Shear velocity maps at depths from 10 to 100 km from the joint inversion of ambient noise and ballistic Rayleigh wave dispersion and Ps RFs. Red triangles are the volcanic fields. Dark dashed line is the SAF. The red dashed line is the inferred SEDGE. Note that the crust/uppermost mantle (a) and upper mantle (b) velocity maps are plotted with different color scales.

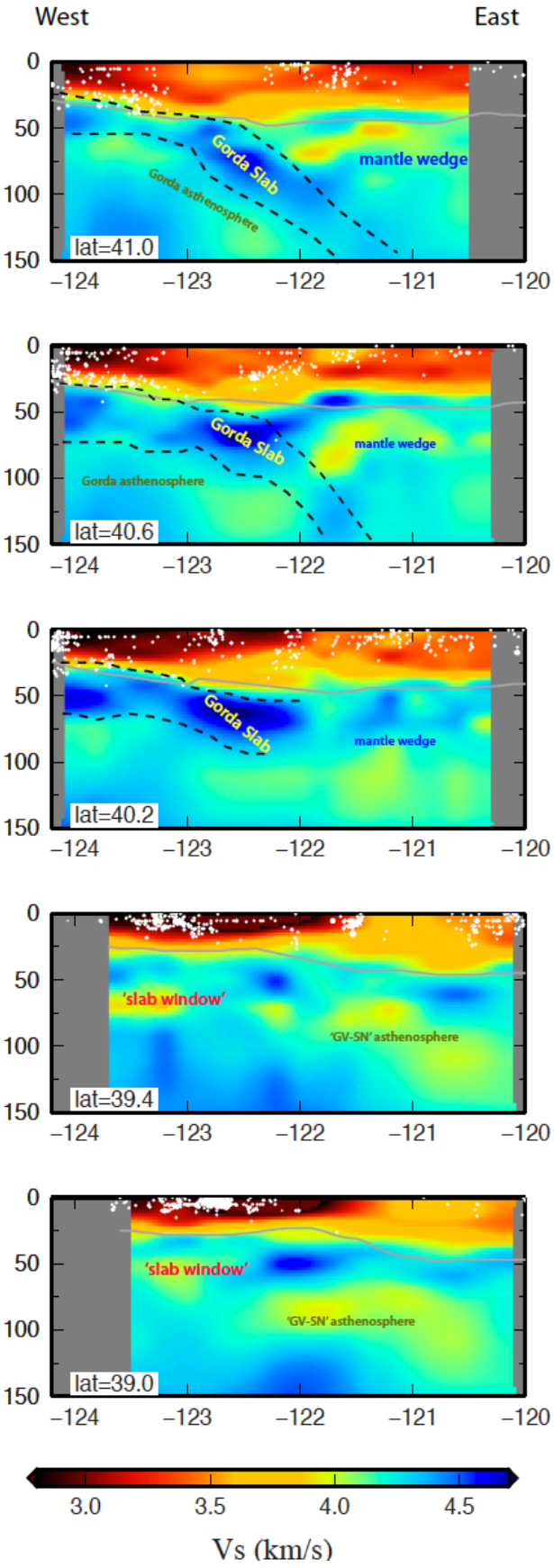

Figure 2.13 W-E cross-sections of joint inversion Vs structure from 39.0°N to 41.0°N. South of MTJ, the 'GV-SN' asthenosphere in the east connects with the slab window asthenosphere, as suggested by our 'staggered' upwelling model. White dots are the seismicity locations. Grey lines display the Moho estimates from Ps RFs alone.

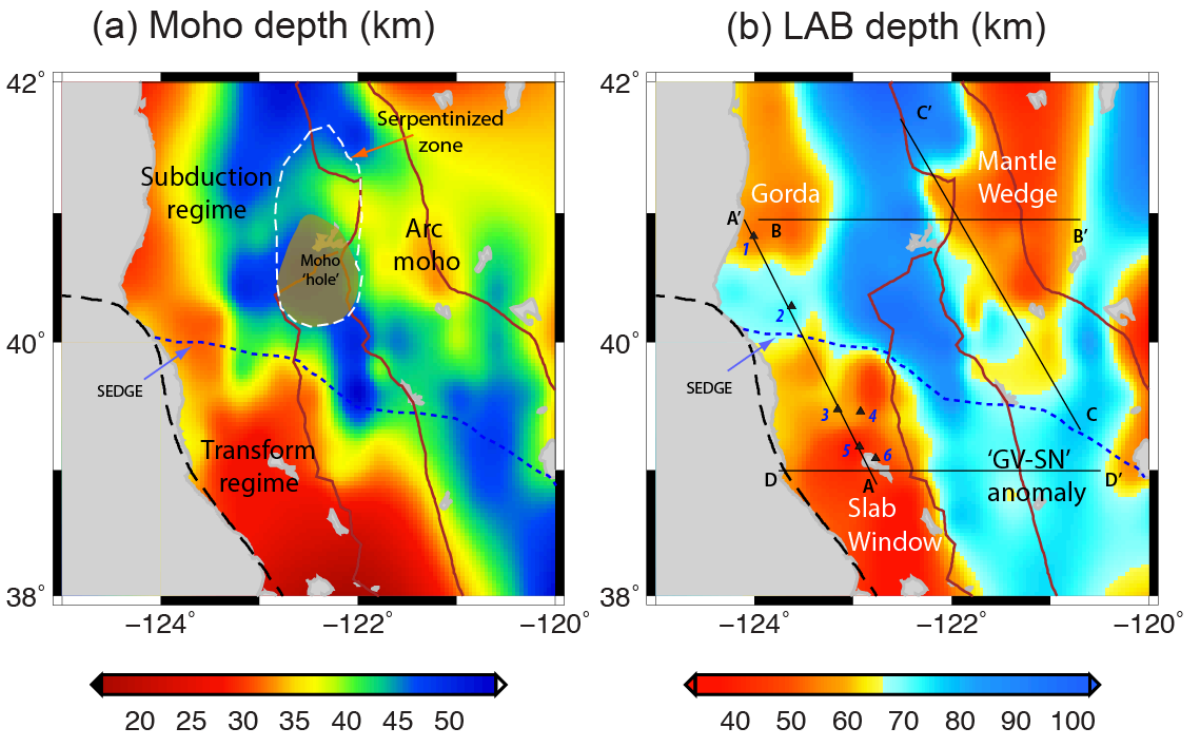

Figure 2.14 Estimated (a) Moho and (b) LAB depth maps. Blue dashed line marks the SEDGE. The relative thick forearc crust refers to the oceanic Moho. The white dashed line in (a) outlines the serpentinized zone, where we observe low-Vs uppermost mantle. Dark thin lines (AA', BB', CC' and DD') in (b) show the locations of cross-sections shown in Figure 2.15 and 2.17. The numbers 1-6 identify the locations of the Vs-z profiles in Figure 2.18.

2.5.2 Comparison with MTJSE Line 9

The MTJ marks the transition from a subduction (convergent) regime to a transform regime resulting from the northward migration of the Pacific and Gorda plates relative to North America, which profoundly influenced North American lithospheric structure [*Beaudoin et al.*, 1996, 1998; *Dickinson and Snyder*, 1979; *Furlong and Schwartz*, 2004; *Henstock et al.*, 1997; *Levander et al.*, 1998]. We compare our joint inversion Vs cross-section with the corresponding RF image [*Zhai*, 2010] and the crustal reflection/refraction P-wave velocity models [*Beaudoin et al.*, 1996, 1998], along Line 9 from the MTJ Seismic Experiment (MTJSE) (Figure 2.15a-c).

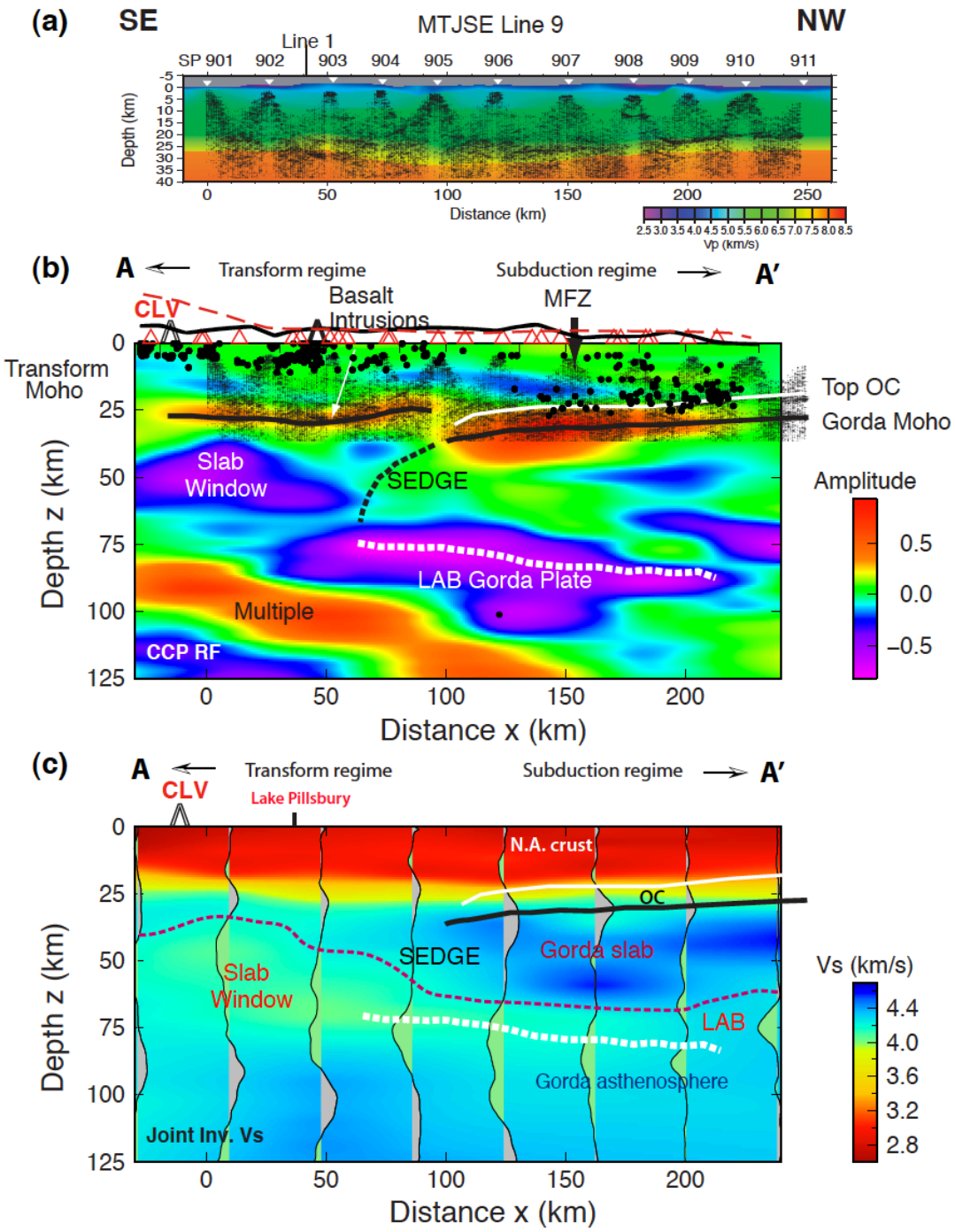

Figure 2.15 Comparison of cross-sections from the joint inversion Vs model with other seismic results along the MTJSE Line 9 (A-A' in Figure 2.14b). (a) A crustal Vp model similar to that of [*Beaudoin et al.*, 1996], (b) Ps RF image [*Zhai*, 2010], and (c) the joint inversion Vs model. Dark dots in (b) are earthquake hypocenters. In the joint inversion Vs image (c), we superimpose the top of the oceanic crust (OC) (white solid line), Gorda Moho (dark solid line), and the LAB depth under the Gorda plate (white dashed line) determined from the active source model and FAME RFs. Purple dashed line is the estimated LAB from the joint inversion Vs model taken as the center of the negative Vs gradient.

2.5.3 Gorda plate

At the northern end of the profile, the high-Vs body (3.6-4.5 km/s; Figure 2.13 and 2.15c) is the subducting Gorda plate. The SEDGE is reasonably well defined as the limit of high velocities to the south, marking the youngest part of the slab-free region in the transform regime near x=90 km (Figure 2.15). The high Vs region indicative of the plate is bounded above by a positive RF event, and below by a negative event. The former, a broad pulse, we interpret as interfering signals from the oceanic Moho and top of the oceanic crust (~20-25 km). The top of the oceanic crust in the Vs image is consistent with strong reflections from the active source study (Figure 2.15a). The Gorda oceanic crust appears as intermediate velocities (~3.9-4.1 km/s) between the reflections from the top of the crust and the Moho (dark and white lines in Figure 2.15b, respectively). The negative RF signal at the bottom of the high velocity plate (~4.4-4.5 km/s) we interpret as the Gorda LAB at ~70 km. The heterogeneous velocity structure within the Gorda lithosphere coincides with the location of the strong internal deformation as indicated by seismicity and seafloor fault offsets [*Gulick et al.*, 2001]. The Gorda plate dips southward toward the MTJ, terminating under the thickest accretionary wedge, also at x=~90 km (Figure 2.15c). It has been hypothesized that mechanical coupling between the slab and the overlying crust cause an ephemeral crustal root to form near the SEDGE (Figure 2.13, 2.15c and 2.18) [*Beaudoin et al.*, 1998; *Furlong et al.*, 2003].

North of the MTJ, we clearly image the subducting Gorda plate (high-Vs body in Figure 2.12b, 2.13, 2.15c and 2.17a) beneath North America. The forearc crust thickens eastward from ~25 to ~40 km, with thickening terminating at the location of rapid plate steepening

from ~10° to ~25° dip (Figure 2.17a). The estimated plate thickness (~30-40 km) from the RF and joint inversion Vs model agrees well with the thickness predicted from the half-space cooling model for oceanic lithosphere (~29-36 km), using ~8-13 Ma as the age of subducted Gorda plate, and 1100°C as the temperature at the base of the thermal boundary layer and 1300°C as the (convecting) ambient mantle, respectively. West of the change in slab dip, we observe a shallow LAB (~50-60 km) at the base of the Gorda plate. Low-Vs (<4.2 km/s) in the Gorda asthenosphere is likely due to proximity to the Gorda ridge, and/or shear melt [*Kawakatsu et al.*, 2009] at the base of the subducted slab.

2.5.4 Slab-free window

In the transform regime, we interpret the shallow low-velocity body between x= 0-80 km at 35-75 km depth as asthenosphere in the slab-free region (Figure 2.12b and 2.15c). North of about x=50 km, the sub-Moho shear velocity in the 'slab-free window' is <4.2-4.3 km/s but velocity decreases (<4.0 km/s) moving southward between x=0-50 km. The lowest velocities are at ~35 km depth beneath Clear Lake (Figure 2.15c and 2.18). The continuity of the low velocity anomaly from beneath Gorda to the transform regime would allow mantle flow of sub-Gorda asthenosphere into the slab window. The significant decrease in velocity accompanying this also suggests generation of a small fraction of partial melt.

In addition to the Clear Lake volcanic field, beneath the Lake Pillsbury region, the MTJSE active seismic data have imaged highly reflective bodies in the lower crust, interpreted as partially molten basalt sills [*Levander et al.*, 1998]. The area has been the site of midcrustal seismicity interpreted as diking events [*Furlong and Schwartz*, 2004]. The LAB in the slab-gap region (at z~30-40 km) is 30-45 km shallower than that beneath the Gorda plate (z~60-

75 km), resulting in decompression melting of ascending asthenosphere from beneath Gorda. Pressure-released basaltic melt can be generated at the base of the transform crust [*Henstock and Levander*, 2000], causing the slab window magmatism at Lake Pillsbury and Clear Lake. However, the apparent thickening asthenosphere and thinning of the lithosphere southward away from the MTJ are of the exact opposite the geometry predicted by the simple slab window model as described by *Dickinson and Snyder* [1979]. We suggest that the asthenosphere thickens to the south by upward and lateral flow of hydrated mantle wedge, left behind as the triple junction migrates, as we describe further below.

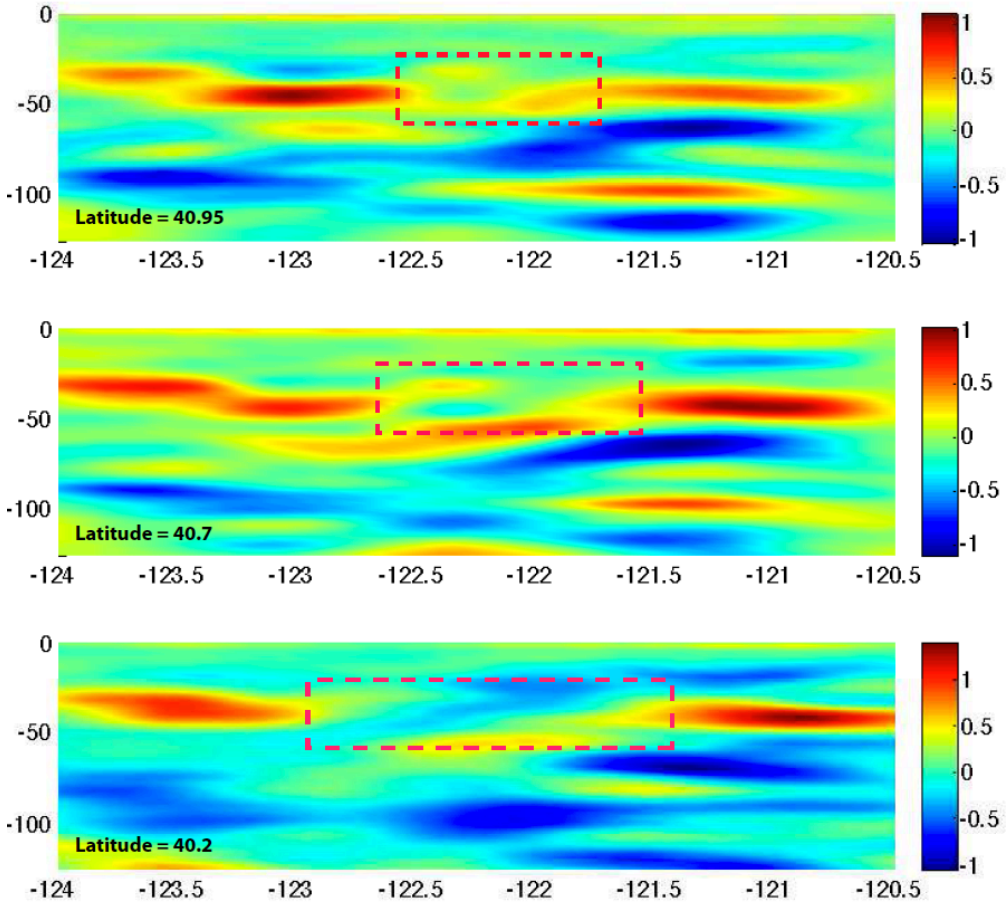

Figure 2.16 W-E cross-sections of RF images along 40.2°N, 40.7°N, and 40.95°N. The dashed red rectangles show the 'Moho hole' location with weak or missing Moho signals.

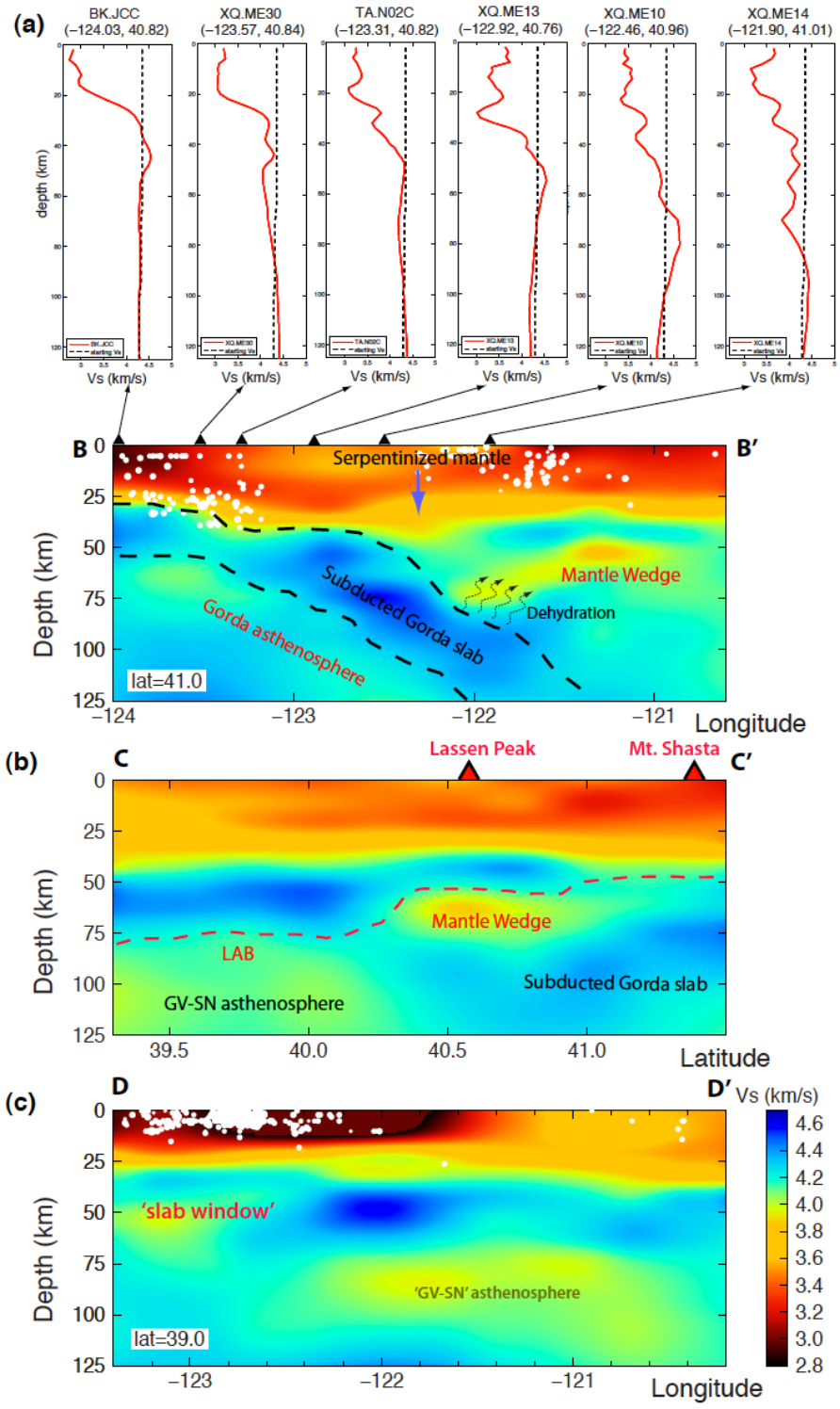

Figure 2.17 Vs cross-section along lines B-B', C-C', and D-D' in Figure 2.14b. (a) Shows the subducted slab, serpentinized forearc mantle, and low Vs mantle wedge. (b) Under the Cascadia volcanoes, the low Vs mantle wedge lies above the subducted Gorda plate. The 'GV-SN' asthenosphere is relatively deep (>75 km) in comparison to the mantle wedge asthenosphere. (c) shows the asthenospheric flow from the 'GV-SN' anomaly to the slab window from east to west. White dots in (a) and (c) are the seismicity distribution.

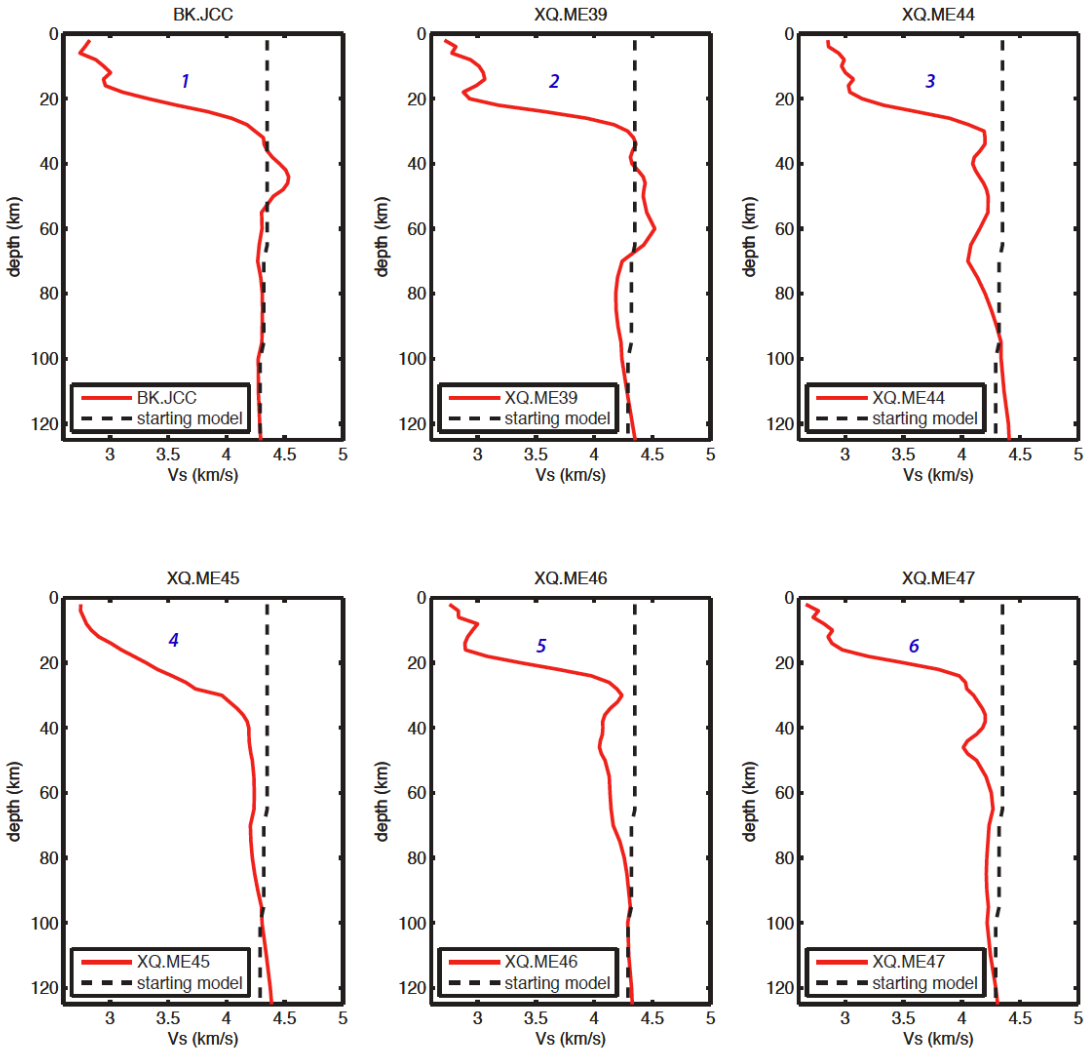

Figure 2.18 Vs profiles beneath several stations along the MTJSE Line 9 cross-section in Figure 2.15. The numbers from 1 to 6 correspond to those labeled in Figure 2.14b.

2.5.5 Forearc serpentinization

Near the northernmost Great Valley, we detect weak or absent Ps Moho signals, and a complicated Vs structure at the base of the crust, which we term a 'Moho hole' (Figure 2.14a and 2.16) [*Zhai*, 2010]. Serpentinization of the forearc upper mantle has been widely inferred to extend north along the Cascadia margin, where it is characterized by low uppermost mantle Vs, weak or reversed Ps conversions [*Bostock et al.*, 2002], weak or

missing P_mP/P_n signals [*Beaudoin et al.*, 1996, 1998; *Brocher et al.*, 2003], and characteristic magnetic anomalies [*Blakely et al.*, 2005]. Using the Vs-serpentinization relation [*Bostock et al.*, 2002], the uppermost mantle Vs (~3.7 km/s at ~40 km depth, Figure 2.17a) gives an estimate of up to ~30-40% serpentinization of the California forearc, an intermediate value between that suggested for Cascadia [*Bostock et al.*, 2002] to the north and a more normal, apparently unserpentinized northern Great Valley ophiolite [*Godfrey and Klemperer*, 1998] to the south. The transition of serpentinized-to-unserpentinized mantle near the SEDGE suggests further mantle dehydration in the post-subduction regime following slab removal [*Fulton and Saffer*, 2009], and recycling of the oceanic slab-derived components into the continental mantle. At ~50-75 km, low velocities immediately east and above the subducting Gorda plate (Figure 2.17a) suggest the possibility of ongoing dehydration of the plate [e.g., *Hacker et al*., 2003].

2.5.6 Young asthenospheres

To the south, the absence of the high-Vs slab defines the SEDGE, similar to body-wave tomography results [*Obrebski et al.*, 2010]. Besides the Gorda asthenosphere (S1 in Figure 2.12b), we observe three additional low-Vs regions (S2, S3, and S4 in Figure 2.12b) in the upper mantle, and identify 3 modern shallow LABs (Figure 2.14b), corresponding to the Cascadia mantle wedge (S3), the San Andreas transform margin (S2), and another low-Vs region (S4), the 'GV-SN' anomaly that we describe below. The SAF LAB shallows rapidly from the subduction regime to <50 km depth beneath Clear Lake. To the east of Clear Lake at greater depths (>75 km) we find low velocities (<4.1 km/s) under the Great Valley and the western Sierra Nevada block, which we term the 'GV-SN' anomaly. We interpret this feature as the cooling former mantle wedge. The LAB at the top of the wedge is deeper (~75 km)

than elsewhere, likely due to development of a conductively cooling boundary layer and/or a remnant lithospheric lid under North America.

2.5.6.1 Mantle wedge and Cascadia volcanoes

We interpret the shallow mantle wedge LAB under the Cascadia arc as resulting from hydration-induced decompression melting, causing a significant drop in Vs [*Leeman et al.*, 2005]. The extremely low velocities (~3.6 km/s at 60-80 km depth) in the wedge (Figure 2.12b and 2.17a, b) can be attributed to partial melts from dewatering of the subducting oceanic lithosphere and convective upwelling [*Leeman et al.*, 2005]. Cross-sections at 41.0N (Figure 2.17) and 40.6N (Figure 2.13) show continuous low velocities from the top of the Gorda plate at 50-75 km depth to directly beneath the Cascadia arc, suggesting that these are fluid pathways from the dehydrating slab. Fluid-mediated decompression melting significantly shallows the LAB depths to 50-60 km, slightly subcrustal, and drives Cascadia magmatism by allowing melt to infiltrate the base of the North American lithosphere. The mantle wedge magmatism causes the arc volcanoes of the southernmost Cascadia Range: Lassen Peak and Mount Shasta. We interpret the low Vs upper mantle in the back arc as a continuation of the mantle wedge asthenosphere.

2.5.6.2 'GV-SN' anomaly

As the MTJ migrates northwestward, it leaves behind a mantle wedge. We suggest that the 'GV-SN' anomaly is the former mantle wedge, located to the south, along strike with the current mantle wedge. However, we note that the LAB at ~75 km is deeper than the active mantle wedge by 15-20 km. We interpret the southeastward thickening high-Vs lithospheric

lid (~10-30 km thick, Figure 2.17b) as a growing thermal boundary layer caused by cooling of former mantle wedge asthenosphere south of the SEDGE.

Slab removal changes the mantle flow field by removing the driving force of mantle wedge counter flow. If the asthenosphere under the Gorda plate can flow into the slab-free window, then Gorda asthenosphere beneath deeper parts of the subducting slab can also flow into the former mantle wedge. It seems likely that the former mantle wedge can also flow laterally and upward into the slab window. The 'GV-SN' low velocity region is likely either, former mantle wedge, or former mantle wedge mixed with Gorda asthenosphere.

2.5.6.3 SAF transform regime

Beneath the transform regime, the significant decrease in Vs (<4.0-4.2 km/s, Figure 2.12b and 2.15c) and very shallow LAB (~30-40 km) south of SEDGE are attributed to partial melts produced by decompression melting of upwelling asthenosphere from beneath Gorda [*Henstock and Levander*, 2000]. The melting mechanism here differs from that beneath the Gorda plate (shear lensing) and mantle wedge (hydration-induced reduction of the solidus). A certain amount of the melt is accreted at the base of the transform crust [*Levander et al.*, 1998], creating some of the slab window magmatism in Clear Lake and elsewhere in the Coast Ranges. The shallowest LAB under the Coast Ranges is between Clear Lake and Lake Pillsbury, the latter being predicted as a location for future volcanism [*Levander et al.*, 1998]. We interpret the continuity of low velocities (Figure 2.15c) and SKS split patterns (Figure 2.19) to indicate mantle flow into the Coast Ranges slab window from beneath the Gorda plate and from the mantle wedge.

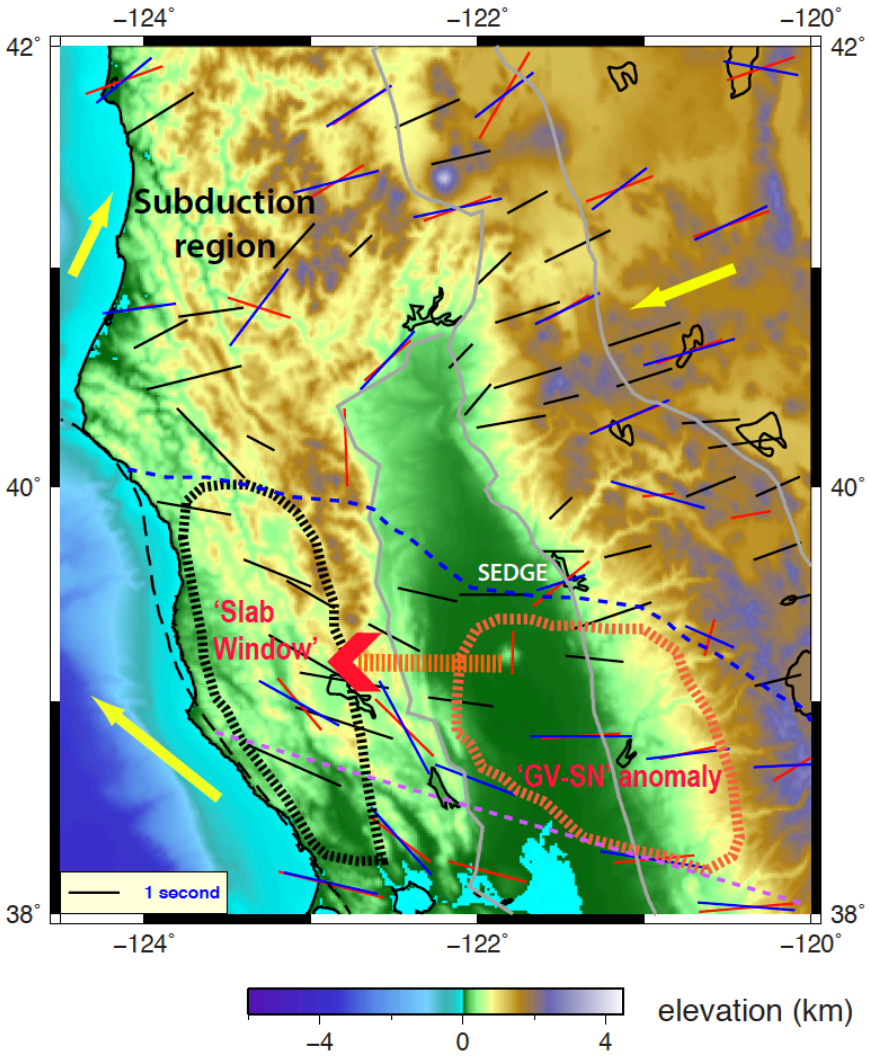

Figure 2.19 Fast polarization directions of SKS splits in the MTJ region with absolute plate motions (yellow arrows) of Gorda, Pacific and North American plates. Shear wave splitting results are plotted as different colors: black from *Eakin et al*. [2010], blue from *Fouch and West* [personal communication], and red from *Liu* [2009]. Black and orange dashed contours are the slab window region in the transform regime and the 'GV-SN' anomaly inferred from joint inversion in this study. Blue dashed line is the current SEDGE, while purple dashed line shows previous SEDGE location.

2.5.7 Mantle flow

Geochemical data from the northern Coast Range volcanics show strong similarity to the mantle wedge, both having enriched large-ion lithophile and depleted high-field-strength elements [*Furlong and Schwartz*, 2004; *Whitlock et al.*, 2001]. *Hole et al.* [1998] argued that a mantle wedge-derived origin could better fit the Coast Range heat flow data [*Lachenbruch*

and Sass, 1980], i.e., mantle flow from the wedge to the shallow slab-free region. In contrast, initially low $^{87}Sr/^{86}Sr$ ratios and high ε_{Nd} of the volcanic rocks [*Cole and Basu*, 1995] in the Coast Ranges south of Clear Lake imply that the slab window was first occupied by asthenosphere from an oceanic source. This is consistent with the continuity of the LAB topography in the slab window south of the SEDGE [*Zhai*, 2010].

It has been suggested that a circular pattern of SKS splits observed in central California, Nevada, Utah and Oregon result from large scale toroidal mantle flow emanating from beneath the Gorda plate along the SEDGE [*Eakin et al.*, 2010; *Zandt and Humphreys*, 2008]. The scale of this flow pattern is almost entirely out of our study region. For example Figure 1 of *Piromallo et al.* [2006] and Figure 2b of *Zandt and Humphreys* [2008] suggest that immediately south of the MTJ, mantle flow from under the sinking Gorda plate will be normal to the plate edge, meaning to the south-southwest in the Mendocino region, and of small magnitude. SKS splitting measurements from *Eakin et al.* [2010], *Liu* [2009] and *Fouch and West* [personal communication] show a nearly SEDGE parallel signature (Figure 2.19) with relatively large magnitudes (~1s). The inconsistency between the observed SKS splits in the MTJ region and the predictions of toroidal flow are the result of the scale of observation. We suggest that locally the plate edge causes a more complicated mantle flow field as the sinking plate drags viscous mantle down with it.

The low Vs in the 'GV-SN' anomaly, the SKS splits, and the appearance of a mantle wedge signature in the geochemical data [*Furlong and Schwartz*, 2004; *Whitlock et al.*, 2001] lead us to hypothesize a 'staggered', two-stage upwelling model (Figure 2.20 and 2.21). We

suggest that as North America moves to the northwest, the opening slab window is filled from two sources: The sub-Gorda asthenosphere flows upward and to the southeast into the slab window, while simultaneously abandoned mantle wedge flows upward and to the southwest into the slab window (Figure 2.20 and 2.21b, c). The abandoned wedge is left behind as the 'GV-SN' asthenosphere (Figure 2.17c and 2.19), and is likely still contributing to the slab window asthenosphere by upward and lateral flow. The former mantle wedge still retains a large amount of slab-derived fluids that can suppress the solidus temperature, producing decompression melting as it ascends, causing surface volcanism and the significant Vs reduction under Clear Lake (Figure 2.15c and 2.20). The 'GV-SN' asthenosphere provides the mantle wedge-type geochemical signatures [*Whitlock et al.*, 2001]. The SKS split directions are consistent with southeast flow from beneath Gorda, southwest flow from beneath Cascadia, and east to west flow from the 'GV-SN' anomaly. This wedge-to-window mantle flow is consistent with numerical simulation based on the MTJ geometry under the transform regime [*Liu and Furlong*, 1992], as well as several other studies [*Guzofski and Furlong*, 2002; *Furlong and Govers*, 1999; *Furlong and Schwartz*, 2004]. The east-west Vs cross-sections (Figure 2.13) show that the low-velocity asthenosphere is continuous from the 'GV-SN' anomaly to the low velocities of the slab window under the Coast Ranges, consistent with this asthenospheric flow model.

This model also provides an alternative explanation for the notable time lag (~3 Myr in Clear Lake) between MTJ migration and Cenozoic Coast Range volcanism [*Dickinson*, 1997]. Although part of the delay in northern Coast Range volcanism could be caused by time spent establishing a magmatic system [*Dickinson*, 1997; *Liu and Furlong*, 1992], or the

propagation time of the flow from the arc to the window [*Furlong and Schwartz*, 2004], the staggered upwelling model suggests that the delay in volcanism results from the times of vertical and lateral transport of the former wedge into the slab window, and mixing with the Gorda asthenosphere. Until there is sufficient accumulation of hydrated asthenosphere at shallow depths to dramatically suppress the mantle solidus and enable large scale decompression melting, volcanism is limited to small-volume decompression melting of Gorda asthenosphere [*Levander et al.*, 1998].

2.6 Summary

Overall, a variety of seismic probes identify four distinct, young LABs and indicate mantle flow between them in the MTJ region. Joint inversion of Rayleigh wave phase velocity dispersion data (8-100 s) and Ps RFs provides complementary constraints on the Vs structure at the lithospheric scale. The relative plate motions associated with the northwestward migration of the MTJ produces three distinct modern asthenospheres: one beneath the volcanic arc where dewatering continues, one remnant mantle wedge in which fluid flux has stopped, and the long-discussed slab window beneath the Coast Ranges. We suggest that the slab window is filled by mantle material from the Gorda asthenosphere and from the present and abandoned mantle wedge. The fourth LAB is under the subducting Gorda plate. These four young LABs are strongly related to subduction (vertical) and northwestward (horizontal) migration of the MTJ. The 'staggered' upwelling model, which mixes mantle flow from beneath the Gorda plate and with that from the mantle wedge, is consistent with the seismic observations, and identifies the source of the mantle-wedge geochemical signature seen in the Clear Lake volcanics.

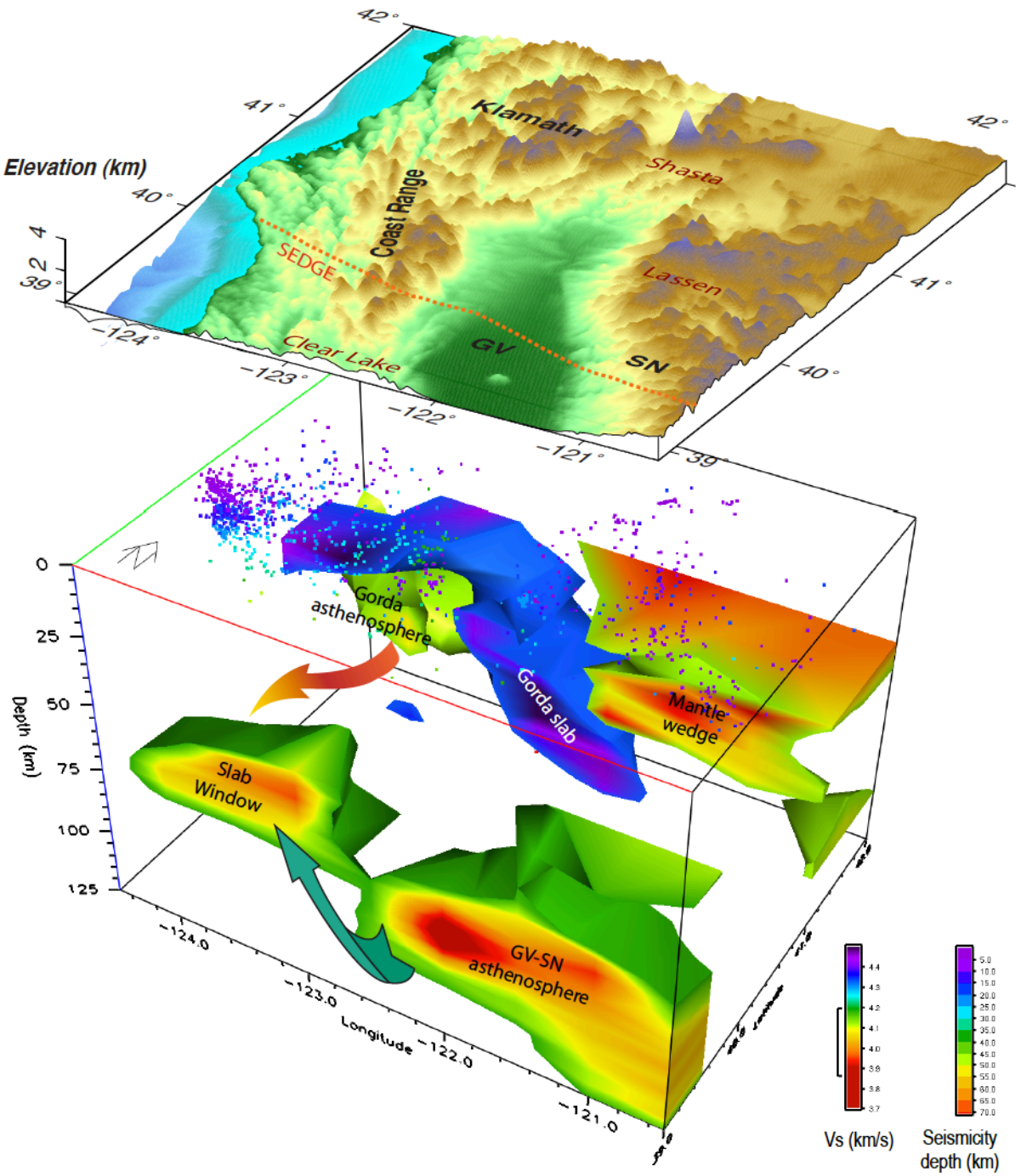

Figure 2.20 The 'staggered upwelling' model illustrated by the Vs isosurfaces (3.86, 4.20, and 4.35 km/s) at 39-40°N and 41-42°N, overlain by the topography map. We suggest a hybrid source for asthenospheric upwelling near the SEDGE (dashed orange line in the topography map), first infilled by the subslab source (red arrow) after slab removal, followed by the major flow (green arrow) from beneath the 'GV-SN' anomaly in its east. The colored dots indicate the location of the seismicity in the 41-42°N region.

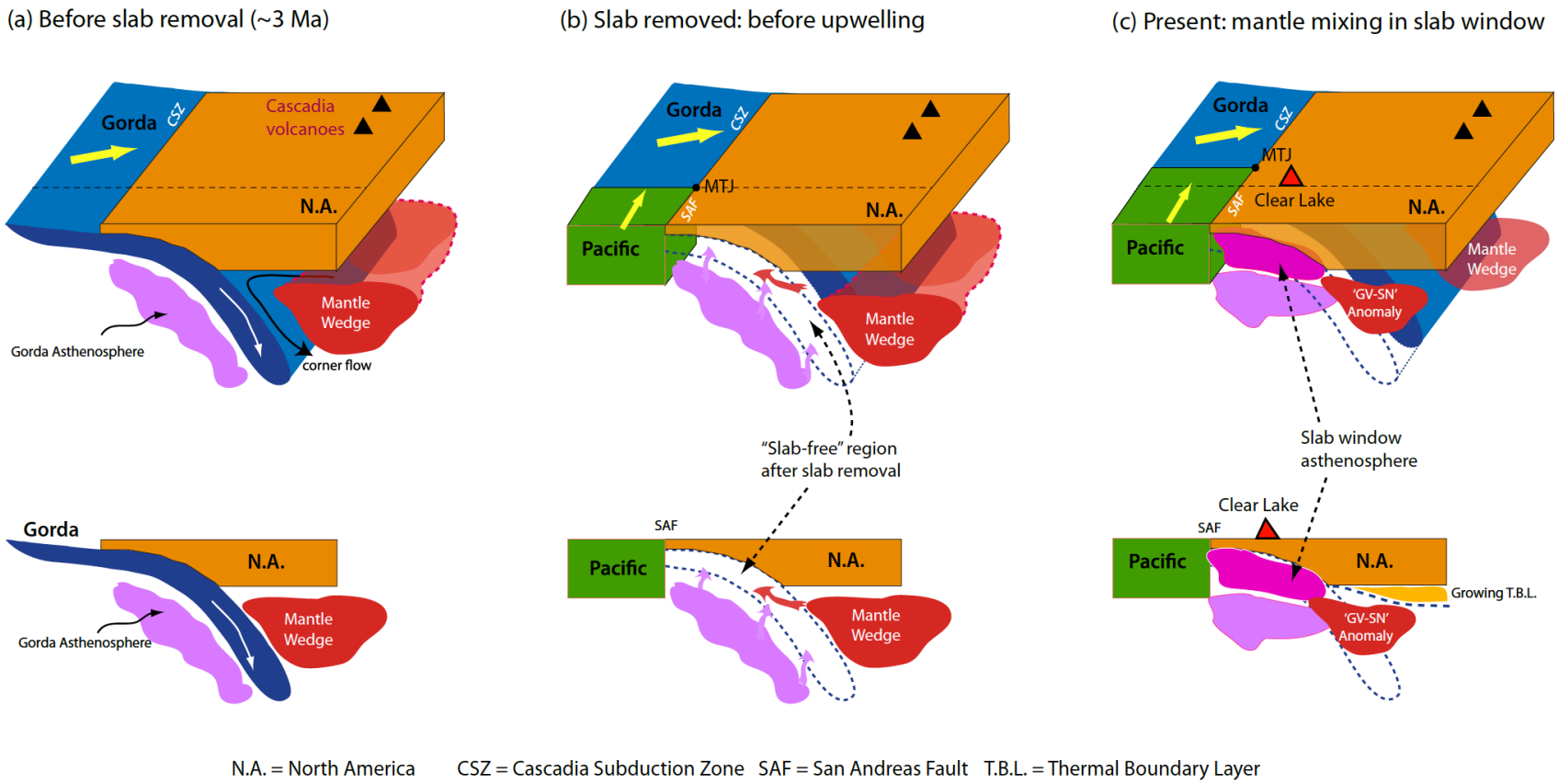

Figure 2.21 Schematic diagrams of mantle upwelling model under the transform regime. North American plate is fixed. Bottom figures are cross-section views taken along the latitude of Clear Lake, shown as the dark dashed lines in the top panel. (a) The MTJ was south of the current Clear Lake location, the Gorda plate was subducting beneath the North American lithosphere along the Cascadia subduction zone, forming the Cascadia arc volcanoes (dark triangles). The Gorda asthenosphere was separated from that of the mantle wedge by the subducting plate. (b) An imaginary moment right as the subducting slab passes the MTJ and is replaced by asthenosphere. Northward migration of the Gorda plate creates the slab-free region. The Gorda and mantle wedge asthenospheres start to upwell and mix in the slab-free window region. (c) After mantle upwelling and mixing. Decompression melting led to the most recent surface volcanism at Clear Lake in the Coast Ranges. The abandoned mantle wedge is the 'GV-SN' anomaly (red), which contributes hydrated mantle wedge asthenosphere to the melting region under Clear Lake.

Chapter 3 IMAGING CRUSTAL AND UPPER MANTLE STRUCTURE BENEATH THE COLORADO PLATEAU USING FINITE-FREQUENCY RAYLEIGH WAVE TOMOGRAPHY

A new 3-D Vs model of the crust and upper mantle beneath the Colorado Plateau (CP) and surrounding regions of the southwestern U.S. was made with finite-frequency Rayleigh wave tomography using EarthScope/USArray data. The goal of our study is to examine the CP lithospheric modification that has resulted from Cenozoic tectonism and magmatism. We have inverted for the isotropic Vs model from a grid of Rayleigh wave dispersion curves obtained by a modified two-plane wave method for periods from 20 to 167 s. We map the LAB under the CP by identifying the middle of the shallowest upper mantle negative Vs gradient. The LAB depths inferred here agree well with RF estimates made independently. The strong lateral Vs heterogeneity can be mainly attributed to 200-400 K variations in temperature together with ~1% partial melt fraction in the shallow upper mantle. The resulting Vs structures clearly image the upper mantle low-velocity zones (LVZs) under the CP margins that are associated with magmatic encroachment. These upper mantle LVZs resulted from the convective removal of the CP lithosphere that had been rehydrated by subduction-released water, refertilizing and destabilizing it. This convective erosion by the asthenosphere at the low-viscosity part of the lithosphere is driven by the large step in lithospheric thickness and the thermal gradient across the boundary between the plateau and the extended Basin and Range since the Mid-Cenozoic at a rate similar to that of magmatic migration into the plateau from the southeast, south, and northwest. Moreover, the Rayleigh wave model images parts of a high-velocity drip in the western CP, and thus provides additional seismic evidence for ongoing convective downwelling of the lithosphere that was

initially suggested by RFs and body wave tomography. Both the widespread edge convective erosion, of which the regional delamination-style downwelling processes are a 3-D manifestation, could provide additional buoyancy sources at the CP margins.

3.1 Introduction

The CP is a high standing (~1.8-2.0 km), relatively stable physiographic province in the tectonically active southwestern U.S. (Figure 3.1). This distinct province is bounded by the Uinta Mountains and the Wasatch front in the north, the highly deformed Southern Rocky Mountains (SRM) in the northeast, the Rio Grande Rift (RGR) valley in the east, and the highly extended Basin and Range Province (BRP) in the south, west and southwest. Between the Southern Basin and Range (SBR) and the plateau, there is a ~100-km-broad zone with transitional geologic and geophysical characteristics including normal faulting and recent magmatism (the CP-BR transition region). The Colorado Mineral Belt and the Jemez lineament are two distinct geologic features [*Humphreys et al*., 2003] lying at the CP-SRM and CP-RGR boundaries, respectively (Figure 3.1).

The availability of the EarthScope/USArray TA data provides an unparalleled opportunity to construct high-resolution tomographic images in the tectonically active southwestern U.S. Prior to the USArray program, seismic investigation of the CP and its adjacent regions was limited to either regional and continental scale tomography studies, with rather poorly sampled data [e.g. *Humphreys and Dueker*, 1994; *van der Lee and Nolet*, 1997], or only relatively small regions or active source seismic profiles [e.g. *McCarthy et al*., 1991; *McCarthy and Parsons*, 1994; *Wolf and Cipar*, 1993; *Parsons et al.*, 1996; *Sheehan et al*., 1995, 1997; *Zandt et al*., 1995; *Henstock et al*., 1998; *Snelson et al.*, 1998, 2005; *Levander et*

al., 2005; *Wilson et al*., 2005ab, 2010]. Since USArray, additional studies have provided new velocity models for the uppermost [*Buehler and Shearer*, 2010] and upper mantle [e.g. *Humphreys and Schmandt*, 2010] beneath the CP, as well as Moho and LAB depth [*Levander and Miller*, submitted]. Our Rayleigh wave tomography can provide better vertical resolution in the upper mantle above ~200 km with absolute Vs information, complementing the body-wave tomography, which provides relative velocity perturbations.

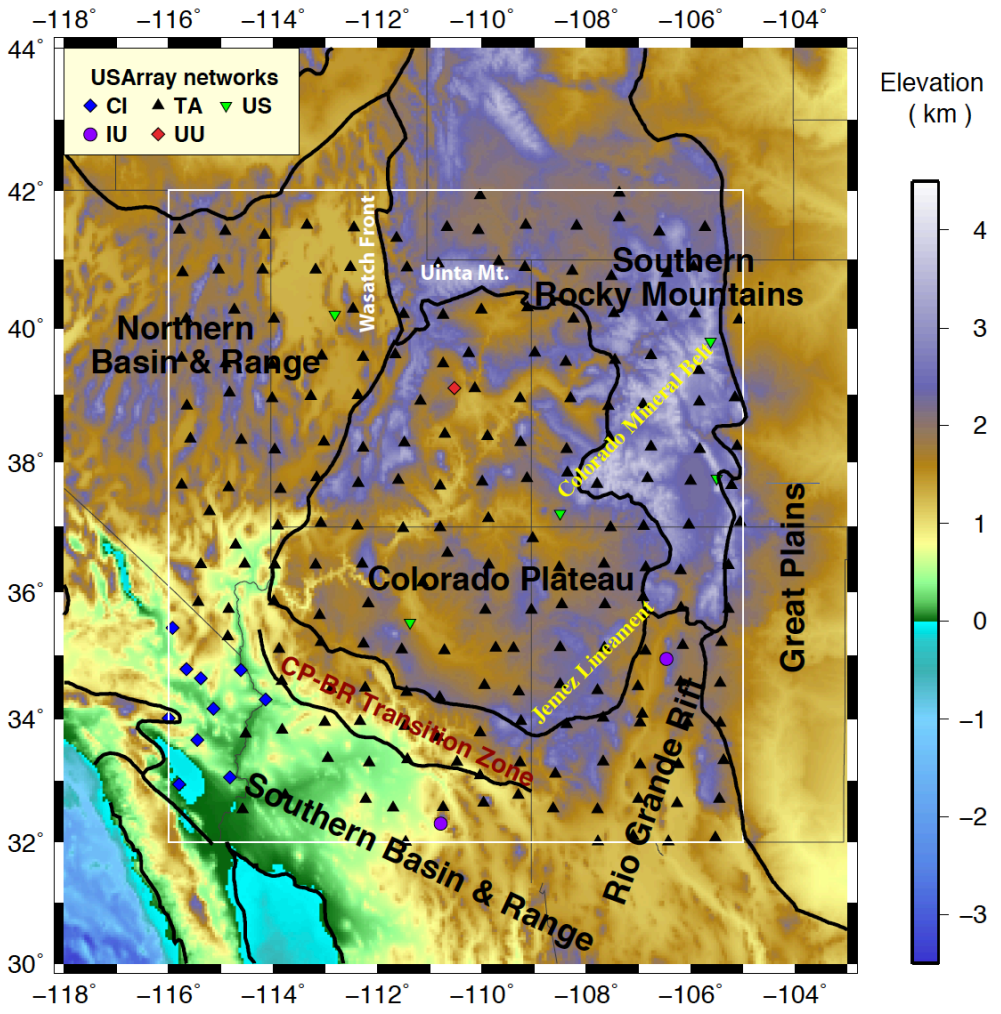

Figure 3.1 Topography map of the major physiographic provinces of the southwestern United States, including the CP, SBR, NBR, RGR, SRM and the Great Plains. Station distribution inside the study area (white box) from various USArray networks (TA=Transportable Array; CI=Caltech Regional Seismic; US=US National Seismic; IU=IRIS/USGS; UU=University of Utah Regional) are also shown with different symbols (see legend). The topography data is from the ETOPO1 model [*Amante and Eakins*, 2009].

Small-scale convection such as edge-driven convection [e.g. *van Wijk et al*., 2008, 2010] or convective destabilization of the Proterozoic lithospheric core beneath the CP [*Humphreys et al*., 2003; *Levander et al*., 2011] has been suggested to explain the unusually large velocity contrast across the transition edges. Based on 2-D seismic tomography from the La RISTRA experiment [e.g. *West et al*., 2004; *Gao et al*., 2004; *Sine et al*., 2008] and geodynamic modeling, *van Wijk et al*. [2010] suggested that edge-driven convection caused the Late-Cenozoic magmatism and uplift at the edges between the CP and BRP or RGR. Whether such convective erosion at the CP margins is a localized or widespread feature remains unclear, and our Rayleigh wave tomographic image provides a comprehensive seismic model to examine the convective erosion around the transition area into the center of the plateau. Moreover, our model provides an independent study to understand the complicated physical state under the western CP. Complex Ps conversions beneath much of the plateau have been noted in RF studies [*McCarthy and Parsons*, 1994; *Wilson et al*., 2005a; *Gilbert et al*., 2007; *Levander and Miller*, submitted]. *Gilbert and Sheehan* [2004] suggested that the weak Ps conversion might be introduced by a gradational impedance transition possibly caused by magmatic underplating [*Wolf and Cipar*, 1993]. However, *Levander et al*. [2011] proposed a delamination-style lithospheric downwelling under the western CP margin to explain the split of Moho signals observed in the RF volume using USArray data. Most of the converted amplitudes beneath the western CP separate into discrete positive events with weak amplitudes compared to those of the surrounding tectonic regions. A high-resolution Vs model can improve our understanding of the regional lithosphere-asthenosphere interaction and the complicated lithospheric convection beneath the western CP.

A detailed 3-D Vs model can also help to understand the CP uplift mechanism, which remains the subject of a long-standing debate. Numerous mechanisms have been suggested to explain the ~2-km Cenozoic rock/surface uplift of the plateau since 80 Ma. The buoyancy sources from the crust, mantle lithosphere and asthenosphere can mainly be attributed to four major factors: thermal expansion [*Thompson and Zoback*, 1979; *Roy et al*., 2009], mechanical lithospheric thinning [*Bird*, 1979; *Spencer*, 1996; *Lastowka et al*., 2001], crustal thickening [*Morgan and Swanberg*, 1985; *McQuarrie and Chase*, 2000], and/or dynamic uplift [*Moucha et al*., 2008, 2009; *Liu et al*., 2010]. No consensus on the uplift contributed by each factor has yet been achieved. Knowledge of the present-day LAB depths determined seismically from our surface wave model can shed some light on the various uplift scenarios, given an assumed initial configuration. To better image the edge convective processes in the upper mantle and examine the feasibility of a regional delamination [*Levander et al*., 2011], we present a new Vs model based on a two-step inversion of Rayleigh wave data using the USArray data. This 3-D model provides absolute shear velocities allowing us to identify possible zones of partial melt at the CP edges, and produces the geometry of the lithosphere and asthenosphere for testing the delamination model at the western CP margin.

3.2 Data and Methodology

3.2.1 USArray stations and data analysis

The final Vs model provides crustal and upper mantle structures to ~200-250 km depth. We used phase and amplitude information of the fundamental-mode Rayleigh waves recorded by the TA network and several other seismic networks in the southwestern U.S. within the

geographic boundaries 32° to 50°N latitude, and 116° to 105°W longitude. Data from about 200 broadband seismic stations in the TA network (station spacing ~70 km) and 18 stations in other networks were incorporated in the analysis, as shown in Figure 3.1. We have used a total of 154 teleseismic earthquakes (30°≤Δ≤120°, Figure 3.2a) with shallow focus (≤70 km) and magnitude ≥ 5.5 which occurred between June 2007 and September 2009, when the TA occupied the CP region. The good azimuthal distribution of events and well-distributed stations provide extremely dense raypath coverage (e.g. Figure 3.2b), allowing for good resolution of stable lateral fluctuations in phase velocities measured across the plateau region and its adjacent provinces.

We processed the vertical components of the seismograms to extract the pure Rayleigh wave signals. After instrument response correction, we applied 18 Butterworth bandpass filters with 10 mHz bandwidth at center periods of 20, 22, 25, 27, 30, 34, 40, 45, 50, 59, 67, 77, 87, 100, 111, 125, 143, and 167s to the pre-selected traces (see example in Figure 3.2c). The filtered seismograms with either unusual amplitudes or low SNRs (<3) were excluded; only highly coherent and clean traces were kept for analysis. To isolate the fundamental mode from higher order modes and body wave phases, we windowed the surface waves with variable length tapered windows. The effects of frequency-dependent anelastic attenuation and geometrical spreading were taken into account for amplitude corrections [*Mitchell*, 1995; *Li et al*., 2003]. Local site responses were also considered to account for individual station corrections of both amplitude amplification and phase shift [*Yang and Forsyth*, 2006a]. Earthquake magnitude variations were removed by normalizing the observed amplitudes to the RMS amplitude for each event.

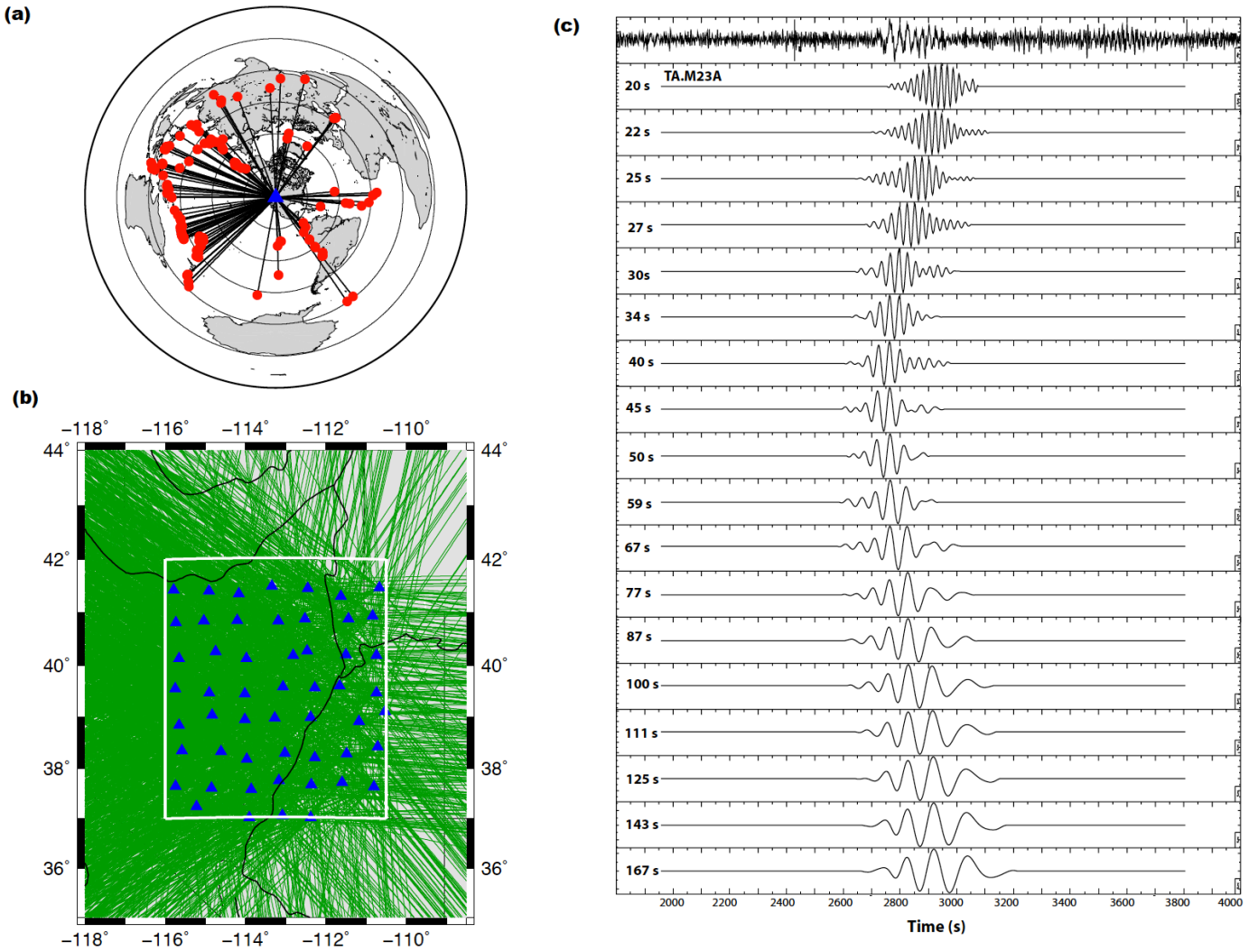

Figure 3.2 (a) Azimuthal distribution of earthquakes (red dots) centered on the CP (blue triangle). The neighboring concentric circles are in 30° increments. (b) Raypath (green lines) coverage at 50 s for the CP-NBR sub-region (white box). Blue triangles represent the stations. (c) An example of fundamental-mode waveform at different frequencies recorded at the M23A station for an earthquake (Magnitude 6.4, depth 35 km, epicentral distance 98.3º) on February 17, 2009. The raw data is shown at the top and was filtered into18 bands from 20 s to 167 s.

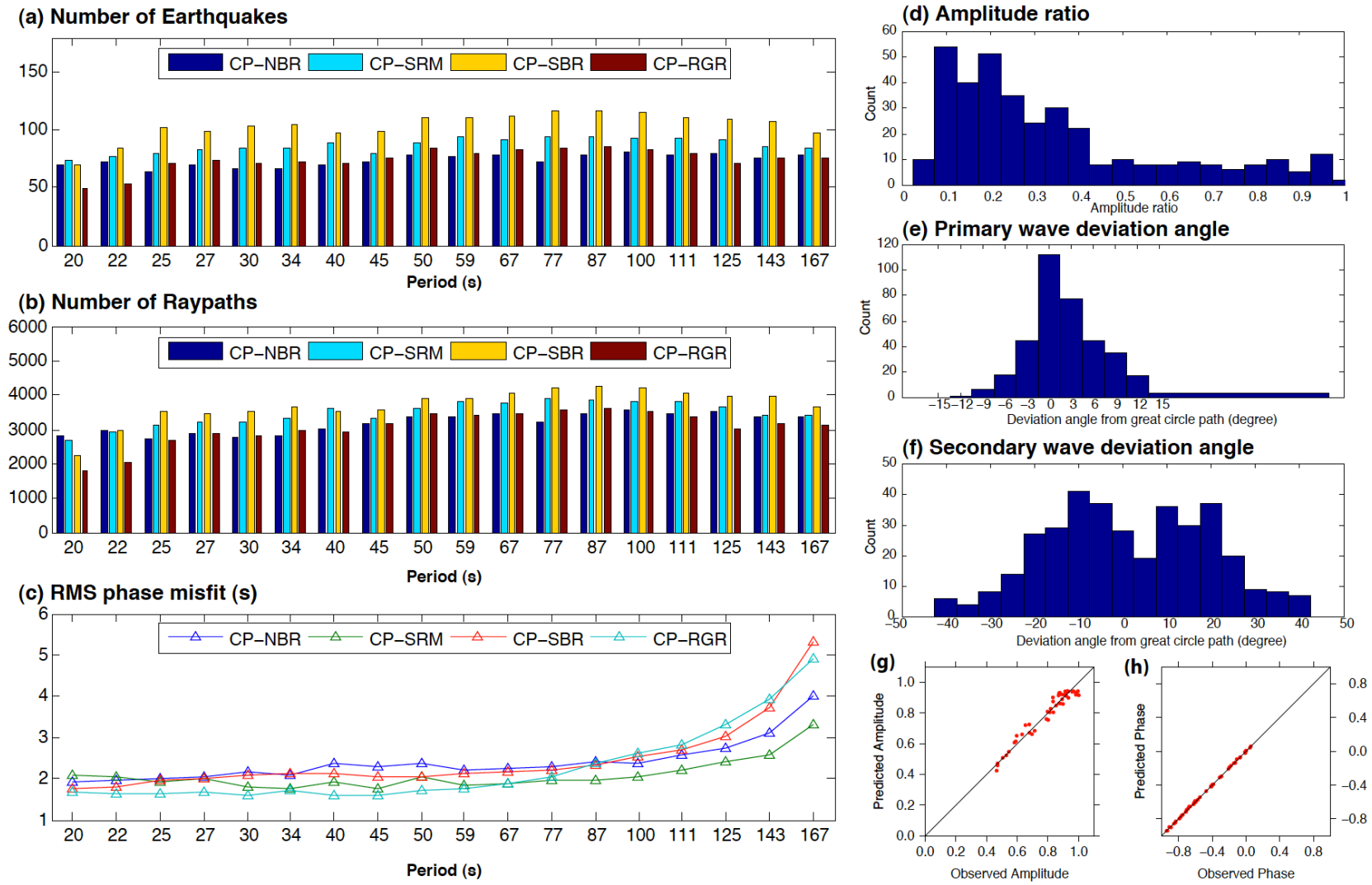

Figure 3.3 (a) Number of Rayleigh wave sources, (b) total number of raypaths, and (c) the phase RMS misfit for the phase velocity inversion at the four separate sub-regions: CP-NBR, CP-SRM, CP-SBR and CP-RGR. Statistics of the inversion results at 0.02 Hz (50 s) includes: (d) amplitude ratios, (e) deviation angles of the primary plane waves, and (f) secondary plane waves from the great circle path. Comparison of predicted and measured amplitude (g) and phase (h) data at 50 s for the CP-NBR sub-region.

3.2.2 Finite-frequency Rayleigh wave tomography

We have used the two-stage inversion developed by *Yang and Forsyth* [2006b] to determine the 3-D Vs structure from the phase and amplitude data. In the first step we obtain the 2-D phase velocities, with the modified two-plane-wave technique [*Yang and Forsyth*, 2006ab; *Forsyth and Li*, 2005], effectively unravelling interference in the Rayleigh wavefield resulting from multipathing. The method assumes that at a given frequency, the complexity and distortion of the fundamental-mode Rayleigh waves results from the sum of two interfering plane waves with different wave parameters (amplitudes, initial phases, angles of deviation from the great circle path). Additionally, we followed *Yang and Forsyth*'s [2006b] consideration of off-azimuth structures by introducing 2-D finite-frequency amplitude and phase sensitivity kernels to resolve localized wavelength-scale heterogeneities. This method for determining phase velocities, with and without the finite-frequency kernels, has been applied successfully to many datasets [*Forsyth et al*., 1998; *Li et al*., 2003, 2005; *Yang and Forsyth*, 2006a; *Yang and Ritzwoller*, 2008; *Schutt et al*., 2008; *Miller et al*., 2009].

The inversion of phase velocity coefficients and wave parameters uses both simulated annealing and a generalized linearized inversion technique [*Forsyth and Li*, 2005; *Tarantola and Valette*, 1982]. In this scheme, the perturbations to the current phase velocity model and wavefield parameters are iteratively updated, until they meet the numerical criteria for the misfit of phase velocities. Next, we inverted the local dispersion curves for 1-D Vs structures using the *DISPER80* code [*Saito*, 1988]. We used a similar iterative, linearized solution to the nonlinear least-square regional 1-D Vs inversion to construct a juxtaposed 3-D Vs model. The crustal thickness constraints are from RF estimates [*Levander and Miller*, submitted].

3.3 Parameterization and Inversion

3.3.1 Rayleigh wave phase velocity measurement

3.3.1.1 Parameterization

One basic assumption of the method is that the study region is small enough that the recorded waveforms can be represented as an interference pattern between two plane waves. We are examining a large area (11°×10°); therefore we first divided it into four sub-regions (Figure 3.1): CP-NBR, CP-SRM, CP-SBR, and CP-RGR. This division takes advantage of the dynamic deployment status of the TA stations. The phase velocities in the overlapping regions were averaged after separate subdivision inversion. Different events were chosen for each 'box' to maintain a good station coverage and similar azimuthal distribution (Figure 3.3a, b). A Gaussian averaging function with a smoothing length of 65 km was used in the relative traveltime calculation and to smooth the sensitivity kernels. Each 'box' is parameterized on an evenly distributed grid with a spacing of 0.5° in the receiver-covered region, and 1.0^{o} on the boundary to absorb traveltime residuals of the waves not modeled well by the two-plane-wave representation, a process accomplished by assigning larger *a priori* standard deviations to the peripheral nodes. The initial average phase velocities were estimated from the synthetic dispersion curve based on a modified TNA model.

3.3.1.2 Inversion and dispersion curves

The phase velocity variations from 20 to 167 s in each model 'box' were derived. Fewer seismograms at short periods (<30 s) were kept because of strong distortion and incoherent interference patterns among stations due to localized multipathing, focusing, or defocusing effects, and at longer periods (>100 s) due to the decreasing Rayleigh wave energy. The

mean phase RMS misfits (Figure 3.3c) are mainly below 3 s, indicating a good fit except at the longest periods (>143 s) that have larger uncertainties of phase measurements. In order to examine the validity of the two-plane-wave approximation we examine one single event (30 September, 2007) at 50 s (Figure 3.3 g, h), which shows the predicted phase and amplitude data fit the observations well. Moreover, for most filtered seismograms, the secondary/primary amplitude ratios are <0.4 (Figure 3.3d), and the deviation angles of the primary waves are <±10 degrees of the great circle path (Figure 3.3e, f). The small amplitude ratios and path deviations indicate that the TPWT representation is reasonable.

Several consistent phase velocity anomalies associated with the regional geological features are identified (Figure 3.4). We observe (1) a profound low-velocity area in the SRM at short periods (<50 s) associated with a relatively low crustal shear velocity and a thick crust beneath the Colorado Rockies; (2) at periods less than 30 s a large low-velocity area covering the Colorado Mineral Belt to the east of the CP; (3) relatively high phase velocities beneath the SBR which decrease abruptly upon entering the CP-SBR transition region; (4) two long NE-trending low-velocity belts along the CP-NBR and the Jemez lineament in the CP-RGR transition regions; (5) consistently high phase velocities in the CP interior compared to the surrounding tectonic margins; (6) at periods >45 s, the high velocity over the CP is continuous with the high phase velocity anomaly north of the CP, although it is variably reduced around its peripheries adjacent to the extended province to the west, south and east; and (7) high-velocities in the SBR at short periods (e.g. 20-30 s, Figure 3.4) which result from the shallow Moho, as Rayleigh waves in these periods sense upper mantle structures in the SBR, but the crust elsewhere.

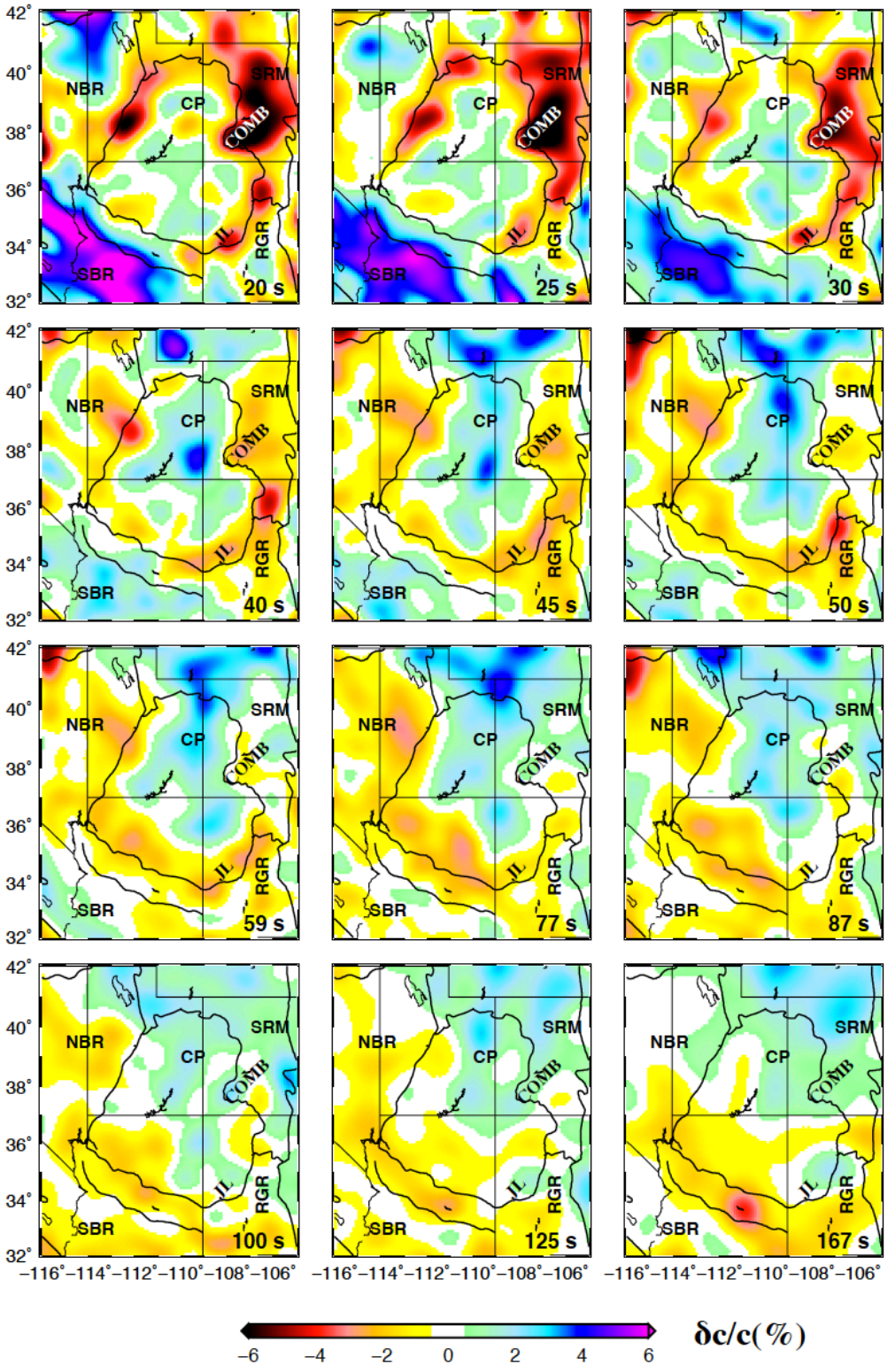

Figure 3.4 Rayleigh wave phase velocity maps at 12 of the 18 periods. The phase velocity inversions were performed separately on the four 0.5° × 0.5° grid sub-regions, created by cutting along two geographic lines at 110.5°W and 37°N, and were then combined by averaging the overlaps. COMB= Colorado Mineral Belt.

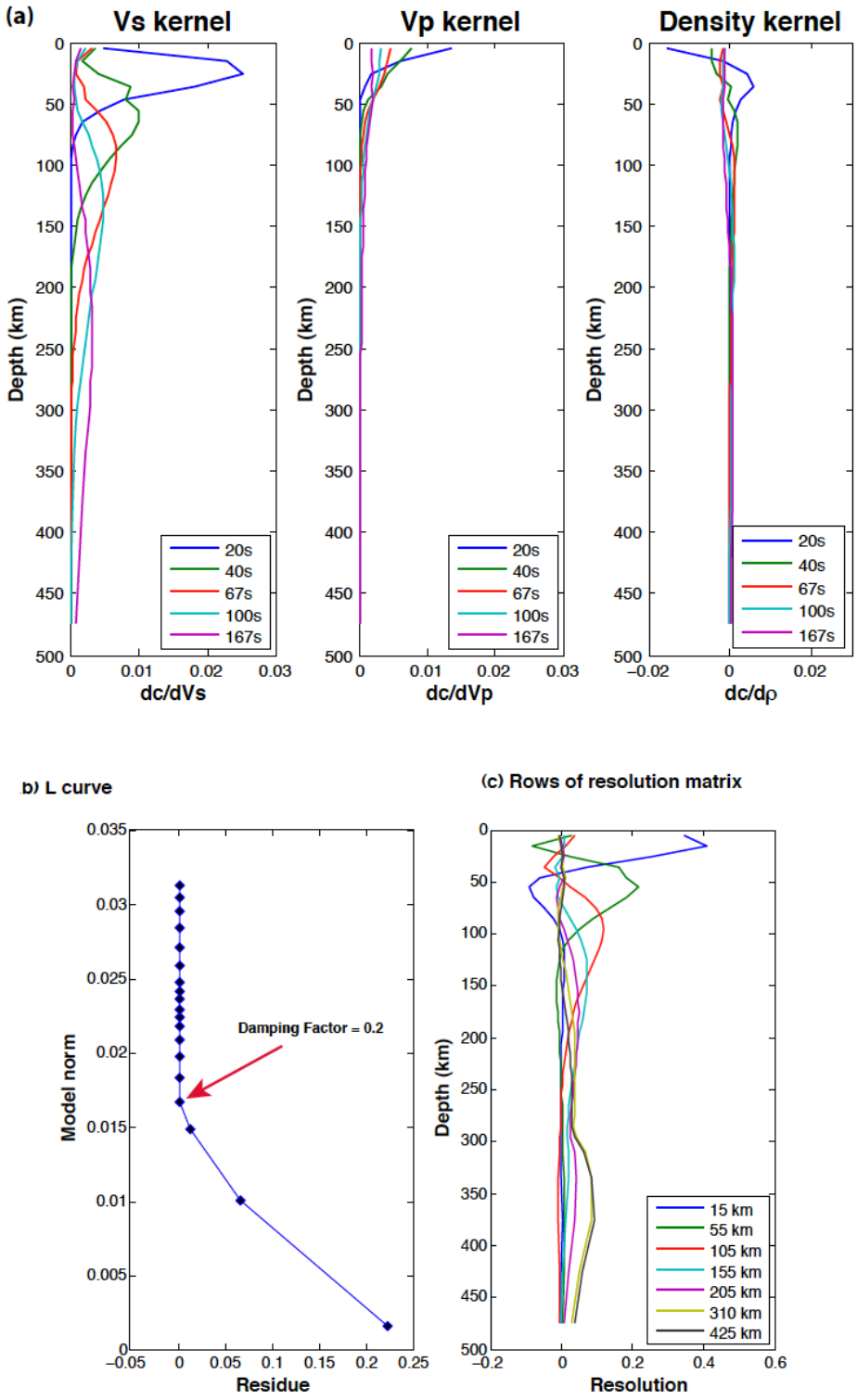

Figure 3.5 (a) Sensitivity kernel functions for Vs, Vp and density respectively at periods of 20, 40, 67, 100 and 167 s, based on the average Vs model. (b) Damping parameter estimation from the L-curve of the Vs model norm and residuals of the phase velocities. The turning point with damping parameter of 0.2 is chosen. (c) Model resolution kernels for layers at depths of 15, 55, 105, 155, 205, 310, 425 km. Rows of the resolution matrix are calculated from the reference model.

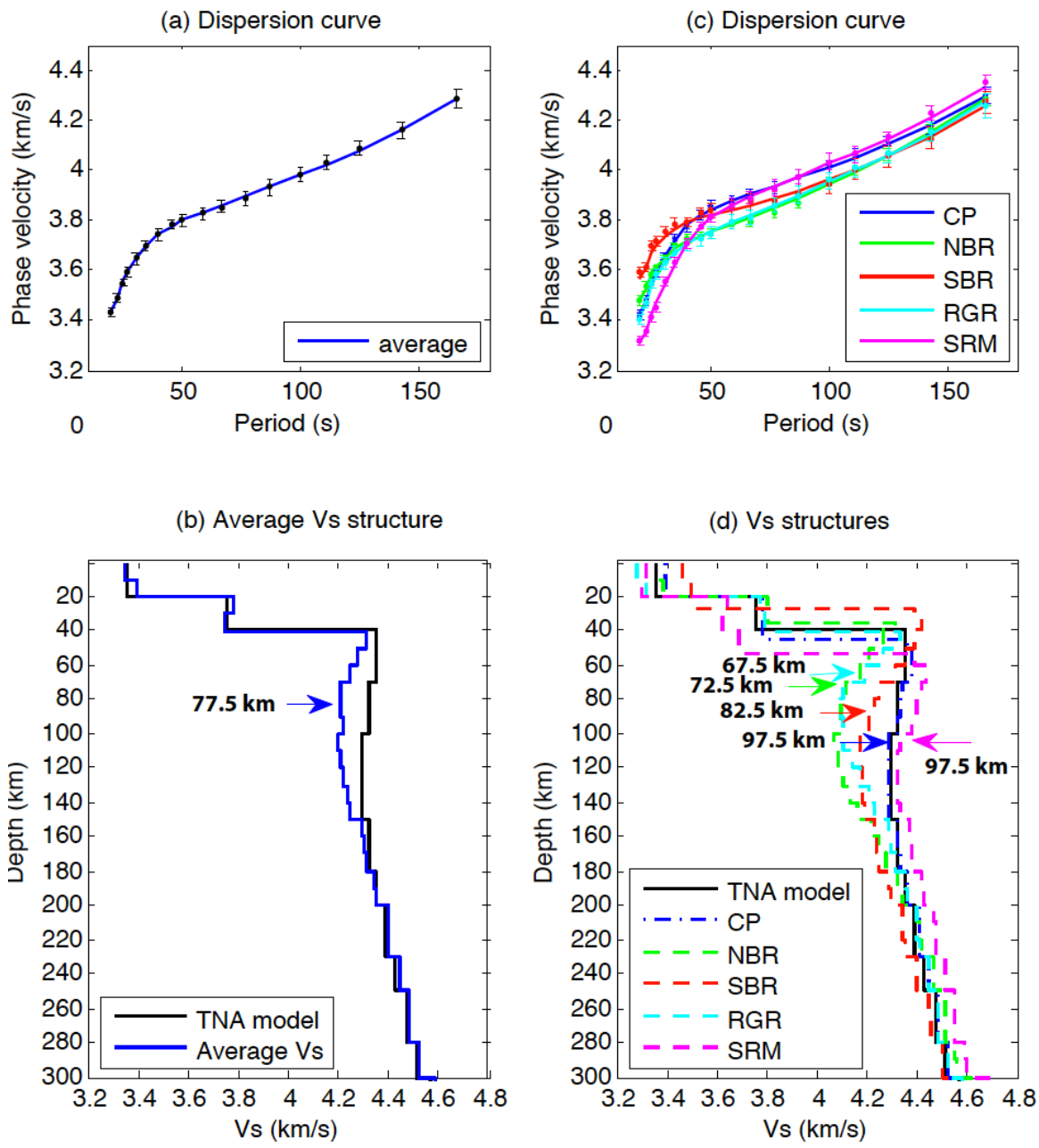

Figure 3.6 Dispersion curve fitting and Vs inversion. (a) The predicted dispersion curves for the average (blue) phase velocities. (b) The average Vs (blue) inverted from the starting modified TNA model (black) to fit the dispersion curve in (a). (c) The dispersion curves for five tectonic regions (CP, NBR, SBR, RGR and SRM). (d) The average Vs models beneath the corresponding geologic regions. The colors are the same as (c) for each region, and the black line is the initial TNA model. All error bars represent the standard deviation of phase velocity measurements. Estimated LAB depths from the Rayleigh wave tomography at the center of the negative velocity gradients.

3.3.2 Shear velocity inversion: parameterization and inversion

The phase velocities have significantly greater sensitivity to the absolute Vs than to density and Vp, especially below the Moho (Figure 3.5a). The vertical sensitivity kernels of Vp, Vs and density at various periods were computed based on the reference model, showing that the strongest sensitivity comes from the Vs profile. Thus, we kept density and Vp/Vs ratio fixed in each layer, and used a combined P- and S-wave sensitivity to calculate the perturbation to the previous velocity model. In practice, slightly varying the Vp/Vs ratio (1.70-1.85) caused no appreciable changes in the inversions. Thus, we finally used a fixed Vp/Vs ratio of 1.735 and 1.756 in the crust and upper mantle, respectively, the same as *Yang et al.* [2008] based on the statistical analysis of seismic parameters by *Chulick and Mooney* [2002]. The longest measured period (167 s) in the phase velocity indicates that the upper mantle structure can be well-resolved as deep as ~250 km, though with larger vertical uncertainties.

We iteratively inverted for Vs on the same 0.5°×0.5° grid used for computing the Rayleigh wave dispersion curves. The average Vs structure was first inverted by taking a mean crustal thickness of 42 km based on the modified TNA model. Then we inverted for the localized Vs at each grid-point using crustal thickness constraints from the RF study. The linearized inversion scheme uses a combination of minimum length and smoothing regularization by introducing nonzero diagonal and off-diagonal terms to the *a priori* model covariance matrix. A damping factor of 0.2 was suggested by the slope change in the L-curve (Figure 3.5b), and agrees well with the choice of *Schutt et al*. [2008] by bounding the minimum upper mantle Vs to a reasonable range.

The Vs inversion can be evaluated from the resolution kernels at different depths. The resolution lengths for the reference model are plotted in Figure 3.5 (c), with the resolution peak displayed around 20 km for the row of the resolution matrix corresponding to 15 km. The number of adjacent layers needed to recover one entire piece of independent information of the model increases with depth, due to broader and weaker resolution peaks. The combined analysis from the Vs sensitivity and resolution kernels indicates that the Vs can be well resolved to ~250 km depth, above which vertical and lateral heterogeneities are well imaged. The average Vs profiles beneath the entire region and the distinct tectonic regions are shown in Figure 3.6. We observe pronounced low-velocity zones beneath the SBR/NBR, the RGR and the SRM, which have been noted in many previous continental-scale studies [e.g. *Humphreys and Dueker*, 1994; *van der Lee and Nolet*, 1997; *Burdick et al*., 2008].

3.4 Results

3.4.1 Crustal heterogeneity

The crustal structure in the study region is characterized by several multi-scale (~50-100 km wide) high and low velocities (Figure 3.7a, b). Using the starting model (see Section 3.2) as the reference, we have imaged several distinct low-velocity features surrounding the plateau, including two narrow transition regions (~50-100 km wide) from the BRP, one beneath the SRM (Colorado Mineral Belt, Figure 3.7a, b), and one beneath the Jemez lineament near the RGR. The low crustal Vs anomalies (~150 km wide) beneath the CP-NBR transition region and the Colorado Rockies are broader than those in the CP-SBR transition region, and those beneath the Jemez lineament in the RGR-CP transition region (~100 km wide). The relatively high velocities (+3-4%) compared to the starting model under the SBR and NBR are

separated by a low-velocity area located in the 'magmatic gap' zone [e.g. *Armstrong and Ward*, 1991; *Zandt et al*., 1995]. The high NBR velocities drop abruptly to the east of the Wasatch Front. In the CP interior, the crust is relatively complex and has an intermediate average velocity between the low-Vs RGR (Figure 3.7a, b) and the high-velocity Great Plains [e.g. *van der Lee and Nolet*, 1997; *West et al.,* 2004]. The NE-trending high-velocity anomaly in the southern plateau is bounded by the Jemez lineament and the Yavapai/Southern Yavapai accretionary boundary (green dashed line in Figure 3.7a, b). It extends from the southeastern Navajo volcanic field region to the western edge of the SRM, and drops abruptly across the SRM-CP boundary into the Colorado Mineral Belt.

3.4.2 Upper mantle heterogeneity

We also observe strong lateral velocity heterogeneity in the upper mantle relative to the TNA model (Figure 3.7). A large high-velocity feature (+1-3%) beneath 50-70% of the CP between 60 and 200 km depth extends from the Navajo volcanic field in the south across the NE-striking Cheyenne Belt into the southern Archean Wyoming Province (Figure 3.7c-h). Encircling this feature in the east, south and west are continuous, large amplitude (-2 to -6%) low velocities extending to ~125-150 km depth. The largest-amplitude low-velocity anomaly is located beneath the NBR to the west of the Wasatch Front (Figure 3.7c-h). A NE-trending narrow low-velocity belt (Figure 3.7f-h) bisects the Four Corners high-velocity body.

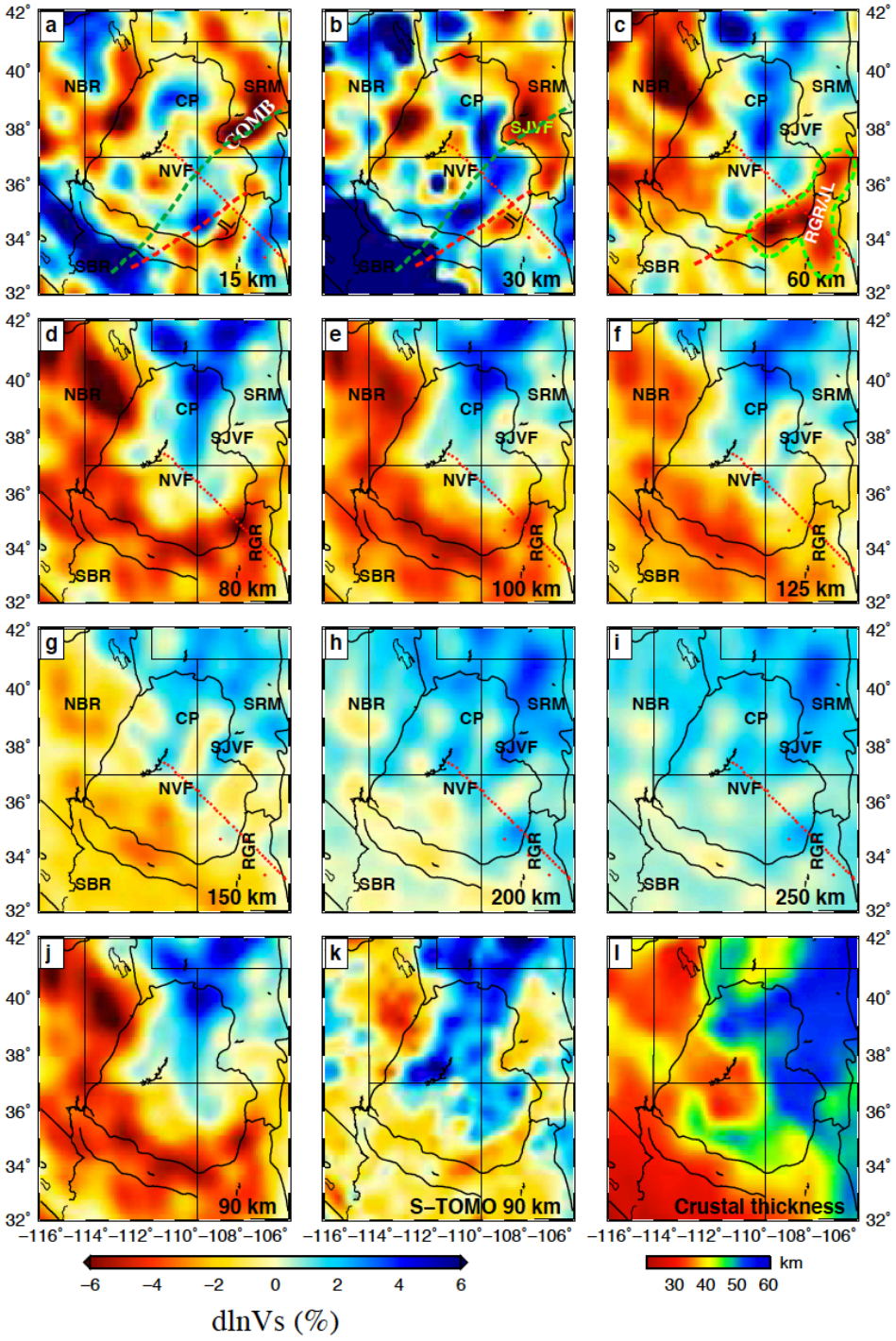

Figure 3.7 Vs anomalies (a-i) at depths of 15-250 km relative to the TNA model, and comparison of Vs at 90 km from this study (j) and the body wave tomography (k) [*Schmandt and Humphreys*, 2010]. Red and Green dashed lines are the Yavapai/Southern Yavapai and Yavapai/Mazatzal accretionary boundaries, respectively. The 'λ' anomaly (green dashed contour) is shown in (c). The crustal thickness (l) is estimated from the Ps RFs [*Levander and Miller*, submitted]. SJVF=San Juan volcanic fields, NVF=Navajo volcanic fields, COMB= Colorado Mineral Belt, JL=Jemez lineament. The red dotted line shows the station distribution of the La RISTRA experiment.

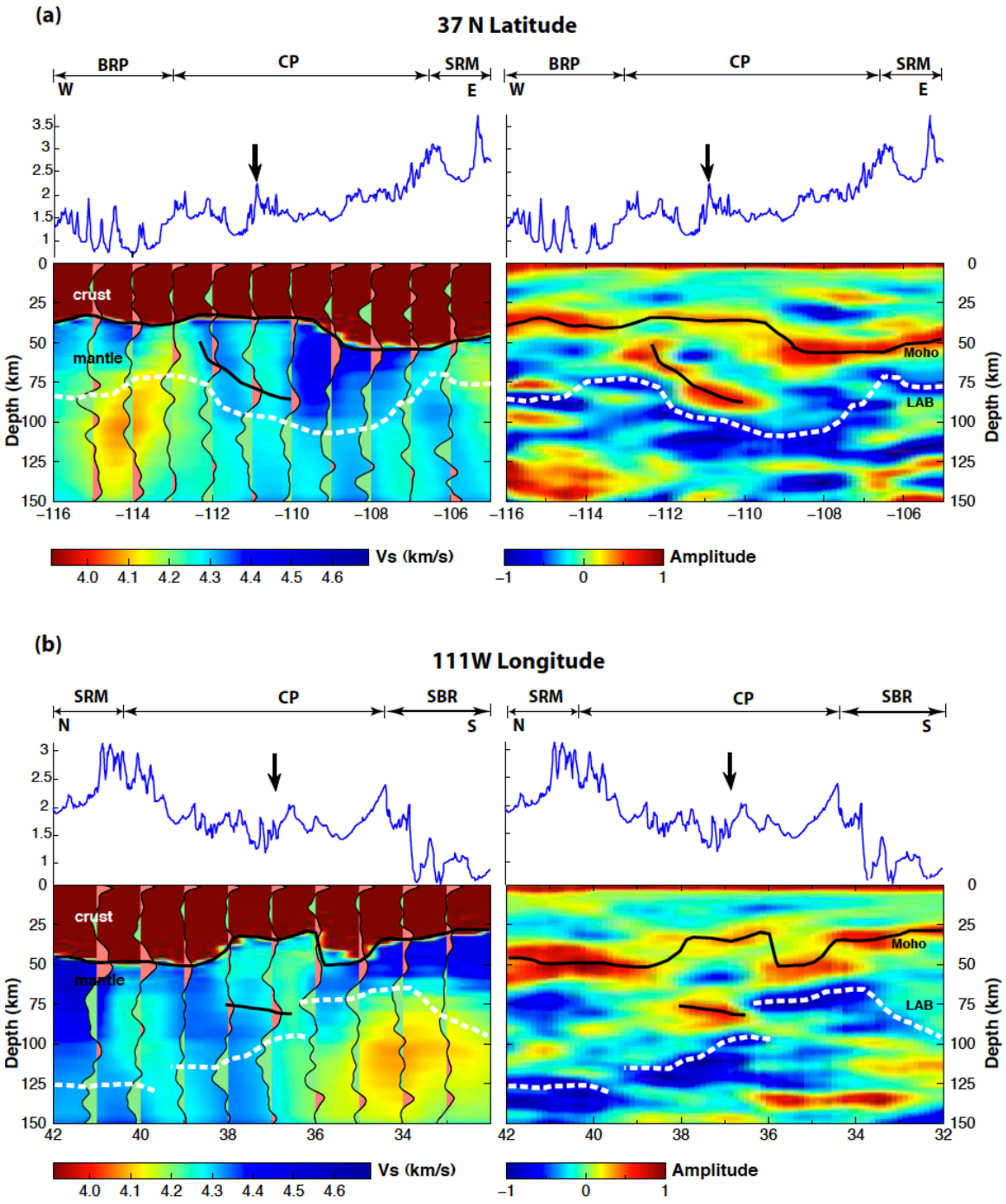

Figure 3.8 Comparison of cross-sections of Vs structure (left) and 1.25 Hz Ps RF images (right) along 37°N (a) and 111°W (b). Top of each image shows the elevation along the lines with arrows pointing at the Monument uplift (MU) where the delamination may start. The crustal velocity is set to a constant 3.9 km/s for display and plotted RF profiles (positive in light red and negative in light green) on the Vs cross-sections. Black solid lines and white dashed ones indicate the Moho and LAB depths, respectively, estimated from the RFs.

In the southeast, a 'lambda-shaped' (λ) low-velocity body (green dashed contour in Figure 3.7c) is observed beneath the southern RGR and the Jemez volcanic fields (RGR/JL) (Figure 3.7c-e). The two low-velocity trends of the 'λ' merge close to the New Mexico-Colorado border, and extend northward into the SRM as Vs increases. The lowest shear velocity, ~8% lower than the global average, lies beneath the RGR axis where it crosses the Jemez lineament (Figure 3.7c-e), in the depth range ~40 to 100 km. Below 100 km, the 'λ' anomaly (Figure 3.7f, g) is lost to larger-scale SBR low velocities. The velocity contrast between the Jemez lineament and the Four Corners high-velocity anomaly is large at ~10%. The low velocities in the RGR are bounded by higher velocities along the easternmost edge of the rift, where surface deformation in the western U.S. has largely ceased. At depths above 200 km (Figure 3.7c-g), the upper mantle Vs peak-to-peak variations can reach as high as 12%. Weakening of the observed lateral heterogeneity at greater depths (>200 km, Figure 3.7h, i) is likely due to the loss of sensitivity and the lateral averaging effect of long-period Rayleigh waves, although it might also reflect the nature of the mantle heterogeneity at these depths.

3.4.3 LAB depth estimate

The Rayleigh wave tomography model provides an independent estimate of the LAB depth under and adjacent to the plateau. *Sensu stricto* the LAB is a rheological boundary separating the conductive and rigid lithospheric lid from the convective and mechanically weak asthenosphere. Proxies for the LAB are often taken as geophysical discontinuities or vertical gradients in geophysical properties, negative in the case of seismic velocity, seismic impedance, or viscosity, and positive in the case of heat flow and electrical conductivities [*Eaton et al*., 2009; *Fisher et al*., 2010; *Abt et al*., 2010]. The Ps and Sp RF techniques [e.g. *Langston* 1979; *Li et al*., 2007] have been developed to detect such seismic impedance

discontinuities effectively. However, the LAB depth is still sometimes ambiguously defined from RF images alone [*Rychert and Shearer*, 2009; *Yuan and Romanowicz*, 2010]. Additional constraint from the surface wave model, which is an estimate of absolute shear velocity, improves the determination of LAB depths. The LAB topography in the tectonically active southwestern U.S. is an important constraint for determining the geodynamic evolution of the BRP/RGR and the little-deformed CP, and for estimating the location of partial melts, which were probably generated and transported from greater depth in the upper mantle, and now reside under the young volcanic fields in the BRP and RGR regions. Detailed knowledge of the regional-scale mantle convection and thermal structures also depends significantly on the accuracy of the LAB topography.

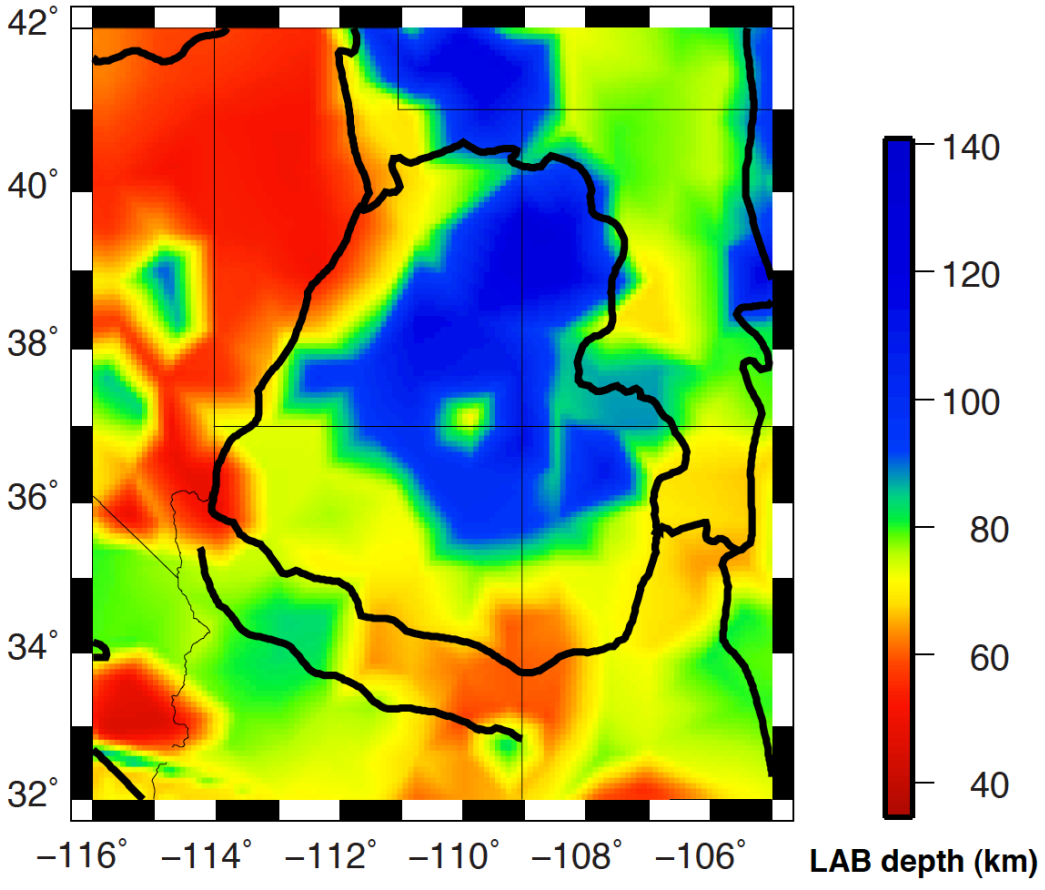

Figure 3.9 LAB depth interpreted from the combined RF-Rayleigh wave tomography analysis.

We obtained a new LAB map (Figure 3.9) by using the surface wave Vs model as a guide to pick the LAB depth from the Ps RF images. We first take the center of the negative upper mantle Vs gradient as the LAB [*Eaton et al*., 2009; *Fisher et al*., 2010], and compare it to the 3-D Ps and Sp RF volumes using the CCP stacking technique [*Dueker and Sheehan*, 1997; *Levander et al*., 2011]. There is good agreement between these two independent LAB depth estimates (Figure 3.8) though they are made from signals in different frequency bands (0.1-1.0 Hz for the RFs; 0.006-0.05 Hz in Rayleigh waves). For example in Figure 3.8, the LAB depth estimates at ~60-120 km from the RF images are, in most locations, well-correlated with the top of the low velocities in the Vs images, in which selected RF profiles are plotted for direct comparison. The tomography Vs image reduces the ambiguity in choosing the LAB in Ps RFs where the negative converted Ps phase from the LAB is obscured by crustal multiple reflections. Due to the inherent smoothness of inverted gradients beneath the lithospheric high-velocity lid, using both surface wave inversion and RF images allows for distinction between multiple permissible LAB depth estimates. Thus, we finally picked the LAB depth from the RFs and the Vs profiles jointly.

From the newly determined LAB map (Figure 3.9), we observe that the LAB beneath the BRP and RGR is relatively shallow at ~50-80 km depth. It is deeper beneath the CP at ~80-120 km, and becomes even deeper beneath the SRM to >150 km. The average LAB depths beneath each tectonic province show good agreement with depths inferred as the center of the negative-velocity gradient from the average Vs profiles (Figure 3.6). However, the relatively deep LAB (>85 km) of the plateau does not coincide with the physiographic province

boundary: the abrupt lithospheric deepening beneath the CP lies within the plateau, not at the edges near the BRP/RGR (Figure 3.9).

3.5 Interpretation and Discussion

The surface wave inversion results are consistent with numerous previous regional-scale or 2-D seismic studies such as PACE [e.g. *Wolf and Cipar*, 1993; *Benz and McCarthy*, 1994], Deep Probe [e.g. *Henstock et al.*, 1998; *Snelson et al.*, 1998], CD-ROM [e.g. *Levander et al.*, 2005; *Snelson et al.*, 2005], La RISTRA [e.g. *West et al.*, 2004; *Gao et al.*, 2004; *Wilson et al.*, 2005ab], and CP-GB [e.g. *Sheehan et al.*, 1995, 1997]. In addition, our model provides a 3-D examination of the complicated CP lithospheric structures over a wider region. The complicated lateral heterogeneity of the crustal and upper mantle Vs structures above 80 km can be attributed to Cenozoic magmatic modifications and tectonism around the plateau periphery, such as melt generation during the magmatic encroachment towards the CP center [*Roy et al.*, 2009], the possible warming from the extension around the margins, and the small rotation of the plateau [e.g. *Aldrich et al.*, 1986]. The thin BRP and RGR lithosphere result from Cenozoic extension, while the relatively thick central CP lithosphere is consistent with geologic observations that the plateau has experienced little internal deformation [*Thompson and Zoback*, 1979; *Morgan and Swanberg*, 1985]. Our results are in good agreement with the P and S body-wave traveltime tomography results from *Schmandt and Humphreys* [2010], but have greater vertical resolution at shallow depths (<200 km). For example, comparing the Vs map at 90 km (Figure 3.7j, k), there appears to be similar lateral variation patterns with a large and continuous low-velocity anomaly surrounding the Four Corner high velocities from both methods. The slightly different magnitudes of anomalies can be attributed to radial anisotropy caused by continental deformation [*Moschetti et al.*,

2010]. Despite the larger station spacing of TA stations (~70 km), a cross section through our Vs volume shows similar high and low-velocity anomalies as the more densely spaced (~20 km) La RISTRA experiment cross-section [*Sine et al*., 2008].

Moreover, the surface wave model provides absolute Vs information rather than velocity perturbations derived from teleseismic body-wave tomography [e.g. *Schmandt and Humphreys*, 2010; *Sine et al*., 2008]. For instance, absolute velocity models can provide accurate traveltime computation, while, in contrast, the body-wave tomography may give a biased result if using an incorrect reference model. Specifically, the absolute Vs can better constrain the upper mantle physical state in the Southwestern U.S. For example, the lowest seismic velocities seen in Figure 3.11 are strongly correlated with locations of Late Cenozoic magmatism and high surface heat flow. We suggest that thermo-chemical convection occurs progressively inward into the plateau, removing the rehydrated and weakened parts of the CP lithosphere, and this convective process leads to magmatic migration inboard and produces a thinned lithospheric thickness and a low-velocity zone across the edge. At the western margin, a regional lithospheric downwelling process has been suggested by our surface waves, body wave tomography, and RFs [*Levander et al*., 2011], and illustrates ongoing thermo-chemical convection involving the lowermost crust and upper mantle. This type of downwelling can help to explain how lithospheric mantle has been removed around the CP, and how the crust in the CP-BR transition regions is thinned.

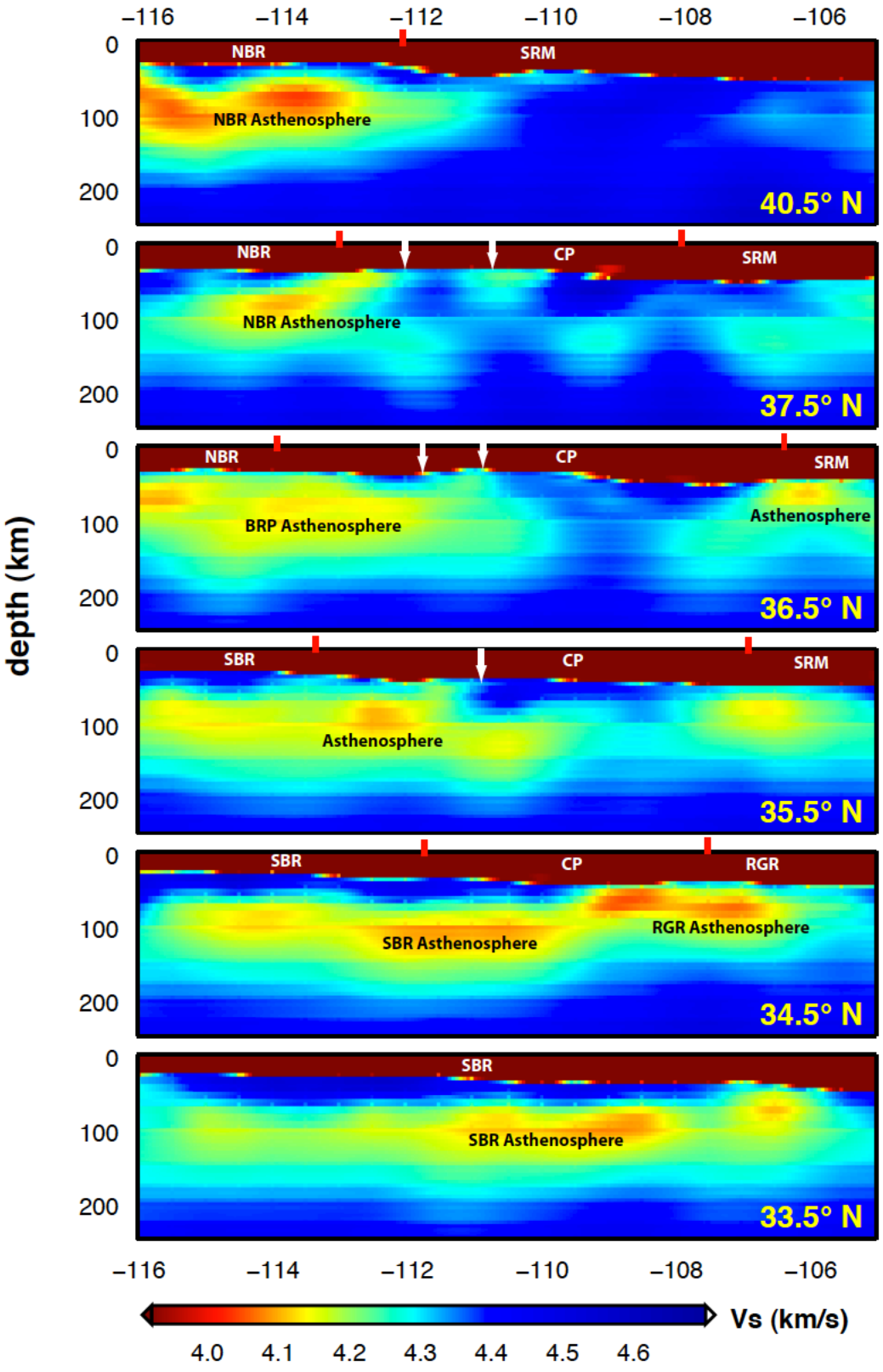

Figure 3.10 Vs cross-sections along east-west traverses (labeled in bottom right) showing LVZ location, with tectonic boundaries marked in red ticks and delamination location in white arrows.

3.5.1 Upper mantle low-velocities

In addition to the top of the LVZ that we interpreted as the LAB, the base of the upper mantle LVZ can also be estimated from the Vs images, although with larger uncertainties due to loss of vertical resolution at greater depths [*Eaton et al*., 2009]. From the Vs cross-sections (33.5°-40.5°N) in Figure 3.10, we observe that the LVZ shape changes significantly beneath different tectonic provinces. The LVZs beneath both the NBR and SBR are very shallow (top at ~55-70 km) and thin (~90-120 km thick), and reach extremely low values (Vs <4.15 km/s) at ~80-100 km depth under the transition region at the CP edge. The RGR/JL system has a shallower LAB (~50 km), a thinner LVZ (~70-90 km thick), and the minimum Vs (<4.0 km/s) at shallower depths of ~60-70 km. The southernmost SRM has a LVZ at a similar depth as the RGR/JL system, but the absolute value of the lowest Vs increases northward by ~2-5%. There is no obvious well-defined LVZ beneath the northern plateau, although the LAB depth can still be roughly estimated from the small negative gradient in the Vs profiles. The penetration distances of the LVZs (SBR: ~100-150 km; NBR: ~50-100 km), which extend across the CP boundary into the lithospheric core, correlate well with the eroded CP lithosphere inferred from the LAB topography obtained in this study (Figure 3.9). Assuming that the magmatic encroachment started from the edge at ~20 Ma when BRP extension initiated with a uniform rate, we obtained a lateral rate of 5-7.5 km/Ma and 2.5-5 km/Ma from the SBR and NBR sides, respectively, which agrees well with the migration rates of surface volcanism presented by *Roy et al*. [2009]: SBR ~6.3 km/Ma; NBR ~4.0 km/Ma.

Seismic velocity reduction is typically ascribed to changes in temperature [e.g. *Karato*, 1993; *Cammarano et al*., 2003], volatile composition [e.g. *Karato and Jung*, 1998], degree of

partial melt and melt depletion [e.g. *Hammond and Humphreys*, 2000; *Schutt and Lesher*, 2006], as well as seismic anisotropy [e.g. *Yang and Forsyth*, 2008] and grain size [e.g. *Faul and Jackson*, 2005]. The extremely strong Vs contrast (~12-14%) across ~80-125 km in the transition regions (Figure 3.7 d-f) cannot be simply caused by temperature variations, which require a physically unreasonable difference of ~600-900 K, if we used a temperature derivative $\delta \ln Vs/\delta T$ of ~1.5-2.3%/100K [*Karato*, 1993; *Cammarano et al*., 2003] and upper mantle attenuation Qs of ~50-100 [*Faul and Jackson*, 2005; *Sine et al*., 2008; *Yang and Forsyth*, 2008; *Dalton et al*., 2008]. The presence of a small amount of partial melt in the upper mantle LVZ can dramatically reduce the shear velocity and thus requires more reasonable temperature variation. *Hammond and Humphreys* [2000] suggested that a ~1% melt fraction in the upper mantle could cause at least a 7.9% reduction in shear velocity. If we assume ~1% partial melt in the low-velocity ring (Figure 3.11), the remaining Vs reduction can be caused by a lateral temperature variation of ~170-400 K, consistent with the 200-400 K temperature change suggested from xenolith data [*Riter and Smith*, 1996]. The required percentage of melt might be higher if we use the measurement by *Takei* [2000], which gives ~2-4% variations in Vs caused by 1% partial melt in the upper mantle. Compositional variations caused by hydration or melt depletion could also contribute a certain percentage to Vs reduction, but the contribution is too small to account for the observed Vs variations. Typically, no more than 0.5% change in Vs can be caused by the melt depletion in the upper mantle [*Schutt and Lesher*, 2006]. We interpret the upper mantle low velocities as resulting from a ~1% partial melt fraction in the lowest velocity regions of the BRP, RGR and the southern and western peripheries of the CP. This has been previously suggested by *Schmandt and Humphreys* [2010] from body-wave tomography, in which they

observed low Vp, Vs, and high Vp/Vs. The partial melt could either be partially molten lithosphere whose solidus was depressed by hydration, or asthenospheric mantle. Geochemical data [e.g. $^{143}Nd/^{144}Nd$ ratios from *Crow et al*., 2011] suggest that the melt source around the plateau rim has an increasingly asthenospheric signature through time. The locations of the asthenospheric low-velocity zones containing partial melt are strongly correlated with the existence of Holocene volcanic fields, which include the Valles Caldera and Zuni Bandera fields in the Jemez lineament, the San Francisco and Uinkaret fields on the southwestern edge, and the Markagunt Plateau and Bald Knoll, Santa Clara, and Black Rock Desert fields in the northwestern margin of the plateau (Figure 3.11).

3.5.2 Edge convection around the Colorado Plateau

The 3-D scenario of edge convective erosion occurring around the CP boundary could be either an extension of 2-D edge driven thermal convection suggested by *van Wijk et al.* [2010], or numerous consecutive 3-D thermo-chemical convective events removing the lower crust and mantle lithosphere proposed by *Levander et al.* [2011], or both. In the latter case, erosion occurs by repeated localized drips, in the former by sheet-like drips. From the present-day configuration of the asthenospheric LVZs abutting the relatively high-Vs lithospheric core of the CP, we suggest that widespread small-scale convection is occurring at more than half of CP margins from the RGR to BRP to explain the present-day thinned lithosphere, localized uplift and magmatism at the edges. The shallowing trend of the LAB and base of the LVZs toward the plateau center could be related to the increasingly asthenospheric components observed toward the center of the plateau due to mantle upwelling [*Sine et al*., 2008; *Crow et al*., 2011].

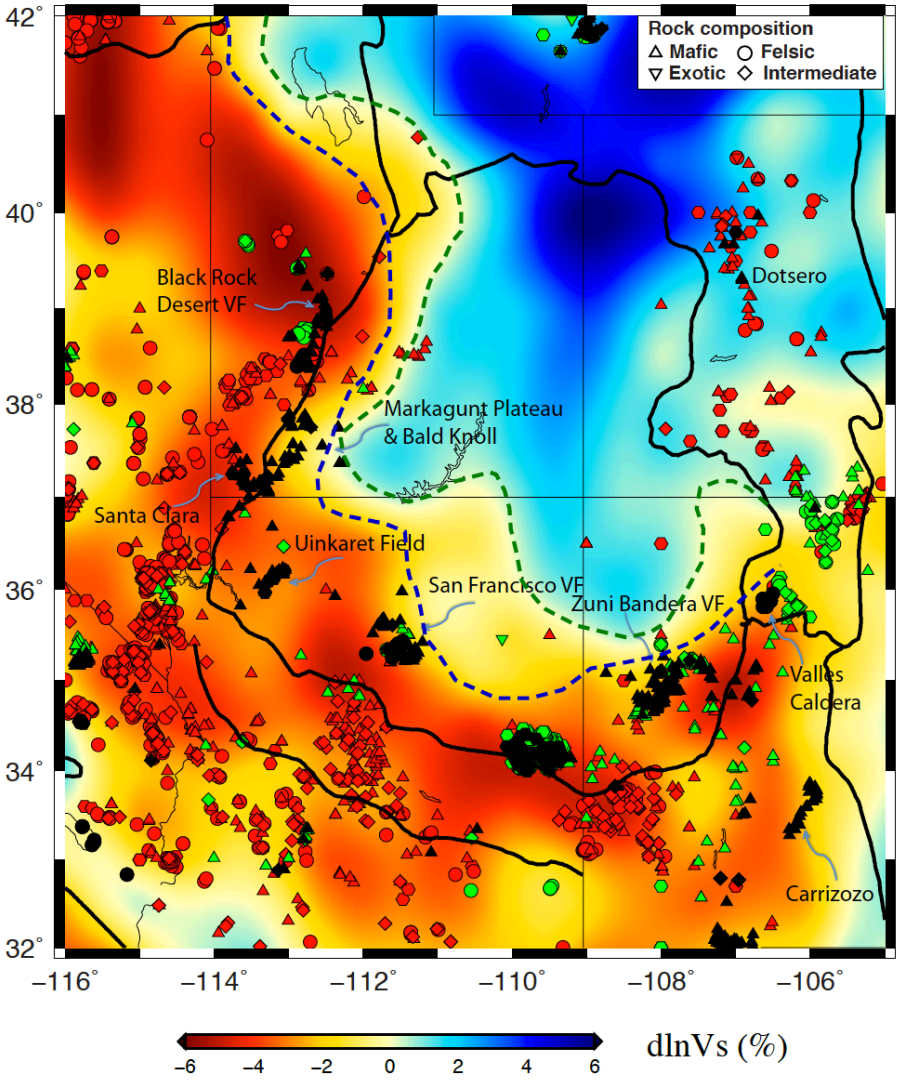

Figure 3.11 Rayleigh wave tomography Vs perturbation relative to TNA at 90 km depth. The types of the igneous volcanic rock compositions are plotted as different symbols as shown in the right upper corner (data from Western North American Volcanic and Intrusive Rock Database). The age of the rock is indicated by the fill color, where red means Miocene (23.7-5.3 Ma), green means Pliocene (5.3-1.8 Ma), and black means Quaternary (<1.8 Ma). The major Holocene volcanic fields located at the CP edges, including Black Rock Desert volcanic field (VF), Markagunt Plateau and Bald Knoll, Santa Clara, Uinkaret field, San Francisco VF, Zuni Bandera VF, Valles Caldera, Dotsero and Carrizozo. The blue dashed line is the contour of the low-velocity boundary coinciding well with the young magmatism, and the green dashed contour shows the high-velocity Proterozoic lithosphere.

Widespread edge convection was probably developed initially from the large variations in lithospheric thickness (Figure 3.9) between the mildly deformed CP and the extended and thinned BRP and RGR since mid-Cenozoic, resulting in convective erosion of the CP thermal

boundary layer as suggested by *van Wijk et al*. [2010] to explain the large Vs gradient and the magmatic invasion. Furthermore, we suggest that pervasive convective removal of both the thermal boundary layer and lithospheric core of the plateau has been progressively occurring across large parts of the periphery toward the northeastern cratonic root. The 3-D scenario of marginal erosion initiated from the large step of lithospheric thickness could be facilitated by rehydration and destabilization of CP lithosphere [*Humphreys et al*., 2003; *Li et al*., 2008]. Edge-driven convection itself cannot dramatically erode the abutting lithosphere without introducing substantial weakness inside the lithospheric root [*King and Anderson*, 1998]. Mantle xenolith evidence shows that the cold CP lithosphere, despite its depletion and little internal deformation, was rehydrated by subduction-released water and was further refertilized and mechanically weakened [*Li et al*., 2008; *Roy et al*., 2009]. The CP lithosphere, with significantly reduced viscosity at its base and flanks, is being convectively removed at a similar rate as the volcanic migration toward the CP interior although the process may be more three-dimensional than two-dimensional as suggested by the delamination-style downwelling over the Grand Canyon [*Levander et al.*, 2011].

Our Vs model suggests that sub-continental convective processes might continue to erode and recycle the entire hydrated and destabilized lithosphere, and we predict core-ward migration of low-velocity zones and thinned lithosphere. The convective erosion of the previously hydrated CP lithospheric core and the replacement by the lower-density asthenosphere contribute additional buoyancy at the western and southeastern edges. The uplift of the CP margins could further be facilitated by the thermal expansion from basal and side heating [*Roy et al*., 2009]. Combining our new upper mantle Vs model and the

geochemical analysis from *Crow et al*. [2011], we suggest that much of the low-velocity volume surrounding the plateau is associated with asthenospheric replacement of the CP lithosphere stripped off by convective erosion across the margins at various depths from the base of the crust to ~150 km.

3.5.3 Lithospheric delamination and CP uplift

Cross-sections of the Vs model support the ongoing regional delamination hypothesis in the western CP, as suggested by RFs, body wave tomography [*Levander et al*., 2011]. The CCP stacked RF images reveal unusually complicated Moho topography beneath the western portion of the plateau, where the conversion signals broaden and separate into two distinct positive-amplitude events (Figure 3.8). The top event is relatively shallow and is interpreted as a newly formed 'elevated' Moho. The deeper one extends to depths of 70-90 km and is interpreted as the upper interface of a delamination-style, convective downwelling that includes the lower crust and upper mantle lithosphere [*Bird*, 1979; *Levander et al*., 2011]. This feature appears in the teleseismic body wave tomography [*Schmandt and Humphreys*, 2010] as a high velocity pipe extending to 200-250 km depth. In both seismic datasets, the feature is centered at about 37°N latitude and 111°W longitude, with a radius of ~100 km.

At this point, the Rayleigh wave tomography shows high velocities that start at ~80 km depth and extend to the northeast to at least 100 km. Figure 3.8 shows a comparison of two cross-sections from the RF and Rayleigh wave studies. The crustal thickness constraint in the Rayleigh wave phase velocity inversions is from the RF estimates as we describe below. To the west of the Navajo volcanic field (113-111°W in Figure 3.8a), a relatively high-velocity anomaly is imaged as hanging to the western edge of the plateau. Along the N-S profile, we

also observed a high-velocity anomaly about 100 km across in the Vs image, the top of which correlates well with the top of the delamination event shown as the deeper positive Ps conversion in the RF image. The detachment direction indicates that the delamination of the lower crust and lithosphere propagates from the plateau interior toward the western margins of the plateau. This is consistent with increasing uplift rates in the Grand Canyon from west to east inferred from the incision history [*Karlstrom et al*., 2008; *Levander et al*., 2011]. The low-velocity region (111-110°W) east of the lithospheric drip, interpreted as the buoyant asthenosphere, is replacing the delaminating lithospheric mantle and lower crust.

To test the robustness of the high-velocity structure beneath the delamination region, we have inverted the Vs structures using three different crustal thickness constraints (shallow, constant at 40 km, and deep Moho) beneath the western plateau. The shallow and deep Moho depths correspond to the shallow and deep events in the RF image (see Figure 3.8a), respectively. As anticipated, the lower crust and uppermost mantle velocity structures are greatly affected by different Moho constraints. However, we consistently observe the northeasterly dipping high-velocity feature in all the three Vs inversions, surrounded by low velocities from both sides in the west of the Navajo volcanic field (Figure 3.12). The consistent pipe-like upper mantle structures discount the possibility of an artifact introduced by an incorrect crustal thickness constraint. The shallow Moho inversion is preferred in this study because the data from the top positive event in the RF analysis is more physically reasonable since it is above 50 km. Moreover, the shallow Moho model produces the smallest residuals (<0.5%) in the inversion at about 3-5 grid points over this region 36°-38°N,

compared to the deep Moho model (Figure 3.13). The constant Moho model has similar residuals to the shallow model since their Moho depths are close (Figure 3.13).

Our Vs model and inferred LAB topography, as well as the edge convection and regional downwelling, provide possible mechanisms for the complicated CP uplift observations at the margins. The crustal thickness from either active source data [*McCarthy and Parsons*, 1994; *Wolf and Cipar*, 1993, *Henstock et al*., 1998; *Snelson et al*., 1998] or Ps and Sp RFs [*Levander and Miller*, submitted] is inadequate to provide isostatic support for the ~1.8-2 km CP elevation. The preserved Proterozoic CP lithosphere, inferred from the high Vs in the core of the plateau and its thickness of ~100 km (Figure 3.6, 3.9), makes the almost complete lithospheric removal following flat-slab subduction *Bird* [1988] seem unlikely to us. Mantle compensation for the CP buoyancy is thus required; however, it cannot be fully explained by a single buoyancy source. Instead, we suggest several types of support that include dynamic uplift from a deep mantle upwelling [*Moucha et al*., 2008, 2009; *Liu et al*., 2010], basal/side heating and thermal expansion [*Thompson and Zoback*, 1979; *Roy et al*., 2009], partial removal of lower crust and lithosphere components [*Spencer*, 1996; *Lastowka et al*., 2001; *Levander et al.*, 2011], and small-scale convective support along the CP margins [*van Wijk et al*., 2008, 2010]. Though it is still difficult to quantify the buoyancy contribution from each mechanism [e.g. *Roy et al*., 2009], our model suggests that both the edge convective asthenospheric source and the regional delamination can cause additional elevation at the western, southern, and southeastern margins of the plateau.

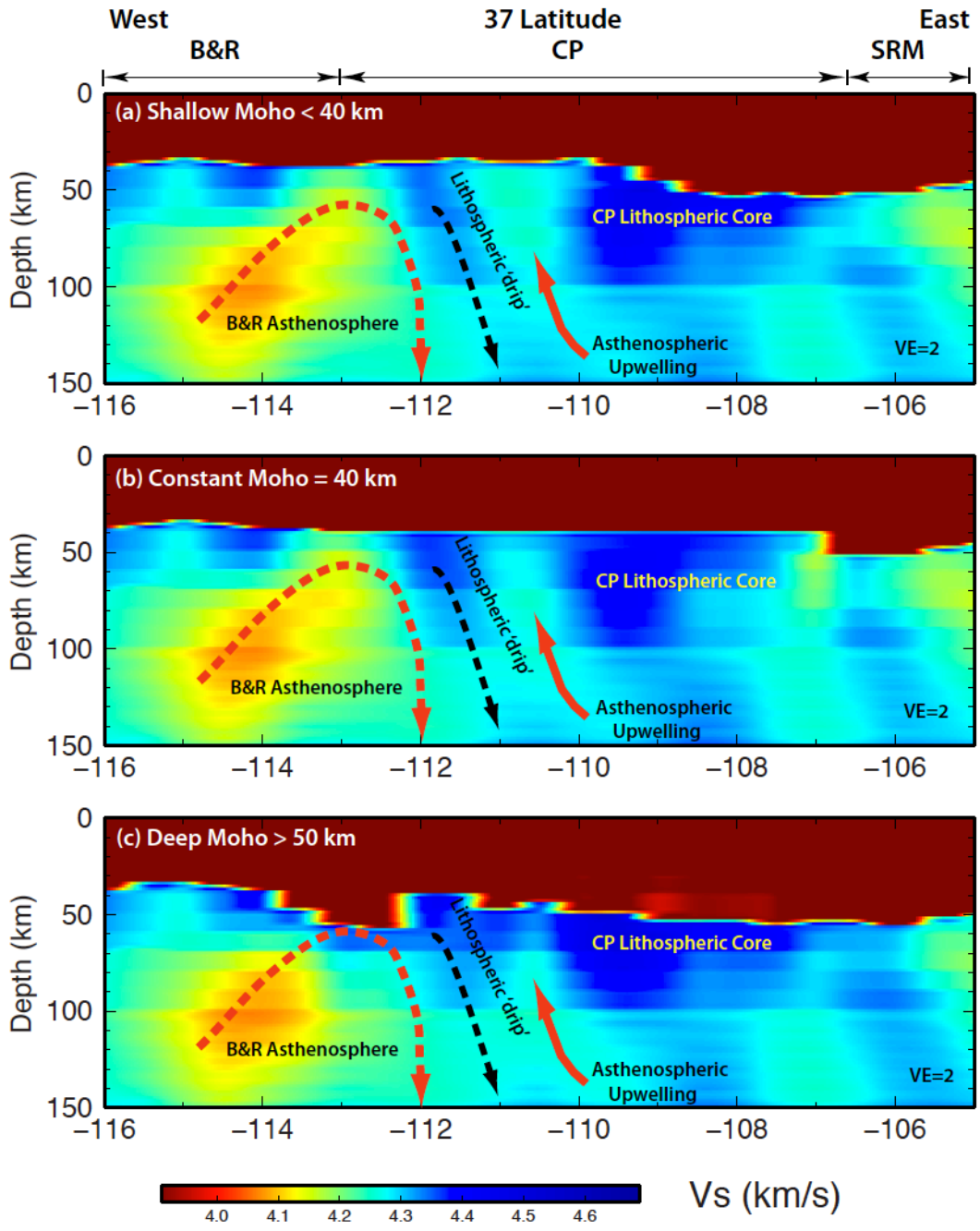

Figure 3.12 Three Vs cross-sections along 37°N latitude from different inversion tests with constraints of crustal thickness beneath the delamination region: (a) shallow Moho (<40 km); (b) constant Moho (40 km); (c) deep Moho (>50 km). The black dashed arrows show the convective downwelling drip of the lower crust and mantle lithosphere, which cause the asthenosphere to upwell to shallow depths (solid red arrow on the right). The dashed red arrows indicate the small-scale convective erosion at the edges. Vertical exaggeration (VE) is 2 for all the panels.

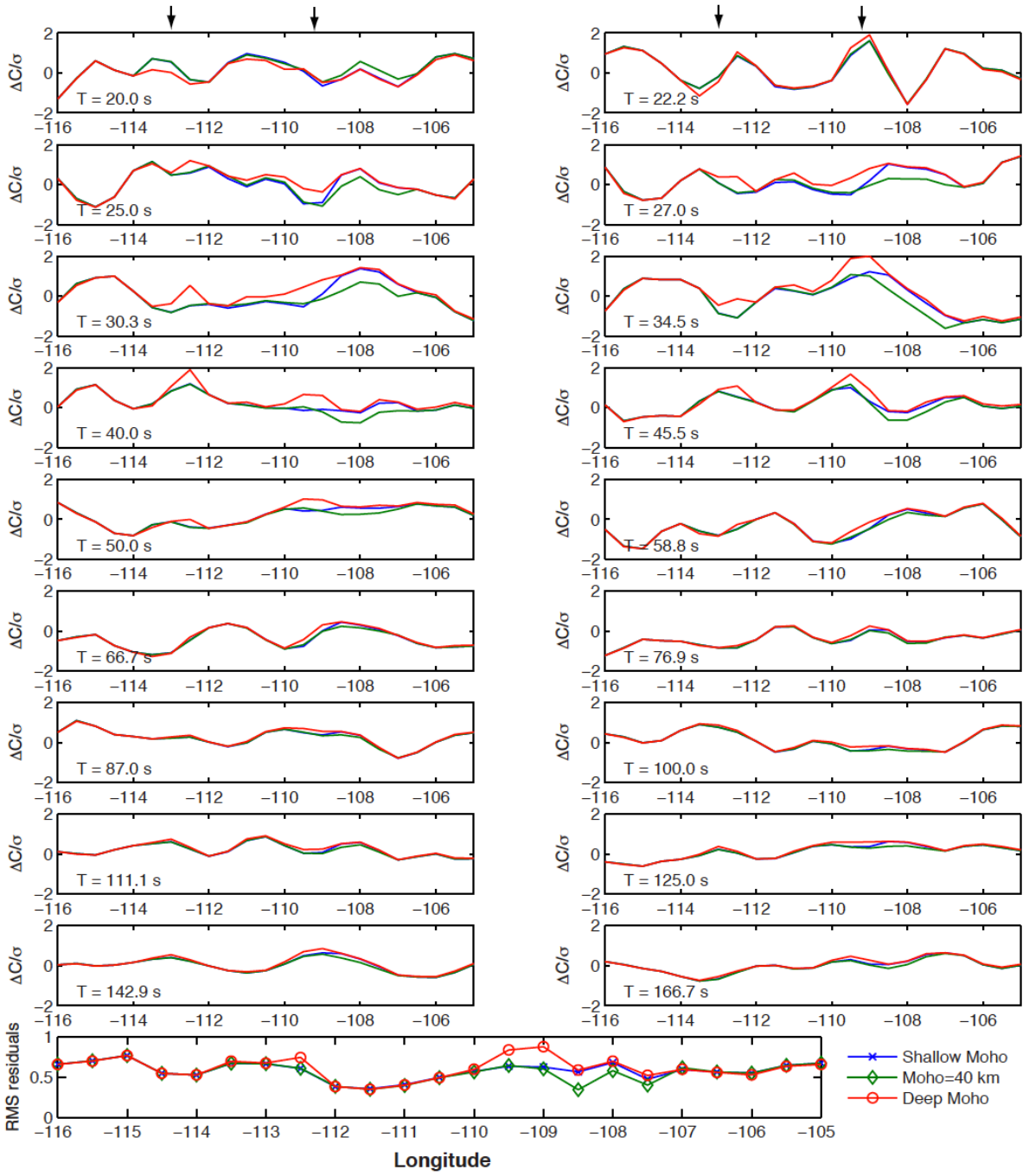

Figure 3.13 Vs inversion residuals along 37°N in the three inversion tests as mentioned in Figure 3.12. The top 18 plots are the relative residuals (different between the predicted and observed phase velocity divided by its standard deviation at that period), while the bottom panel is the RMS residuals for all the 18 periods.

3.6 Summary

We have developed a 3-D Vs model to ~250 km depth using USArray-based Rayleigh wave phase velocity data determined with finite-frequency Rayleigh wave kernels and the two-plane wave method to separate multi-pathed arrivals. The resulting Vs model reveals strong lateral heterogeneity in the crust and uppermost mantle beneath the CP and the adjacent tectonic provinces. The Proterozoic CP lithosphere has high velocities relative to its peripheries and these high velocities extend to the north into the Rockies. A ring of low velocities in the upper mantle surround and extend under the CP periphery about ~100 in the CP-BRP transition region and the RGR/JL boundary. We interpret these low velocities as partially molten lithosphere or asthenosphere based on the geochemical signatures of volcanics in the region during the past 5-6 Myr. We suggest that the rehydrated and mechanically weakened CP lithosphere is progressively removed from the edges where low-velocity zones and thinned lithosphere are present, taking the form of either 2-D thermal or 3-D thermo-chemical convective erosion driven from the plateau edges by the thermal gradient and lithospheric thickness steps, and likely aided by asthenospheric melt invasion of the lithosphere. This edge convective process, in 3-D and the complexity of the modern crustal and upper mantle structures under the plateau are understandable in terms of the lithospheric modification during the Cenozoic. By putting additional constraints from our Rayleigh wave Vs model with the Ps RFs analysis, we have obtained a new LAB topography map. Our Vs model suggests that the lithosphere is removed at a rate similar to the magmatic encroachment towards the center of the plateau observed in surface volcanism. We note that the surface wave tomography provides additional seismic tomographic evidence for the delamination-style convective downwelling hypothesis in the western CP based on the RF

imaging [*Levander et al*., 2011]. A northeasterly dipping high-velocity anomaly, appearing regardless of the crustal thickness used in inversion, is interpreted as the convective downwelling of lower crust and mantle lithosphere at the western margin of the plateau. Based on previous studies and our new Vs model, we propose a hybrid uplift mechanism that includes a combination of chemical/thermal/geodynamic contributions, with buoyant support under the margins provided from lithospheric removal.

Chapter 4 3-D GENERALIZED RADON TRANSFORM IMAGING USING KIRCHHOFF APPROXIMATION AND TELESEISMIC P-TO-S SCATTERED WAVES

Teleseismic imaging techniques utilizing mode converted scattered waves are gaining importance due to the deployment of increasingly dense broadband seismograph arrays. Although CCP stacking is widely used to determine structure from Ps or Sp scattered wavefields isolated by RF processing, this method is limited due to its assumption of a layered medium: Dipping events and diffractions are not treated correctly. As an extension of previous 2-D Generalized Radon Transform (GRT) imaging methods [e.g., *Bostock*, 2002], we present a 3-D Kirchhoff-approximate imaging technique to migrate scattered waves in 3-D. We first derive the 3-D migration formula for P-to-S conversions using the GRT solution to the linear inverse elastic wave scattering problem. Then we illustrate the Kirchhoff-GRT method using finite-difference synthetic seismograms from several 3-D models.

Next, we applied the method to two Flexible Array datasets in the western United States to image the MTJ and the HLP crust and uppermost mantle structures. From the HLP data, we have constructed the Ps transmission coefficient images with three-component (S_V, S_H and P) Green's functions (GFs). The 1.0 and 0.5 Hz images show a continuous undulating Moho, as well as three negative upper mantle events at 50-80 km depth. Compared to the CCP images [*Eagar et al.*, 2011], the Moho is more clearly imaged, particularly near 117°W at the western edge of the Owyhee Plateau. The three negative events in the upper mantle correlate well with the top of three low-Vs zones (-3% contour) in the Rayleigh wave tomography model [*Wagner et al.*, 2010]. The migrated Ps RF data from MTJ clearly image the rapid

decrease in LAB depth from ~65 km beneath the subducting Gorda Plate to 30-50 km beneath the Coast Ranges slab window. The final image is consistent with, but has higher resolution than joint receiver-function/Rayleigh wave inversion Vs structure [*Liu et al*., 2012] and Ps CCP stacks [*Zhai*, 2010]. Scattered waves on the P and SH components produced images comparable to that from the S_V component. Although restricted by array aperture and spatial aliasing criteria to dense, large aperture arrays, the 3-D Kirchhoff-GRT technique provides a promising tool for imaging complicated lithospheric structures that are poorly mapped or unresolved by more traditional imaging methods.

4.1 Introduction

Scattered teleseismic body waves generated by receiver side structure are widely used to determine fine-scale seismic structure in the lithosphere and upper mantle [*Bostock*, 2007; *Rondenay*, 2009; *Nowack et al*., 2010]. The widespread deployment of broadband seismometers, such as the USArray TA and a large number of dense portable array experiments (FAME, La RISTRA, HLP etc.), motivates improvement of multichannel data processing and seismic imaging techniques (migration/inversion) in global seismology to produce more highly detailed images. Teleseismic converted phases (e.g., P-to-S mode) from receiver-side structure provide an important higher resolution complement to teleseismic traveltime tomography for imaging the upper mantle. The most commonly used multi-component data analysis method is the RF technique [e.g., *Langston*, 1979; *Vinnik*, 1977; *Kumar et al.*, 2005], which attempts to deconvolve the source function from the converted wave field and can be used to measure discontinuity depths by time to depth conversion and impedance contrasts by reference to a known or assumed event. 2-D and 3-D images from RFs can be constructed using the CCP stacking method [e.g., *Dueker and Sheehan*, 1997].

However, CCP stacking normally assumes horizontal converting horizons and determines energy relocation in depth along 1-D ray paths. Being relatively simple and computationally inexpensive, this approach (though fast) dramatically decreases the ability to detect steeply dipping or localized anomalous structures.

In the past decade, both pre- and post-stack migration-type methods have been developed for upper mantle imaging [e.g., *Pavlis*, 2005]. These include acoustic Kirchhoff integral/migration [*Ryberg and Weber*, 2000; *Levander et al*., 2005, 2006; *Wilson and Aster*, 2005] and inverse scattering techniques via the GRT inversion with either the Born [*Bostock and Rondenay*, 1999; *Bostock et al.,* 2001, 2002; *Poppeliers and Pavlis*, 2003ab; *Pavlis*, 2011] or the Kirchhoff approximation [*Bostock*, 2002]. Migration of RFs or GFs in these methods maps the location of conversion to the true position, and thus significantly reduces the artifacts caused by dipping or strongly curved discontinuity interfaces in the CCP images [*Rondenay*, 2009]. However, previous efforts mainly focus on either scalar waves using the Ps RF as the representation of the scattered field, or are limited to 2-D. Here we present a 3-D elastic Generalized Radon Transform method based on the Kirchhoff scattering approximation, developed from *Bostock*'s 2-D approach [2002], to recover transmission coefficients of discontinuities.

The 3-D elastic Kirchhoff-GRT technique for teleseismic imaging originates in the asymptotic solutions to inverse scattering problems via GRT inversion developed in reflection seismology [e.g., *Beylkin*, 1985; *Bleistein*, 1987; *Miller et al*., 1987]. This method has much in common with depth migration algorithms, which are used to reconstruct

structural images, but do not suffer from the loss of true amplitude information, and hence have the ability to determine material properties contrasts. *Beylkin and Burridge* [1990] extended the application of the GRT solution to linearized inverse scattering problems [e.g., *Beylkin*, 1985; *Miller et al*., 1987] from the Born approximation (single- scattering from a volume) to the Kirchhoff approximation (single scattering from a smooth interface), and have outlined P-to-P elastic scattering with the Kirchhoff approximation using the concept of singular functions [*Bleistein*, 1987]. *Docherty* [1991] further compared the Kirchhoff migration and inversion formulae in acoustic cases, and concluded that they are identical with certain filters and imaging conditions under common-source geometry.

In the teleseismic situation, acquisition geometry and the uncontrolled source distribution make the forward P-to-S conversion more practically useful than single P-to-P scattering. GRT solutions similar to that of *Beylkin and Burridge* [1990] have been developed in 2-D for elastic waves by *Bostock et al.* [*Bostock et al*., 2001; *Bostock*, 2002]. Similar to 3-D GRT imaging, *Poppeliers and Pavlis* [2003ab] developed a prestack plane wave migration of RFs, with the recent application of this method to the transition zone discontinuities using the USArray RFs [*Pavlis*, 2011]. Full 3-D linearized scattered waveform inversion is attempted in tomographic form by *Frederiksen and Revenaugh* [2004] using ray theory and Rayleigh scattering, but is computationally expensive.

In this chapter, we extended Bostock's 2-D approach to 3-D, using the Kirchhoff-Helmholtz integral and GRT formulation. Kirchhoff-GRT imaging is a useful alternative to the Born-approximate imaging in certain circumstances. Although using the same backprojection

operator, the forward modeling of both approximations is based on different assumptions [e.g., *Beydoun and Jin*, 1994]. In order to linearize the Lippman-Schwinger integral, the Born approximation (volumetric integral) assumes small perturbations of material parameters with respect to a background model, while the Kirchhoff approximation (surface integral) solves for both small and large impendence contrasts across discontinuities in elastic properties (e.g., the Moho, the 410- and the 660-km) with smooth amplitude fluctuations. The Kirchhoff-approximate surface integral better describes typical stratification of near-receiver structures, while the Born representation of small perturbations might be more useful to resolve volume perturbations, such as in a mantle wedge. Instead of directly imaging the media property perturbations, Kirchhoff-GRT inverts for the reflection/transmission (R/T) coefficients that depend on the scattering angles and impedance contrast.

In this study, we start with the derivation of the 3-D elastic wave Kirchhoff-GRT formula for teleseismic geometry. After testing the method on synthetic datasets, we apply it to field data examples from two regional studies in the WUS: the FAME (2007-2009) and HLP (2006-2009) experiments. The Kirchhoff-GRT method images features consistent with previous studies, but arguably produces higher-resolution images and identification of more structures.

4.2 Derivation of 3-D Kirchhoff GRT inversion

The Kirchhoff approximation and the Kirchhoff-Helmholtz integral have been used previously in elastic wave inverse scattering [*Morse and Feshbach*, 1953; *Miller et al*., 1987; *Beylkin and Burridge*, 1990; *Bleistein et al.*, 2000; *Bostock*, 2002]. Following *Bostock* [2002] we describe the derivation of the forward model starting from the fundamental equation of motion in an isotropic medium, adopting a high-frequency asymptotic form of the GF, and

then introduce the GRT inversion to estimate the R/T coefficients at any imaging point. We separate the final images into three in a natural way using three-component input data.

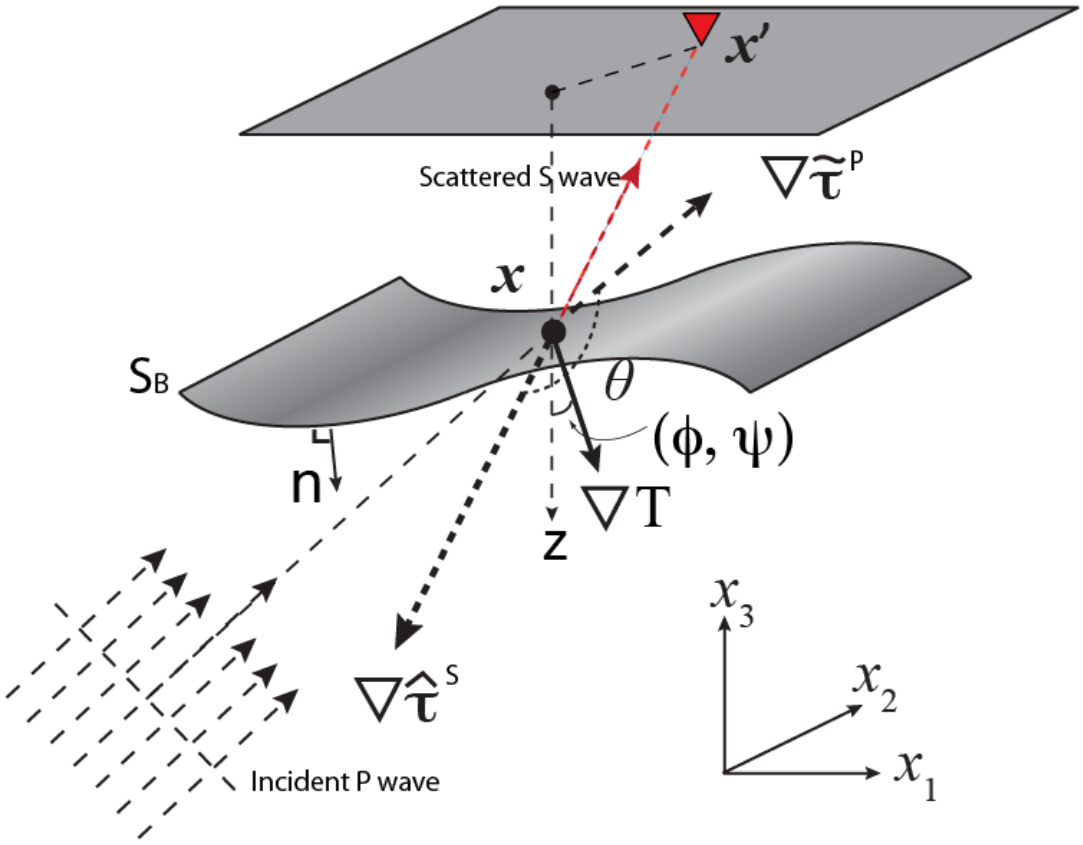

Figure 4.1 3-D geometry for the inverse scattering theory using the Kirchhoff approximation modified from the 2-D scheme in *Bostock* [2002]. The red inverse triangle denotes the surface receiver at **x'**. The incident P wave is converted to the S wave (red dashed line) after transmission across the discontinuity interface S_B with a normal vector **n**. At the imaging point **x**, the traveltime gradients ($\nabla\tilde{\tau}^P$ and $\nabla\tilde{\tau}^S$) of incident P and back-propagated S waves form the scattering angle θ. The compound traveltime gradient ∇T is characterized by two geometrical angles ϕ and ψ with respect to the vertical direction (**z**).

4.2.1 3-D Kirchhoff-Helmholtz integral representation

We use forward P-to-S conversion as an example of teleseismic scattered waves we wish to invert for transmission coefficients (i.e. impedance contrasts) using GRT inversion. Consider an incident P wavefield, $\mathbf{U}(\mathbf{x})$, from a teleseismic event propagating across an arbitrarily shaped discontinuity S_B (Figure 4.1). After forward P-to-S transmission, the scattered S

waves arrive at the surface receivers time delayed relative to the direct P wave. Starting from the Fourier transformed equation of motion in a general 3-D elastic medium in absence of source:

$$\rho(\mathbf{x})\omega^2 U_i(\mathbf{x}) + (c_{ijkl}(\mathbf{x})U_{k,l}(\mathbf{x}))_{,j} = 0 \tag{4.1}$$

where $\{\rho(\mathbf{x}),\ c_{ijkl}(\mathbf{x})\}$ are the density and elastic tensor elements, both of which depend on the position of measurement $\mathbf{x}$, and w is the angular frequency. $U_i(\mathbf{x})$ is the i-th component of displacement after the interaction of the upgoing wavefields with the discontinuity at any given frequency ω. Commas imply spatial derivatives. Assuming an isotropic medium, the elastic tensor is reduced to the two Lame parameters:

$$c_{ijkl} = \lambda\delta_{ij}\delta_{kl} + \mu(\delta_{ik}\delta_{jl} + \delta_{il}\delta_{jk}) \tag{4.2}$$

and the equation of motion is

$$\rho\omega^2 U_i + (\lambda U_{j,j})_{,i} + [\mu(U_{i,j} + U_{j,i})]_{,j} = 0 \tag{4.3}$$

Introducing the corresponding GF in the upper medium after scattering interaction with the interface, where the GF is the solution to the wave equation for back-propagating from the surface receiver, we have:

$$\rho\omega^2 G_{in} + (\lambda G_{jn,j})_{,i} + [\mu(G_{in,j} + G_{jn,i})]_{,j} = -\delta_{in}\delta(\mathbf{x} - \mathbf{x}') \tag{4.4}$$

in which the GF G_{in} stands for the i-th component of the displacement response at $\mathbf{x}$ due to a unit impulse applied at $\mathbf{x}'$ in the n-direction. Note that both λ and μ are functions of $\mathbf{x}$. Integrating both sides of $(4.3)\times G_{in} - (4.4)\times U_i$ through a closed volume V, employing the divergence theorem:

$$\iiint_V (\nabla\cdot\mathbf{F})\mathrm{d}V = \oint_S (\mathbf{n}\cdot\mathbf{F})\mathrm{d}S \quad \text{or} \quad \iiint_V \mathbf{F}_{i,i}\mathrm{d}V = \oint_S \mathbf{n}_i\mathbf{F}_i\mathrm{d}S$$

and subtracting the zero term as mentioned in *Bostock* [2002] and *Pao and Varatharajulu* [1976]

$$\oint_S \mathrm{d}S\mathbf{n}\cdot[\nabla\times(\mathbf{U}\times\mathbf{G}_n)] = \iiint_V \mathrm{d}V\nabla\cdot[\nabla\times(\mathbf{U}\times\mathbf{G}_n)] = 0$$

we get an expression for the scattered wavefield at the receiver:

$$\begin{aligned} U_n(\mathbf{x}') = \oint_S \mathrm{d}S(\lambda+2\mu)[(\mathbf{n}\cdot\mathbf{G}_n)(\nabla\cdot\mathbf{U}) - (\mathbf{n}\cdot\mathbf{U})(\nabla\cdot\mathbf{G}_n)] \\ +\mu[(\mathbf{n}\times\mathbf{G}_n)\cdot(\nabla\times\mathbf{U}) - (\mathbf{n}\times\mathbf{U})\cdot(\nabla\times\mathbf{G}_n)] \end{aligned} \tag{4.5}$$

This formula is similar to those derived in *Bostock* [2002] for 2-D, and *Morse and Feshbach* [1953] for 3-D. The isolation of curl-free and divergence-free terms in the integral separates the P and S wave modes. For example, we can remove the curl-free terms in the displacement when using P-to-S conversion energy to image upper mantle structures. By virtue of the Sommerfeld radiation condition, the integral vanishes on the infinite radius for the upper surface. Thus, we obtain the displacement of transmitted S waves from an incident P event at the receivers as

$$U_n(\mathbf{x}') = \iint_{S_B} \mathrm{d}S\mu[(\mathbf{n}\times\mathbf{G}_n)\cdot(\nabla\times\mathbf{U}) - (\mathbf{n}\times\mathbf{U})\cdot(\nabla\times\mathbf{G}_n)] \tag{4.6}$$

4.2.2 High-frequency approximation and GRT inversion

We adopt the same notations for the quantities associated with the incident ('~'), scattered ('ˇ') and back-propagated ('^') waves as those used in *Beylkin and Burridge* [1990] and *Bostock* [2002]. To further quantify the scattered and backscattered waves, and apply the Kirchhoff approximation on the boundary, we use high-frequency asymptotic forms to estimate the S wave GFs ($\hat{\mathbf{g}}^{S_V}$,$\hat{\mathbf{g}}^{S_H}$ are the unit polarization vectors of S_V and S_H, respectively):

$$G_{in}(\mathbf{x},\mathbf{x}') = \hat{A}^S(\mathbf{x},\mathbf{x}')e^{i\omega\hat{\tau}^S(\mathbf{x},\mathbf{x}')}[\hat{g}_i^{S_V}(\mathbf{x})\hat{g}_n^{S_V}(\mathbf{x}') + \hat{g}_i^{S_H}(\mathbf{x})\hat{g}_n^{S_H}(\mathbf{x}')] \tag{4.7}$$

Similarly, for incident P and scattered S wavefields we have:

$$U_i^0(\mathbf{x}) = \tilde{A}^P(\mathbf{x})e^{i\omega\tilde{\tau}^P(\mathbf{x})}\tilde{g}_i^P(\mathbf{x}) \tag{4.8}$$

$$U_i(\mathbf{x}) = \breve{A}^S(\mathbf{x})e^{i\omega\breve{\tau}^S(\mathbf{x})}\breve{g}_i^S(\mathbf{x}) \tag{4.9}$$

We now substitute Eqs. (4.7-4.9) into (4.6), and note that $\nabla\tau >> \nabla A, \nabla\breve{\mathbf{g}}^S$, $\hat{\mathbf{g}} = -\breve{\mathbf{g}}$, $\nabla\tau = |\nabla\tau|\mathbf{g}^P$. The substitution of the S-wave GF and scattered waves into the Kirchhoff-Helmholtz integral equation give the first term in S_V:

$$\begin{aligned}(\mathbf{n}\times\mathbf{G}_n)\cdot(\nabla\times\mathbf{U}) &= (\mathbf{n}\times\hat{A}^S e^{i\omega\hat{\tau}^S}\hat{\mathbf{g}}^{S_V}\hat{g}_n^{S_V}(\mathbf{x}'))\cdot(\nabla\times\breve{A}^S e^{i\omega\breve{\tau}^S}\breve{\mathbf{g}}^S) \\ &= i\omega\hat{A}^S\breve{A}^S e^{i\omega(\hat{\tau}^S+\breve{\tau}^S)}[(\mathbf{n}\times\hat{\mathbf{g}}^{S_V})\cdot(\nabla\breve{\tau}^S\times\breve{\mathbf{g}}^S)]\hat{g}_n^{S_V}(\mathbf{x}') \\ &= i\omega\hat{A}^S\breve{A}^S e^{i\omega(\hat{\tau}^S+\breve{\tau}^S)}\{\mathbf{n}\cdot[\hat{\mathbf{g}}^{S_V}\times(\nabla\breve{\tau}^S\times\breve{\mathbf{g}}^S)\}\hat{g}_n^{S_V}(\mathbf{x}')\end{aligned}$$

Thus we have a description for the S-wave after scattering as:

$$\begin{aligned}U(\mathbf{x}') = i\omega\int_{S_B} \mathrm{d}S\rho\beta^2\hat{A}^S C\tilde{A}^S e^{i\omega(\hat{\tau}^S+\tilde{\tau}^S)}\{&\mathbf{n}\cdot[\hat{\mathbf{g}}^{S_V}\times(\nabla\tau^S\times\breve{\mathbf{g}}^S) - \breve{\mathbf{g}}^S\times(\nabla\hat{\tau}^S\times\hat{\mathbf{g}}^{S_V})]\hat{g}_n^{S_V}(\mathbf{x}') \\ &+\mathbf{n}\cdot[\hat{\mathbf{g}}^{S_H}\times(\nabla\tau^S\times\breve{\mathbf{g}}^S) - \breve{\mathbf{g}}^S\times(\nabla\hat{\tau}^S\times\hat{\mathbf{g}}^{S_H})]\hat{g}_n^{S_H}(\mathbf{x}')\end{aligned} \tag{4.10}$$

In this case C is the forward P-to-S transmission coefficient as defined by Eq. (5.40) in *Aki and Richards* [2002].

The vector **n** in the S wavefield formulae remains unknown and can be estimated using the micro-localization technique [*Beylkin and Burridge*, 1990] and applying Snell's law at the local normal to the boundary (Figure 4.1):

$$\mathbf{n} = \frac{\nabla\hat{\tau}^S + \nabla\tilde{\tau}^P}{|\nabla\hat{\tau}^S + \nabla\tilde{\tau}^P|} \tag{4.11}$$

Instead of using seven scattering modes for the 2-D medium derived by *Bostock* [2002], we focus on the P-to-S conversion mode. We define the corresponding compound amplitude (in vector form) and traveltime for this scattering mode as:

$$\vec{A} = 2\rho\hat{c}^2\tilde{A}\hat{A}\frac{\nabla T\cdot\nabla\hat{\tau}^S}{|\nabla T|}\vec{\ell}(\mathbf{x},\mathbf{x}') \tag{4.12}$$

$$T = \hat{\tau}^S + \tilde{\tau}^P \tag{4.13}$$

in which we include the polarization vector in the amplitude defined as:

$$\vec{\ell}(\mathbf{x},\mathbf{x}') = -\frac{\left(\hat{\mathbf{g}}^{S_H}(\mathbf{x})\cdot\tilde{\mathbf{n}}^P\right)\hat{\mathbf{g}}^{S_H}(\mathbf{x}')+\left(\hat{\mathbf{g}}^{S_V}(\mathbf{x})\cdot\tilde{\mathbf{n}}^P\right)\hat{\mathbf{g}}^{S_V}(\mathbf{x}')}{\sin\theta} \tag{4.14}$$

and the scattering angle θ (Figure 4.1) between the incident P and back-propagated waves defined as:

$$\theta = \arccos(\tilde{\mathbf{n}}^P\cdot\hat{\mathbf{n}}^S) \tag{4.15}$$

This is a function of incident/scattered wave velocities and gradients of traveltimes, and is required to estimate the compound amplitude. However, in practice, we replace the exact velocities with values from the smoothly varying migration velocity model, since we do not know the exact velocities above and below the interface.

Note that the unit vectors for the S_V and S_H components at the scatterer and receiver differ from the 2-D or 2.5 D case presented in *Bostock* [2002]. Substituting Eqs. (4.11-4.14) into (4.10), we have a compact form for the scattering wavefield:

$$\mathbf{U}(\mathbf{x}') = i\omega\int_{S_B} \mathrm{d}S C(\mathbf{x},\theta)\vec{A}e^{i\omega T} \tag{4.16}$$

Introducing the singular function $\gamma(s)$ and recasting the surface integrals as volume integrals, we obtain:

$$\mathbf{U}(\mathbf{x}') = i\omega \int_V \mathrm{d}V \gamma(s) C(\mathbf{x},\theta) \vec{A} e^{i\omega T} \tag{4.17}$$

Then we apply a filter $F(\omega) = i\omega$ (a high-frequency filter in contrast to the Born approximation, and simpler in 3-D than the corresponding 2-D filter $-\sqrt{-i\omega i}\,\mathrm{sgn}(\omega)$) and inverse Fourier transform $\mathbf{U}(\mathbf{x}')$ to the time domain to give

$$\begin{aligned} \vec{v}(\mathbf{x}',t) &= \mathbf{F}^{-1}\{i\omega \mathbf{U}(\mathbf{x}')\} \\ &= \frac{1}{2\pi} \int \mathrm{d}\omega e^{-i\omega t} \times (i\omega)^2 \int_V \mathrm{d}V \gamma(s) C(\mathbf{x},\theta) \vec{A} e^{i\omega T} \\ &= \int_V \mathrm{d}V \gamma(s) C(\mathbf{x},\theta) \vec{A} \delta''(t-T) \end{aligned} \tag{4.18}$$

Recognize that this equation can be viewed as an inverse Radon transform. The 3-D Radon transform [*Miller et al*. 1987] is

$$Rf(\vec{\xi}, p) = \int \mathrm{d}^3 x f(\vec{x}) \delta(p - \vec{\xi} \cdot \vec{x}) \tag{4.19}$$

and its inverse is:

$$f(\vec{x}_0) = -\frac{1}{8\pi^2} \int \mathrm{d}^2 \xi \int \mathrm{d}^3 x f(\vec{x}) \delta''\left[\vec{\xi} \cdot (\vec{x}_0 - \vec{x})\right] \tag{4.20}$$

In the vicinity of a scattered point $\mathbf{x}_0$, keeping only the first order terms of the traveltime gradient, we have

$$\begin{aligned} \vec{v}(\mathbf{x}', t = T_0) &= \int_V \mathrm{d}V \gamma(s) C(\mathbf{x},\theta) \vec{A} \delta''(T_0 + |\nabla T_0| \vec{n} \cdot (\vec{x} - \vec{x}_0) + \ldots - T_0) \\ &\approx \int_V \mathrm{d}V \gamma(s) C(\mathbf{x},\theta) \vec{A} \delta''(|\nabla T_0| \vec{n} \cdot (\vec{x} - \vec{x}_0)) \\ &= \frac{\vec{A}}{|\nabla T_0|^3} \int_V \mathrm{d}V \gamma(s) C(\mathbf{x},\theta) \delta''(\vec{n} \cdot (\vec{x} - \vec{x}_0)) \end{aligned} \tag{4.21}$$

Taking the inner product of $\vec{A}(\mathbf{x}_0, \mathbf{x}')$ with both sides gives

$$\int_V \mathrm{d}V \gamma(s) C(\mathbf{x},\theta) \delta''(\vec{n} \cdot (\vec{x} - \vec{x}_0)) = \frac{|\nabla T_0|^3}{\| A \|^2} \vec{A}(\mathbf{x}_0, \mathbf{x}') \cdot \vec{v}(\mathbf{x}', t = T_0) \tag{4.22}$$

in which

$$|| A ||^2 = \sum_n A_n^2(\mathbf{x}_0, \mathbf{x}') \tag{4.23}$$

Thus from analogy with the 3-D Radon transform, we finally obtain the R/T coefficients as

$$\overline{\gamma(s)C(\mathbf{x},\theta)} = -\frac{1}{8\pi^2}\int \mathrm{d}^2\psi \frac{|\nabla T|^3}{|| A^2 ||}\vec{A}(\mathbf{x}_0,\mathbf{x}')\cdot\vec{v}\left(\mathbf{x}', t = T(\mathbf{x}_0,\mathbf{x}')\right) \tag{4.24}$$

As suggested by *Miller et al.* [1987], it is more efficient to calculate the R/T coefficients in Eq. (24) using numerical computation of the Jacobian $\mathrm{d}^2\psi$ term instead of deriving an explicit 3-D expression for it. The R/T coefficients can also be evaluated from different contributions by the three components of the wavefield. If we transform the recorded wavefield from Z-N-E to the P-S_V-S_H system and separate the upgoing wavefield from the downgoing reflection from the free surface [e.g. *Kennett*, 1991; *Bostock and Rondenay*, 1999; *Reading et al*., 2003; *Rondenay*, 2009] using the free-surface transformation:

$$\begin{pmatrix} u^P \\ u^{S_V} \\ u^{S_H} \end{pmatrix} = \begin{pmatrix} \dfrac{\beta^2 p^2 - 1/2}{\sqrt{1-\alpha^2 p^2}} & \dfrac{p\beta^2}{\alpha} & 0 \\ p\beta & \dfrac{1/2 - \beta^2 p^2}{\sqrt{1-\beta^2 p^2}} & 0 \\ 0 & 0 & 1/2 \end{pmatrix} \begin{pmatrix} u^Z \\ u^R \\ u^T \end{pmatrix}$$

we can further consider the final transmission coefficients as a sum of three partial contributions from scattered waves in the S_V, S_H and P direction, respectively:

$$\overline{\gamma(s)C(\mathbf{x},\theta)} = \left\langle \gamma(s)C \right\rangle_{S_V} + \left\langle \gamma(s)C \right\rangle_{P} + \left\langle \gamma(s)C \right\rangle_{S_H} \tag{4.25}$$

In both synthetic and field data examples, we will examine the contribution from each component as well as the total.

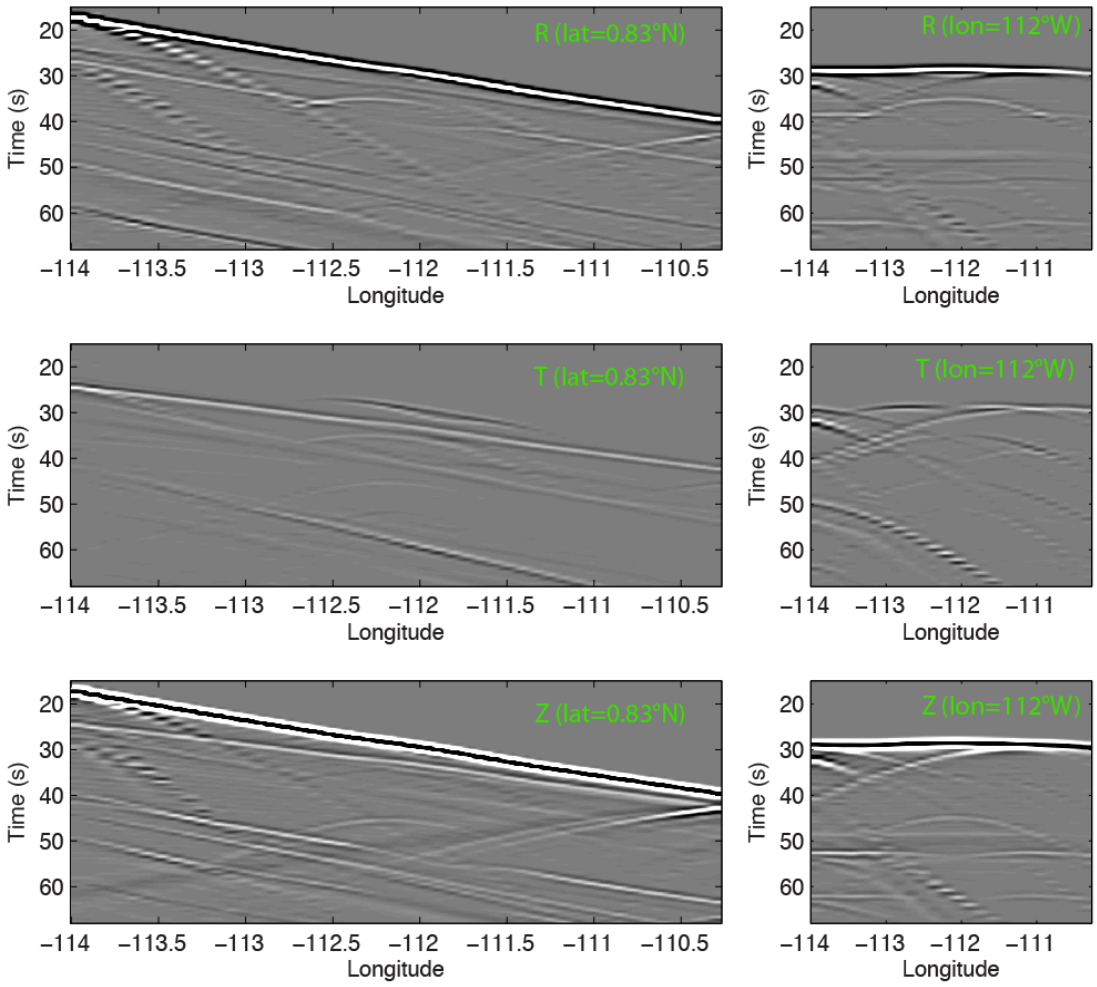

Figure 4.2 Profiles of the R-T-Z components through the synthetic data volume along latitude 0.83°N (left) and cross-lines along longitude 112°W (right) for the 'dome' model shown in Fig. 4.4(a).

4.3 Synthetic tests

4.3.1 3-D elastic finite-difference simulation

We test the 3-D Kirchhoff-GRT technique on several synthetic models calculated using a 3-D elastic wave, finite-difference wave propagation code [*Larsen and Harris*, 1993]. This synthetic method solves the elastic wave equation in the imaging volume on a staggered grid with 4th-order accuracy in space and 2nd-order accuracy in time [e.g., *Madariaga*, 1976; *Levander*, 1988; *Larsen and Harris*, 1993], using the absorbing boundary conditions on all

sides except the free surface. We simulate a teleseismic incident P wave with a plane of point sources distributed at the bottom of the model. Traveltime delays and amplitude corrections were pre-computed from the assumed earthquake location using a 1-D global model. We used a Ricker wavelet with a central frequency of 0.5 Hz as the source time function for all these simulations. The grid spacing was 0.6 km and the time interval 0.029 seconds.

We saved 3-component seismograms at the free surface at 1128 regularly spaced recording points (9 km×9 km) in a 4°×2° area for a teleseismic event (epicentral distance: 75°, back azimuth: 270°). In order to construct several 3-D discontinuity interfaces to test our Kirchhoff-GRT code and examine its potential resolution limitations, we introduce 3-D heterogeneities into a smooth background model modified from the IASP91 model [*Kennett and Engdahl*, 1991]. The recorded elastic wavefields are transformed from the orthogonal Z-N-E or R-T-Z components (Figure 4.2) to the P-S_V-S_H system, which not only rotates the wavefields to the polarization direction of P, S_V and S_H, but also extracts the upgoing waves from the free-surface reflections since the Kirchhoff-GRT forward model builds on the displacement representation of the upgoing waves. We use both the velocity seismograms and the GFs estimated by the RF technique, taking P or vertical components (Z) as source time function approximations for each teleseismic event.

4.3.2 Synthetic test: models and results

4.3.2.1 Crater and dome

We constructed two 3-D models (Figure 4.3 and 4.4) with crater- and dome-shaped discontinuities above which we place constant model properties (V_P=5.8 km/s, V_S=3.36

km/s, density=2.72 g/cm^3 at the surface of the reference model). The depth of the surface is 72km, with the crater/dome having an amplitude of ±15 km and a diameter of 88.8 km. The center of both models is located 75° from the epicenter. Figure 4.3 and 4.4 show the input P velocity model (a), the synthetic seismograms (b-c), as well as the imaged transmission coefficient structure from our Kirchhoff-GRT method (d-i), which recover both discontinuities well. The depths and the 3-D shapes of these two images are quite consistent with the models (dashed white lines in Figures 4.3d, f, h and 4.4d, f, h), although the imaged depth of the discontinuity is a little deeper (~3 km). This we attribute to the difference between the model used to calculate the imaging traveltime and amplitude tables (constant gradient) and the true model used to compute synthetics (constant velocities above interface). By rescaling the constant velocity by the migration velocity at given depth, we can map the discontinuity interface (~75 km) to the true location (~72 km).

4.3.2.2 Sinuous interface

Both 2/2.5-D Born and Kirchhoff GRT theory for teleseismic imaging [*Bostock et al*., 2001; *Bostock*, 2002] correct out-of-plane energy to in-plane propagation with a ray parameter dependent phase shift, assuming that out of plane structural heterogeneity is absent. To examine imaging of an exact 2-D structure, we set up a 3-D model consisting of a north-south striking sinusoidal discontinuity, 60 km deep, with a 12 km peak to peak amplitude (Figure 4.5). Above the discontinuity the model has low, constant velocities and density. Our Kirchhoff-GRT images show exactly the same sinuous shape as the discontinuity surface, again with a 3-km depth shift caused by the inaccurate migration velocity model (Figure 4.5).

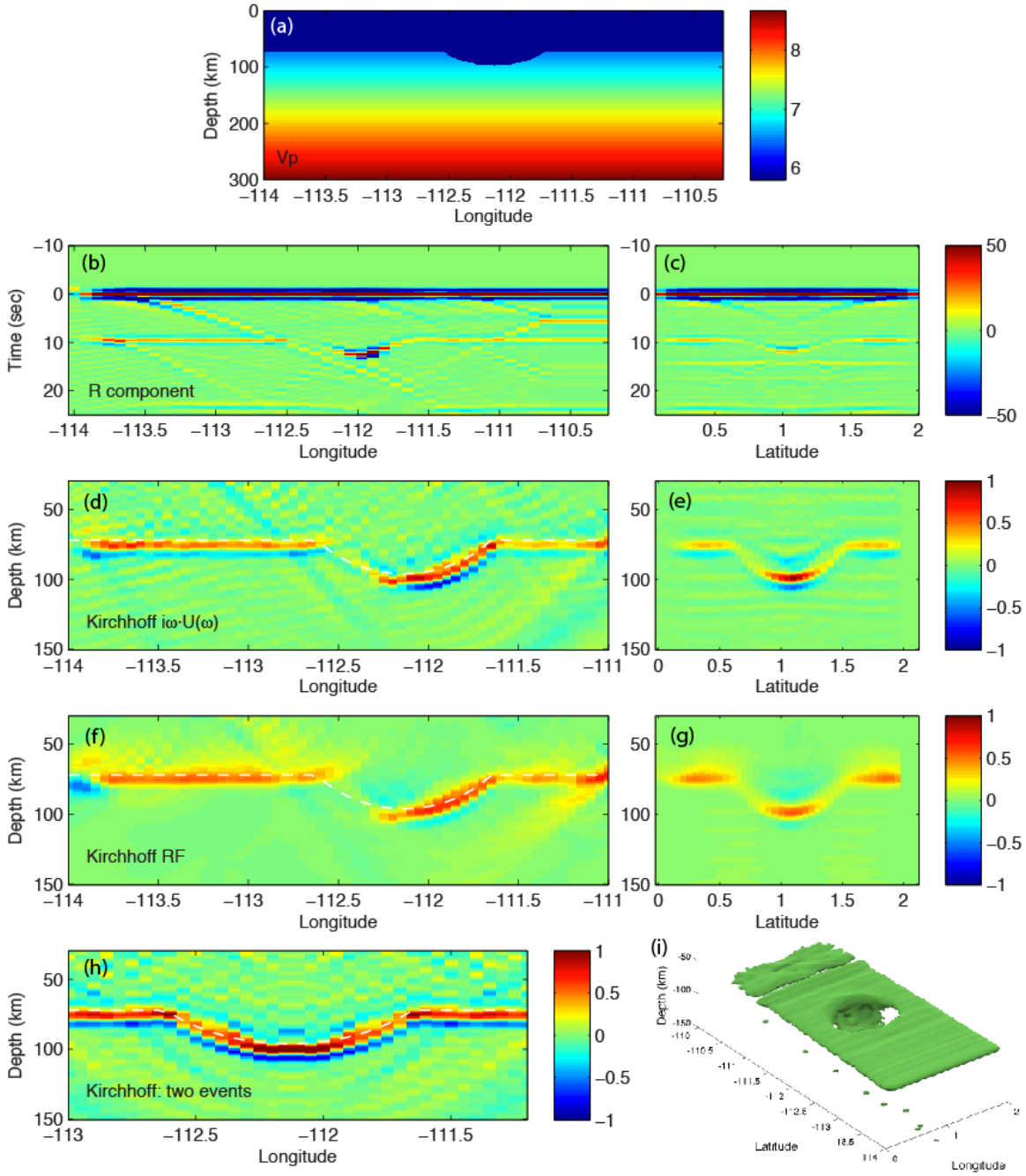

Figure 4.3 Kirchhoff-GRT images for a 'crater' model. (a) P-velocity model used for the synthetics. (b-c) Two radial component synthetic seismograms along the cross-sections of latitude=1.0°N and longitude=112°W, respectively. (d-e) Kirchhoff-GRT imaging results using the velocity seismograms as input, while (f-g) use the filtered RFs as input. (h) Imaging results from two events from east and west, respectively. White dashed lines shows the true location of the interface. (i) Isosurface of the Kirchhoff-GRT result in (d-e) for one event using velocity seismograms.

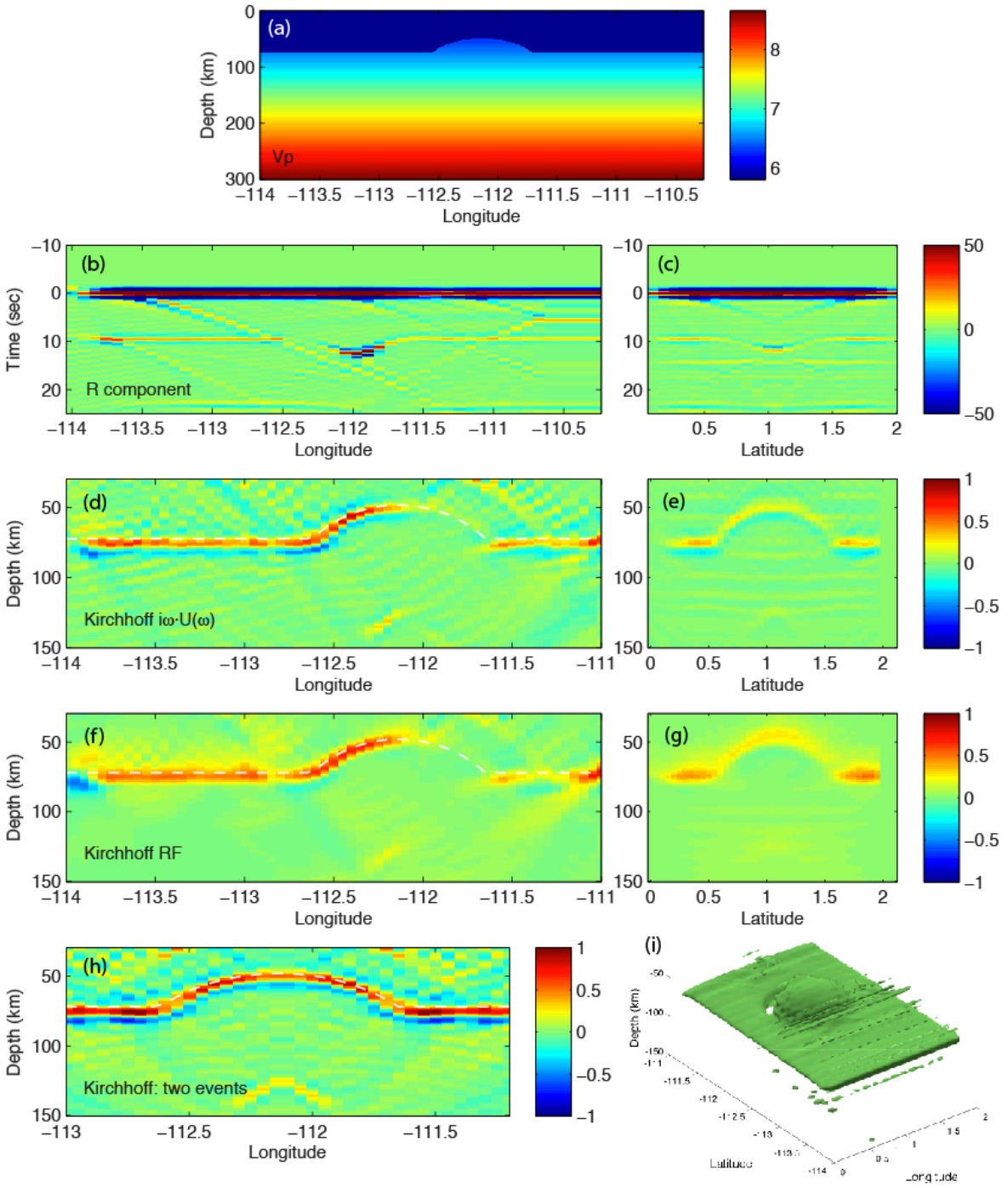

Figure 4.4 Kirchhoff-GRT images for a 'dome' model. (a) P-velocity model used for the synthetics. (b-c) Two radial component synthetic seismograms along the cross-sections of latitude=1.0°N and longitude=112°W, respectively. (d-e) Kirchhoff-GRT imaging results using the velocity seismograms as input, while (f-g) use the filtered RFs as input. (h) Imaging results from two events from east and west, respectively. White dashed lines shows the true location of the discontinuity interface. (i) Isosurface of the Kirchhoff-GRT result in (d-e) for one event using velocity seismograms.

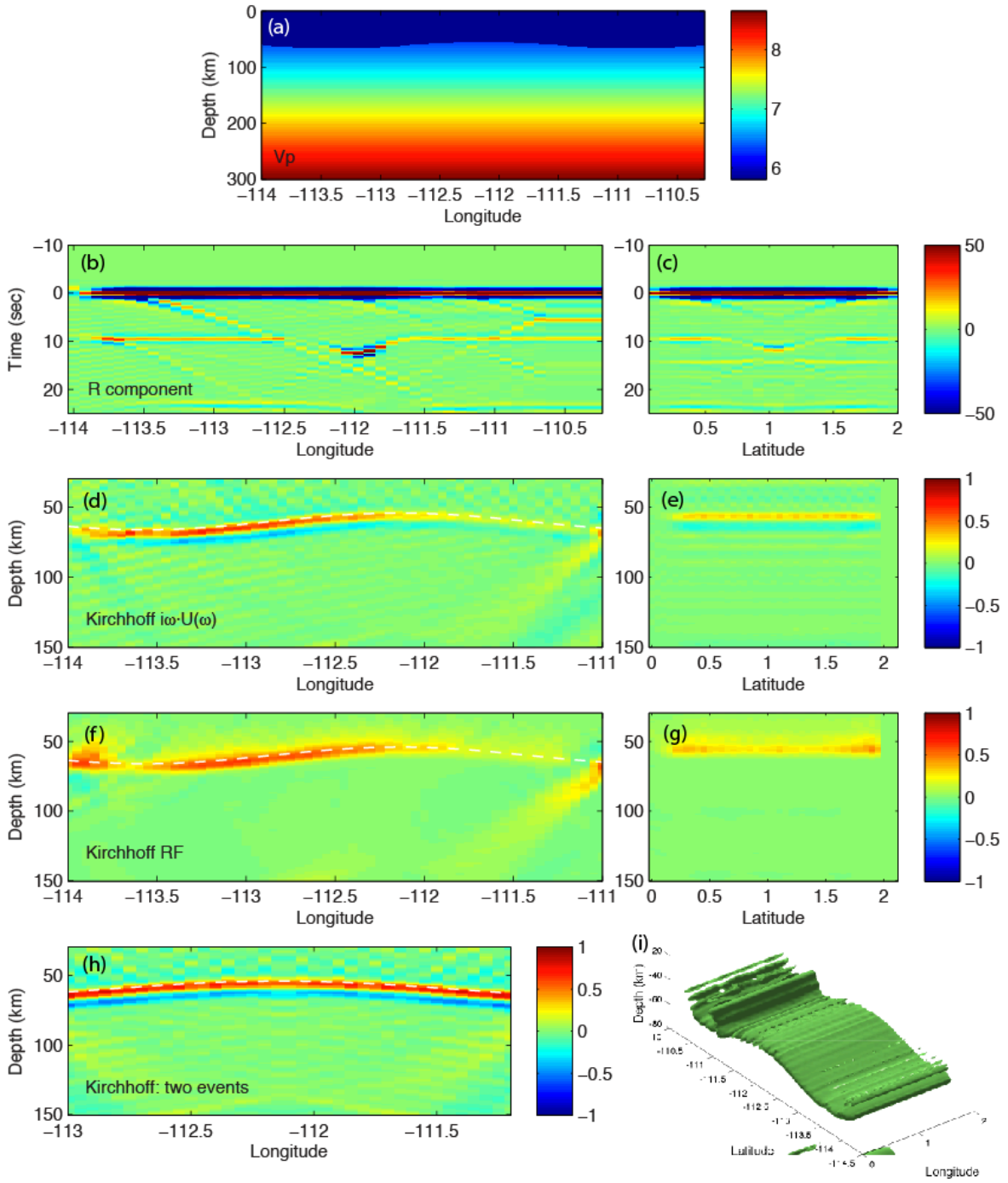

Figure 4.5 Kirchhoff-GRT images for a sinuous discontinuity model with a peak-to-peak amplitude of 12km (54-66 km). (a) P-velocity model used for the synthetics. (b-c) Two radial component synthetic seismograms along the cross-sections of latitude=1.0°N and longitude=112°W, respectively. (d-e) Kirchhoff-GRT imaging results using the velocity seismograms as input, while (f-g) use the filtered RFs as input. (h) Imaging results from two events from east and west, respectively. White dashed lines shows the true location of the discontinuity interface. (i) Isosurface of the Kirchhoff-GRT result in (d-e) for one event using velocity seismograms.

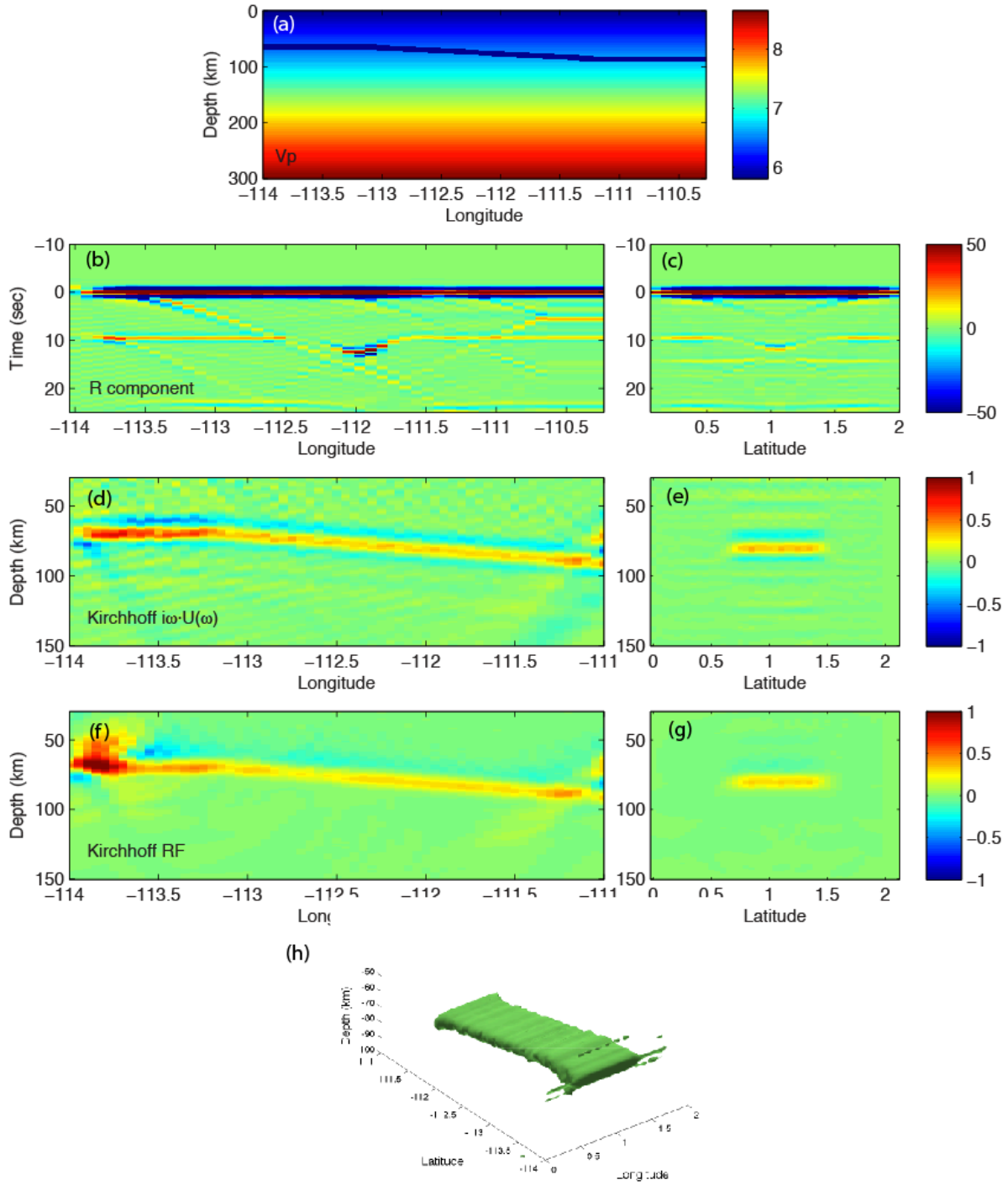

Figure 4.6 Kirchhoff-GRT images for a dipping layer model (9-km thickness with a dip of 5°). (a) P-velocity model used for the synthetics. (b-c) Two radial component synthetic seismograms along the cross-sections of latitude=1.0°N and longitude=112°W, respectively. (d-e) Kirchhoff-GRT imaging results using the velocity seismograms as input, while (f-g) use the filtered RFs as input. (h) Isosurface of the Kirchhoff-GRT result using velocity seismograms.

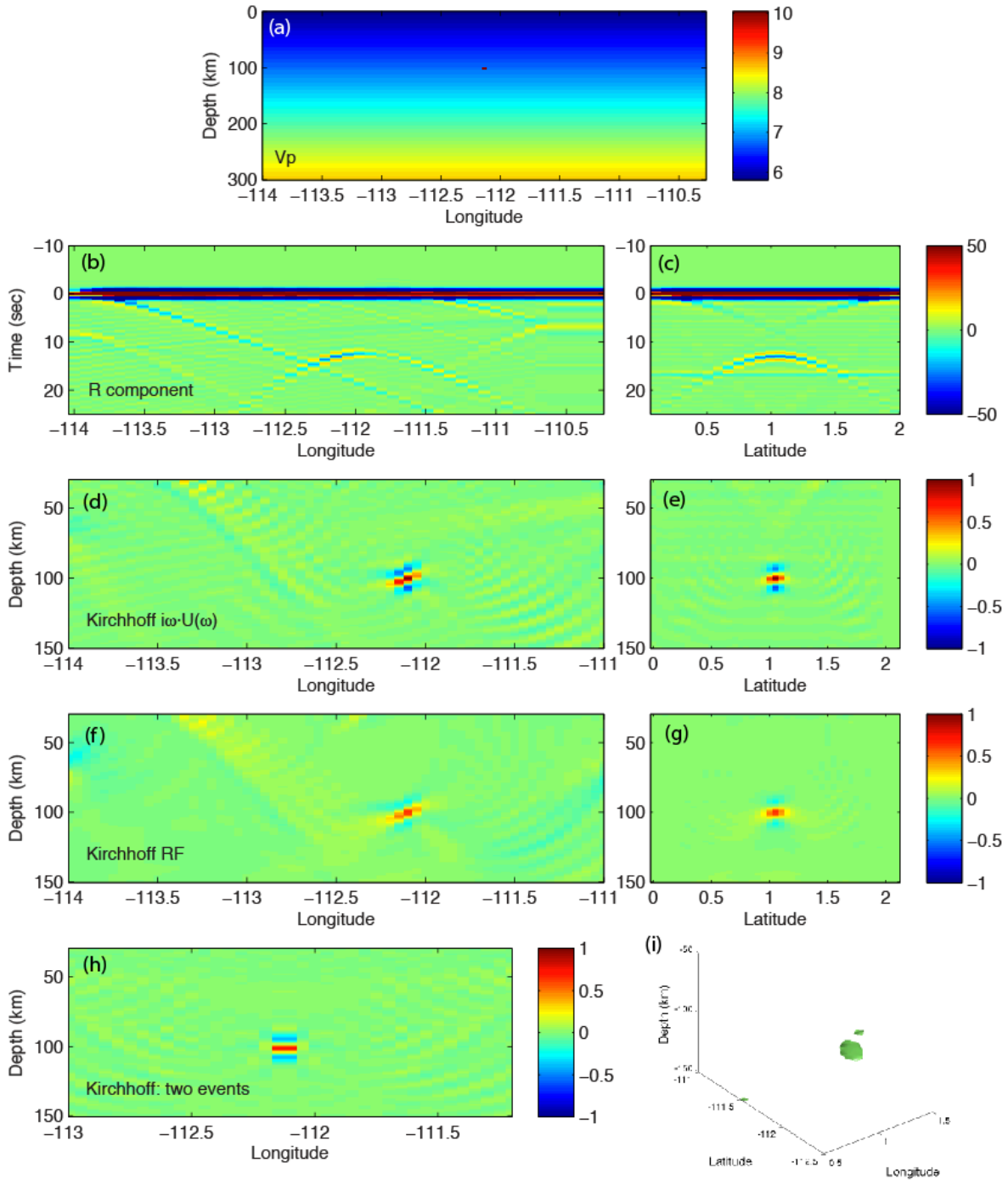

Figure 4.7 Kirchhoff-GRT images for a 'point' scatterer model at 100 km depth. (a) P-velocity model used for the synthetics. (b-c) Two radial component synthetic seismograms along the cross-sections of latitude=1.0°N and longitude=112°W, respectively. (d-e) Kirchhoff-GRT imaging results using the velocity seismograms as input, while (f-g) use the filtered RFs as input. (h) Imaging results from two events from east and west, respectively. (i) Isosurface of the Kirchhoff-GRT result in (d-e) for one event using velocity seismograms.

4.3.2.3 Dipping interface

Another geometry that illustrates how the scattered-wave migration produces better images than CCP stacked RFs involves dipping structures, such as subducted slabs. *Rondenay* [2009] has previously shown that a GRT migration technique will recover interfaces dipping at 35°, whereas the CCP-stacked image significantly underestimates dip angle. Here we test the imaging of a slab with a dip angle of 5° towards the east (Figure 4.6). A 9-km thick dipping layer separates horizontal interfaces at 60 km and 81 km depth. The Kirchhoff-GRT correctly resolves both the location and dip angle of the dipping layer.

4.3.2.4 'Point' scatterer

We next embedded a 2.4km×2.4km×2.4km 'point' scatterer with 8% model parameter perturbations at 100 km depth centered in the model (Figure 4.7). We illuminated it with two teleseismic P-waves, Although the scatterer size is less than half of the minimum wavelength (3.36 km) propagating in the imaging volume, our 3-D Kirchhoff-GRT code recovers both location and scatterer size well (Figure 4.7).

4.3.3 Multiple events and diffraction weighting function

Overall, these synthetic tests have successfully validated the efficacy of our 3-D Kirchhoff-GRT code to recover both curved ('crater', 'dome', sinuous, dipping models) surface and localized structure causing strong diffraction ('point' scatterer) for the idealized receiver configuration. More events from a range of distances and azimuths would provide better target illumination. For example, simply adding another teleseismic source from the east would dramatically improve the amplitudes of the curved structures that are weakly imaged due to nearly normal incidence, as shown in Figure 4.3h, 4.4h, 4.5h and 4.7h.

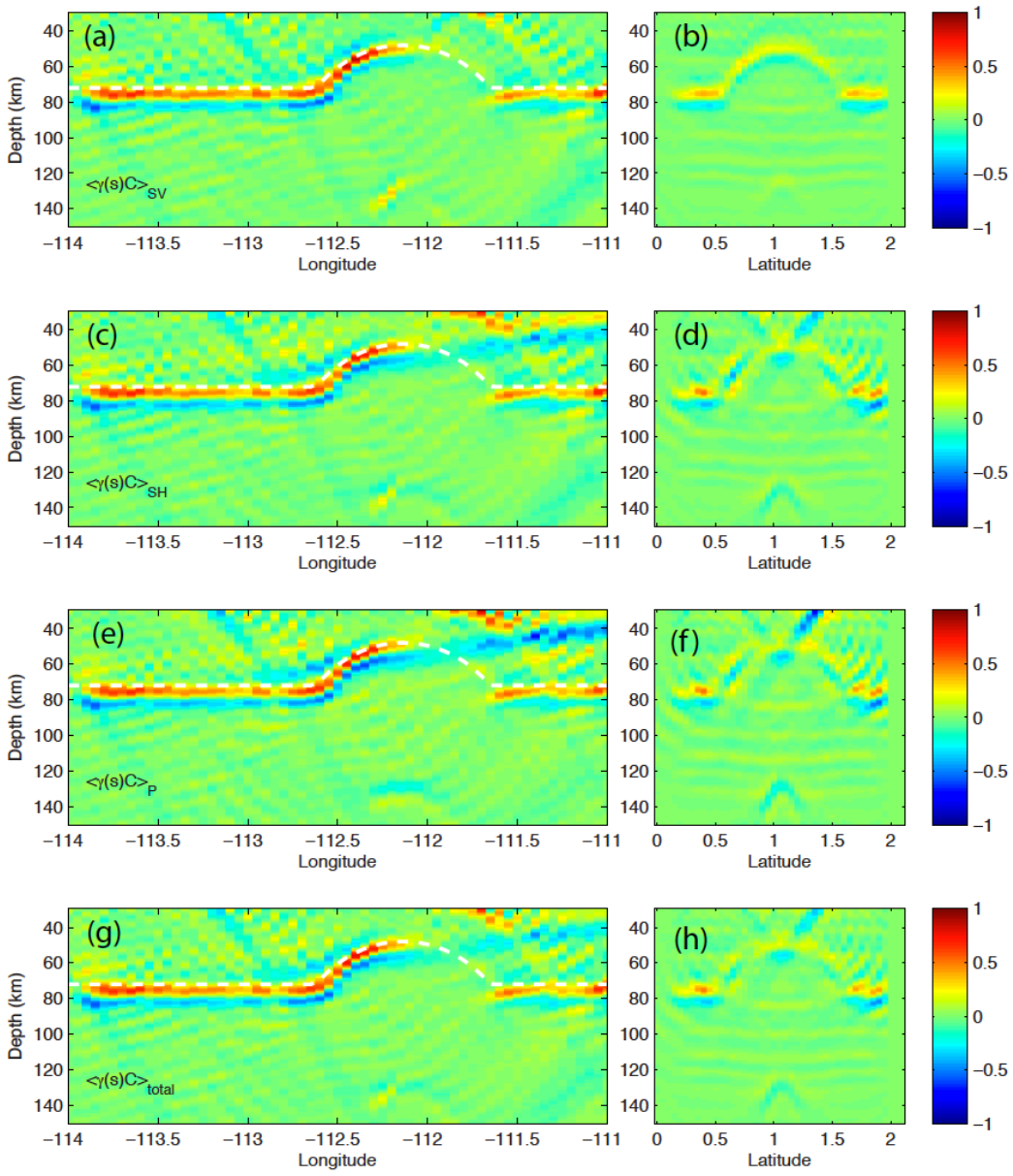

Figure 4.8 Transmission coefficient structure inverted using the S_V (a-b), S_H (c-d) and P (e-f) component velocity seismograms individually for the synthetic model of a 'dome' discontinuity interface shown in Figure 4.4(a). The bottom panel (g-h) is the final image using three components.

One advantage to our elastic migration method is the utilization of the scattered or leaked P-to-S converted energies along the S_H and P directions. This energy has been generally ignored in previous studies. As shown in the 'dome' model (Figure 4.8), the contribution of the S_H (Figure 4.8c, d) and P components (Figure 4.8e, f) to the final transmission coefficient

image is comparable to that of the S_V component (Figure 4.8a, b) in the elastic Kirchhoff-GRT imaging, although the S_V component has the clearest image.

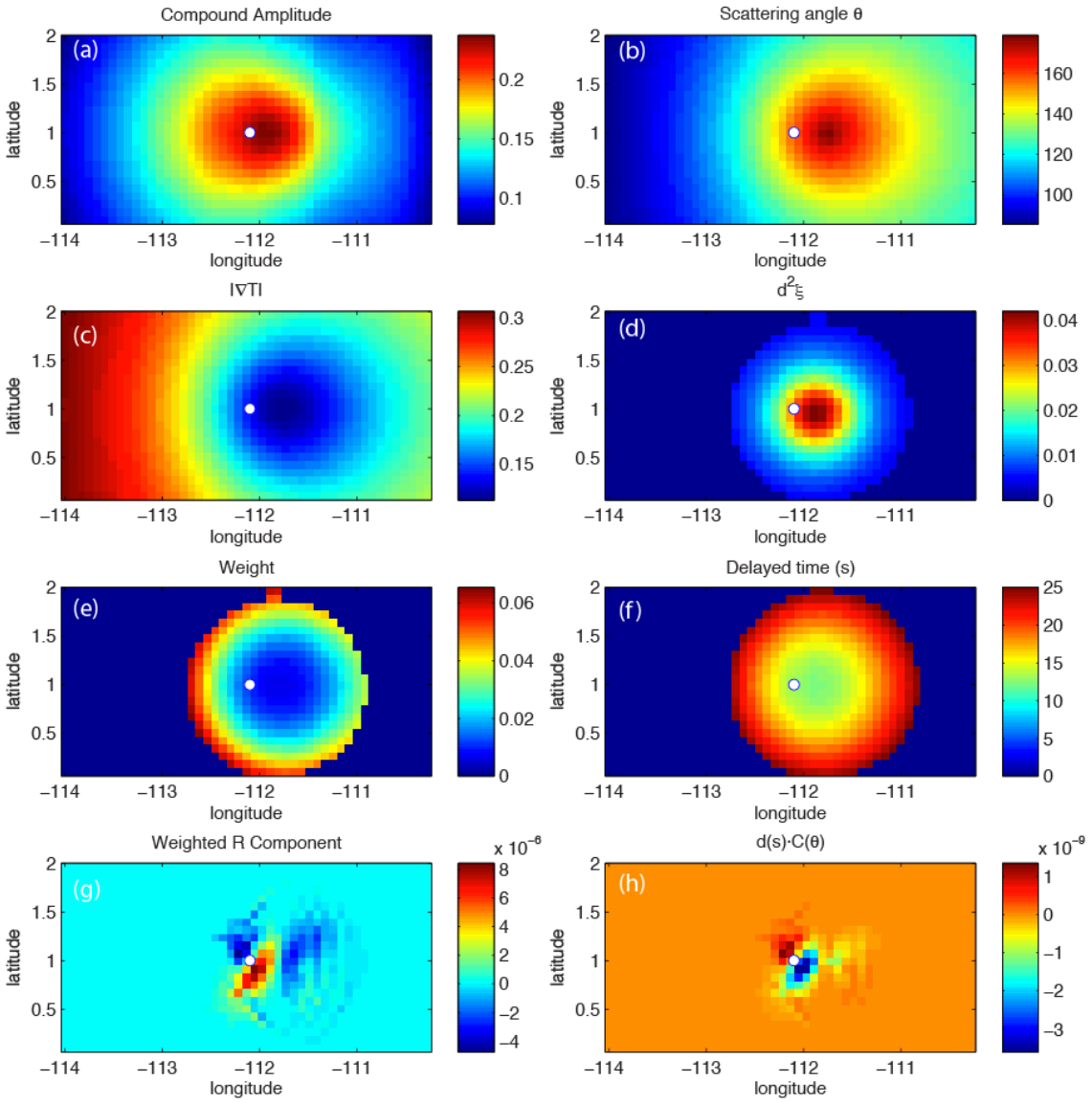

Figure 4.9 Kirchhoff-GRT imaging parameters for the 'point' model in Figure 4.7 at the imaging point (z=100 km, white dots), including (a) compound amplitude, (b) scattering angle, (c) gradient of compound traveltime $|\nabla T|$, (d) Jacobian, (e) weight, (f) time delays with respect to the direct P arrivals, (g) weighted R wavefields, and (h) transmission coefficient contribution.

The resolution obtainable using this Kirchhoff-GRT method depends upon the source/receiver configurations, and their associated coverage in the compound traveltimes,

scattering angles, and the numerical Jacobian, similar to those of the 2-D Born-GRT imaging [*Bostock et al*., 2001; *Shragge et al*., 2001; *Rondenay et al*., 2005]. Taking the 'point' scatterer model as an example, we plot the major factors that contribute to the diffraction stack weights at a given imaging point (112°W, 1°N, 100 km depth) in Figure 4.9. Near the surface location with the minimum total traveltime, the Jacobian reaches a maximum and decays sharply, while in contrast both the total traveltime gradients and the magnitude of the compound amplitude reduce the total stack weights, and thus increase the contribution from other receivers around the geometrical ray center.

4.4 Field data and discussion

To further demonstrate our 3-D Kirchhoff method, we apply it to two field datasets of passive seismic experiments in the western US. While there are several dense profiles, e.g., La RISTRA across the CP [*Wilson and Aster*, 2005] and Cascadia 1993-1994 (CASC93) in central Oregon [*Nabelek et al*., 1993; *Trehu et al*., 1994], these are suited to test a 2-D rather than 3-D theory. Very few flexible array experiments have suitable receiver configurations to apply the 3-D scattered-wave migration method. Density of permanent and Transportable Array seismic stations is too low for imaging using migration methods due to spatial aliasing. In this section, we show results from the teleseismic data from the FAME and HLP experiments. Both have relatively dense 3-D stations suitable for examining the Moho and other lithospheric structures. In both experiments stations were clustered along main profiles, but also distributed in an areal array, providing a good opportunity to apply the 3-D Kirchhoff-GRT method, emphasizing cross-sections along the dense profiles.

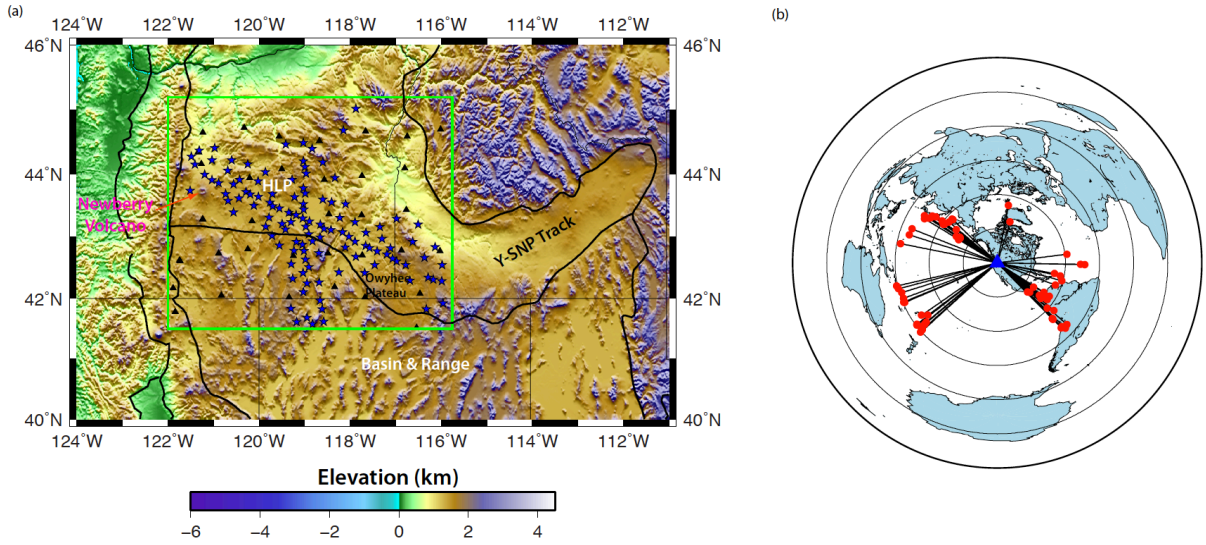

Figure 4.10 Station coverage (a) and distribution of teleseismic sources (b) used for the Kirchhoff-GRT imaging from the High Lava Plains seismic experiment. The blue stars in (a) are the HLP stations, while black triangles are the USArray TA and other regional networks. In (b), the red dots show the hypocenters of the earthquakes centered at the study region (blue triangle).

4.4.1 HLP seismic experiment

The HLP seismic experiment in the northwestern US (Figure 4.10a) was designed to improve the understanding of the origin of the extensive and large-volume intraplate magmatism that has been occurring since the Mid-Miocene in the HLP and its surrounding regions, east of the Cascadia subduction system [e.g., *Carlson et al.*, 2005; *Wagner et al.*, 2010; *Eagar et al.*, 2011]. Starting ~12 Ma, extensive eruption of flood basalt near the Owhyee Plateau resulted in two progressive silicic volcanism trends propagating in opposite directions: the northeastward Yellowstone/Snake River Plains (Y-SNP) track and the northwestward HLP track towards the Newberry Volcano in central Oregon. The former propagates roughly parallel to the plate motion direction of North America, suggesting it is driven by a deep mantle hotspot/plume source [e.g., *Pierce and Morgan*, 2009; *Smith et al.*, 2009], whereas the HLP track remains unexplained since it does not correlate well plate motion [e.g., *Meigs et al.*, 2009]. Although several mechanisms involving extension, rotation and slab rollback

[e.g., *Cross and Pilger*, 1982; *Carlson and Hart*, 1987] have been proposed to explain the voluminous back-arc volcanism within the continent, poor understanding of the formation and driving source of the HLP track motivated the seismic experiment. The HLP project deployed 118 broadband seismometers with an average station spacing of 15-20 km from central and eastern Oregon to western Idaho and northern Nevada [*Carlson et al*., 2005]. The Rayleigh wave tomography [*Wagner et al*., 2010] and CCP RF images [*Eagar et al*., 2010] utilizing these data reveal strong lateral Moho variation and large lithospheric heterogeneities within the tectonic blocks, and identify several distinct low-Vs anomalies beneath the HLP track.

To examine lithospheric structure more closely, we made 3-D Kirchhoff images using a total of 76 teleseismic events (Mb>5.6, 35°-90°, Figure 4.10b) with 8237 three-component seismograms recorded by the HLP and coeval USArray stations, as shown in Figure 4.10a. Most of the teleseismic body wave sources come from the northwest and southeast, as well as the southwest. We use three-component (S_V, S_H and P) GFs preprocessed by *Schmandt et al.* with a multichannel spectral deconvolution technique as described in *Baig et al.* [2005], *Mercier et al.* [2006], *Hansen and Dueker* [2009] and *Schmandt et al.* [2011]. These GFs are estimated by removing the source amplitude spectra using a log-spectral least square inversion, and reshaping the phase spectra using the minimum-phase characteristics of the P wave Green's function [*Bostock*, 2004]. We use these GFs (e.g., Figure 4.11) as input to construct the elastic Kirchhoff-GRT images with high-cut frequencies of both 1 and 0.5 Hz. We migrated in a grid of 0.08°×0.08°×1km and used the IASP91 model [*Kennett and Engdahl*, 1991] as the migration velocity model.

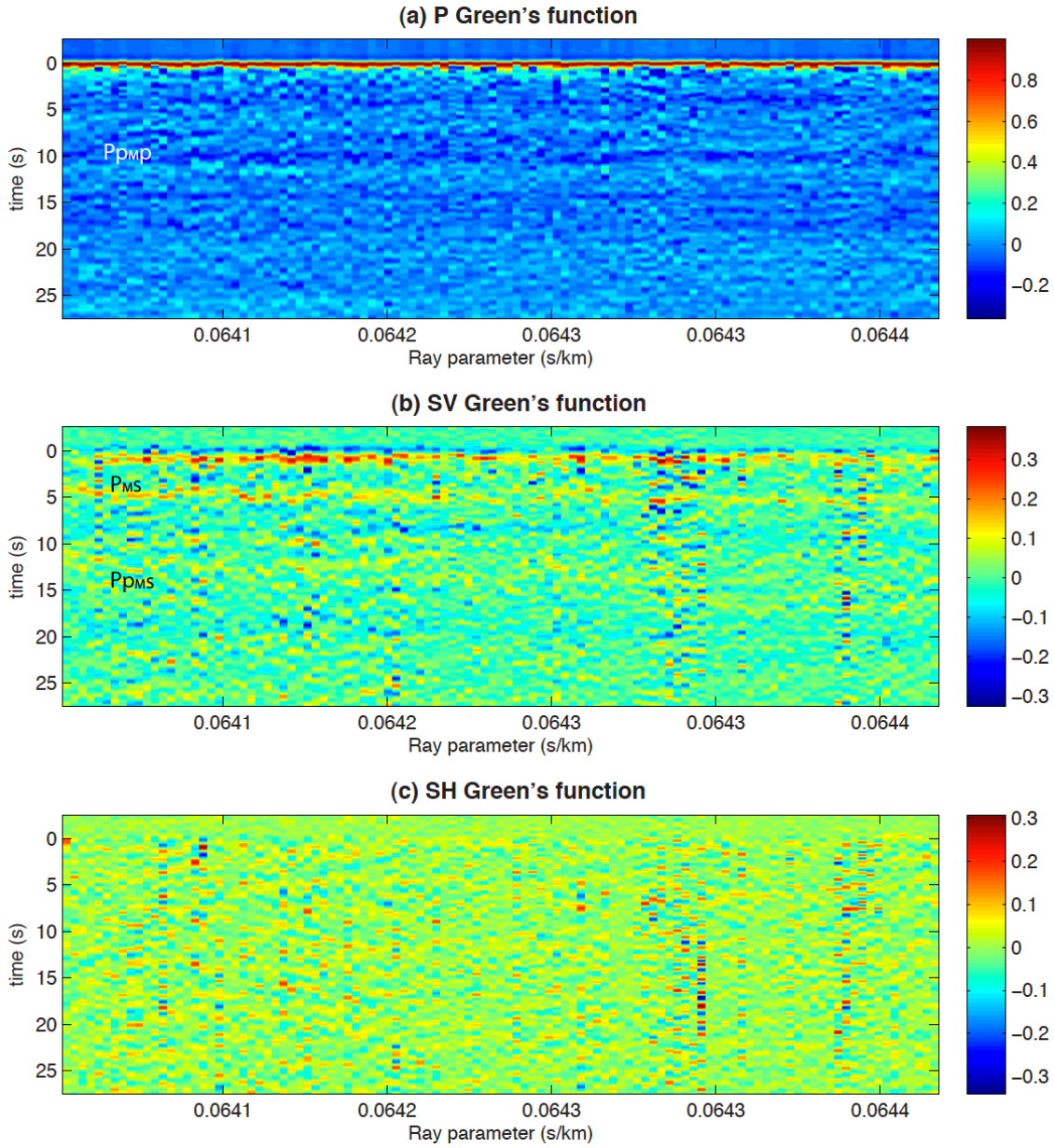

Figure 4.11 Three-component GFs of the HLP and TA stations for a teleseismic event (61.274°W, 14.944°N, depth=156 km). (a-c) are the P, S_V and S_H component GFs, respectively.

A hit count map (0.5 Hz, Figure 4.12) suggests that the migration results are most reliable along the NW-SE profile that has relatively large hit count numbers (>50). Figure 4.13(a) and 4.13(b-d) shows the Ps transmission coefficient structure contributed by the S_V direction alone as well as P and S_H. Two major features have clearly been imaged along this cross-

section roughly parallel to the HLP track, as shown in Figure 4.13-4.14. The first one is a lateral variation of Moho depth as indicated by the positive Ps transmission coefficient event (35-45 km) that is well captured in both frequency bands. The crust beneath the Newberry Volcano near the Cascadia arc has an average thickness of 42 km, and continues to shallow southeastward across the HLP region to a thickness of 35 km (Figure 4.13a). Further east, there is an abrupt increase in Moho depth from 35 to ~45 km occurring over less than 20 km between -117.5° and -117.8°. This abrupt change is quite consistent with the CCP image (35 to 42 km) and H-k analysis (31 to 38 km) [*Eagar et al*., 2011]. The CCP images are expected to have a relatively poor resolution of dipping or curved interfaces. In Figures 4.13 and 4.14, we observe a more continuous Ps conversion signal where the Moho deepens, more so in the $\langle \gamma(s)C \rangle_{S_V}$ image (Figure 4.13a), than in the CCP images (BB' cross-section in Figure 9c, *Eagar et al*., 2011). The location of the abrupt Moho variation defines the western edge of the relatively undeformed Owyhee Plateau [*Shoemaker*, 2004], coincident with the boundary of large lateral contrast of crustal Vs from the ANT [*Hason-Hedgecock et al*., 2012], as well as the sharp gradient of the $^{87}Sr/^{86}Sr$ isopleths of 0.704 [*Armstrong et al*., 1977].

Other notable features in the Kirchhoff GRT images are three negative events (blue events marked as L1: 120°-121°W, L2: 118°-119°W and L3: 117°-116°W) at approximate depths of 60-70 km (Figure 4.13 and 4.14). These three distinct, discontinuous negative Ps transmission coefficients correlate well with the top of low-Vs bodies imaged by the Rayleigh wave tomography using a two-plane-wave method [*Wagner et al*., 2010]. In the CCP RF image [*Eagar et al*., 2011], this feature is not obvious. The low Vs zones in the surface wave model are spatially discrete, in contrast to a continuous low-Vs anomaly

beneath the Y-SNP track. Previous dating studies [e.g., *Jordan et al.*, 2004] suggest similar time-progressive volcanism along the HLP trend as the Y-SNP trend. Using recently compiled rhyolitic data [*Meigs et al.*, 2009], *Wagner et al.* [2010] reinterpreted the 'kink' in the $^{40}Ar/^{39}Ar$ dating contours over-smoothed by *Jordan et al.* [2004]. The segregation of the early HLP volcanic track (12-7 Ma, similar to the Y-SNP branch) and the young volcanism west of the 'kink' is ascribed to the complicated interaction of two volcanic systems between the HLP and the N-S trending arc [*Wagner et al.*, 2010]. Analogous to marginal volcanism in the Basin and Range extension, the ongoing volcanism near the arc could result from HLP extension, as indicated by the crustal thinning observed both in the CCP [*Eagar et al.*, 2011] and the Kirchhoff-GRT images (Figure 4.13 and 4.14). The three distinct low-Vs anomalies indicate that the HLP volcanic system differs from the Y-SNP track.

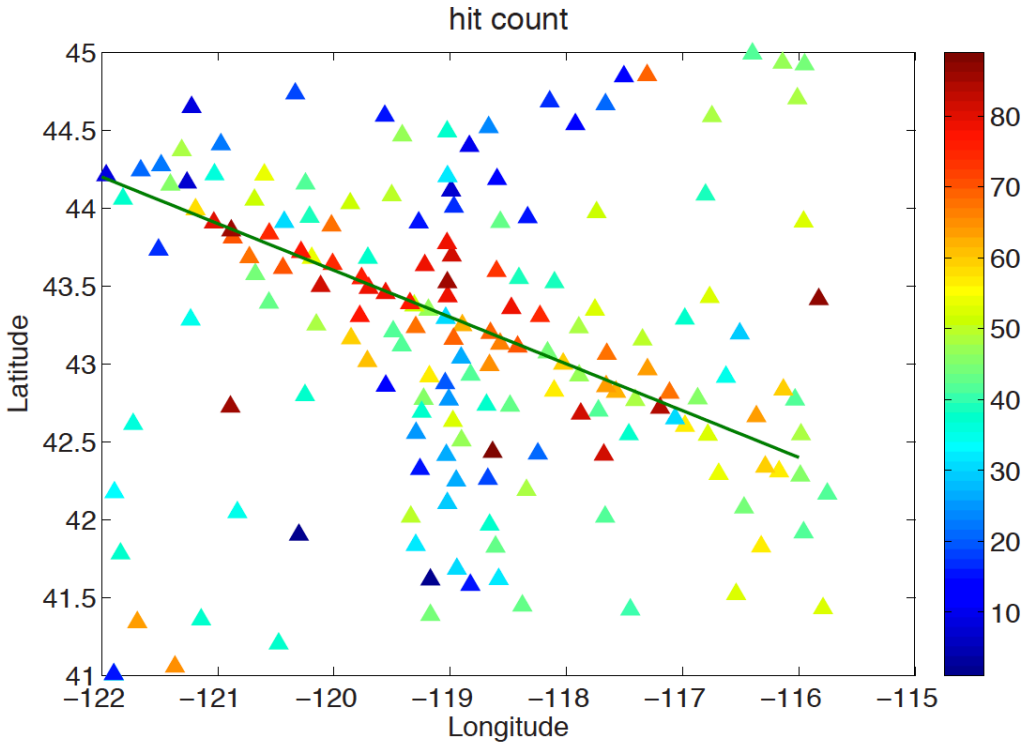

Figure 4.12 Hit count map for both 1.0 and 0.5 Hz Kirchhoff-GRT images. Stations with largest hit count numbers (>50) are distributed along the green profile.

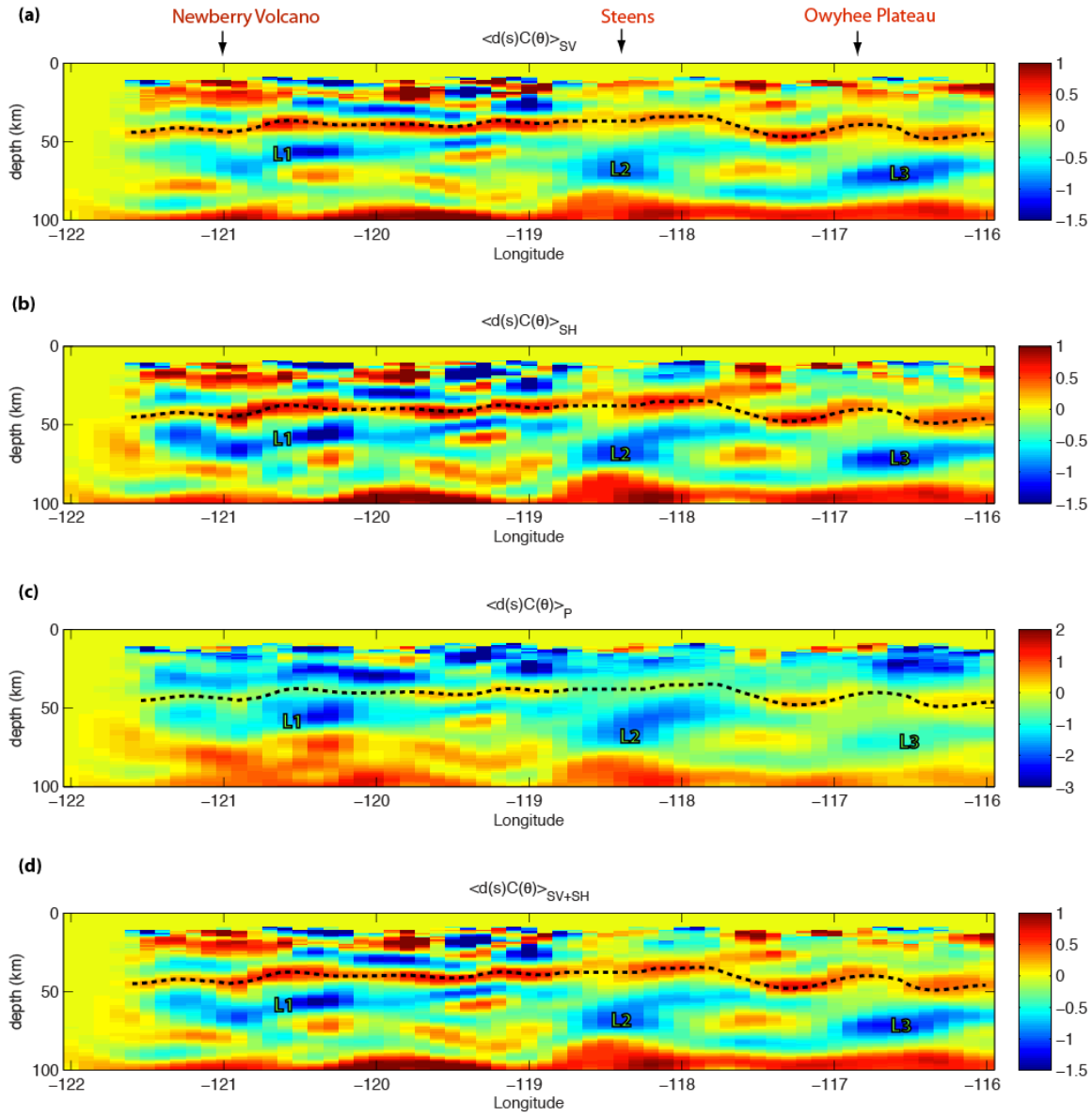

Figure 4.13 Cross-section of the Kirchhoff-GRT imaging result (0.5 Hz) along the green profile as marked in Figure 4.12. (a-d) shows the transmission coefficient images reconstructed from the S_V, S_H, P, and S_V+S_H, respectively. Positive amplitude means a low-to-high impedance jump viewed from the earth's surface. Dark dashed lines are originally picked in (a) and imposed on the remaining panels, as well as in Figure 4.14. L1-3 mark the three distinct negative transmission coefficients which correlate well with the top of three low Vs zones inverted from the Rayleigh wave dispersion curves.

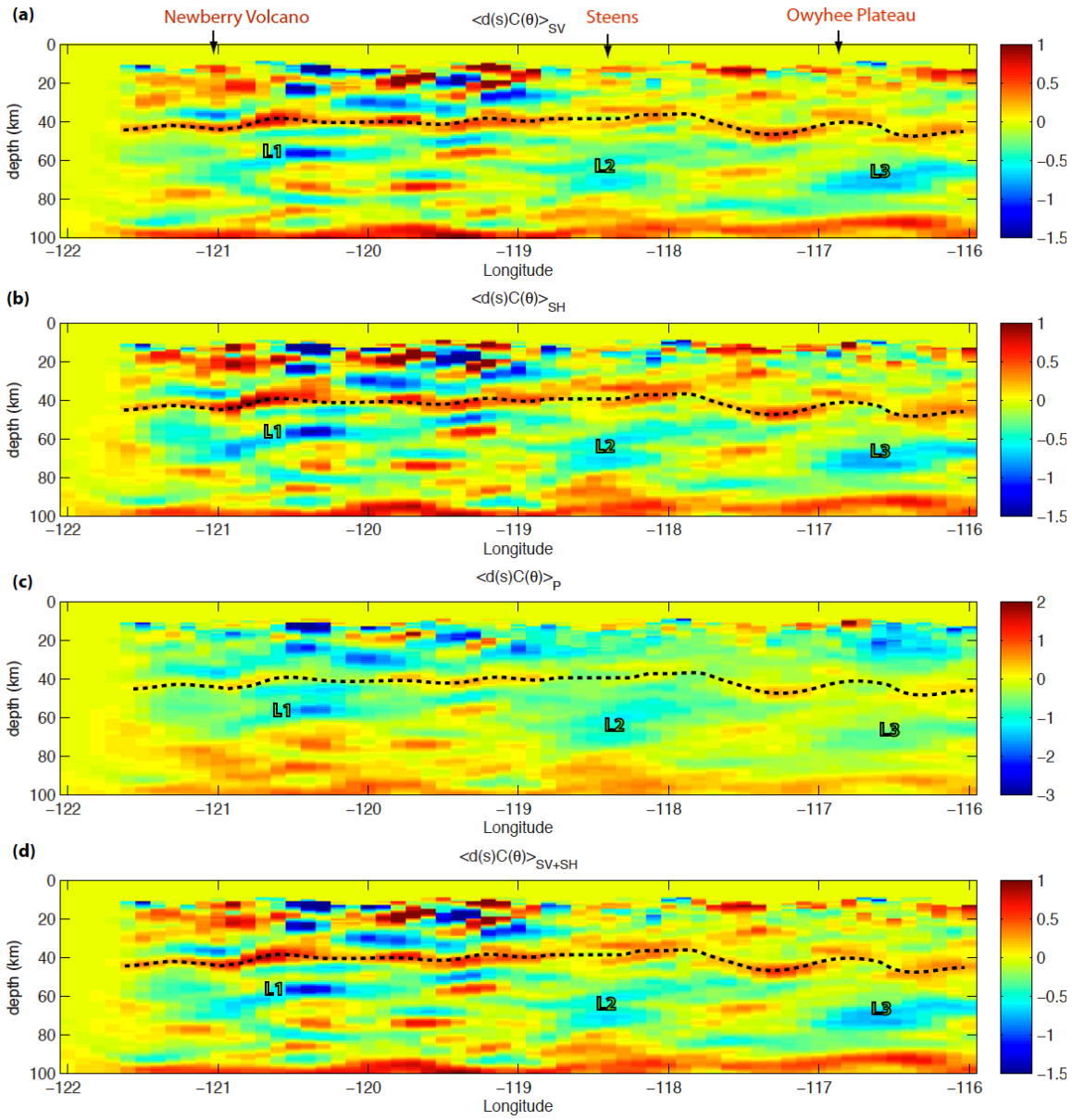

Figure 4.14 Kirchhoff-GRT cross-section at 1.0 Hz along the same profile as in Figure 4.13.

The negative event above Moho between the Newberry volcano and Steens Mountain correlates well with the negative amplitude in the CCP image and many other geophysical observations (high heat flow and crustal temperatures, high conductivity) [*Eagar et al*., 2011 and *references therein*], suggesting partial melt in the middle to lower crust. Another negative transmission coefficient event immediately below the Moho at ~50 km depth

between 119.6°W and 119.3°W could indicate a possible pathway of the crustal melt from the uppermost mantle across the Moho into the crust. It is also interesting to mention that another curved Moho above 'L3' is observed, especially in the S_V panel (Figure 4.13a and 4.14a), and in both 1 and 0.5 Hz. This transmission coefficient structure strongly resembles that of the 'dome' model in the synthetic test (Figure 4.4). However, the CCP result shows a flat feature in the region. Due to relatively sparse station coverage and low hit count numbers (Figure 4.12) compared to the rest in the profile, we cannot further resolve whether it is caused by artifacts of migration, or if it is true Moho structure.

4.4.2 Mendocino experiment in northern California

The FAME project consists of 89 broadband seismometers in the MTJ region deployed from 2007 to 2009 (Figure 4.15a) with additional Berkeley and USArray TA stations. Overall FAME had a station spacing of 25-35 km in a 4°x4° region in northern California, with a NW-SE embedded profile extending from Clear Lake to the Cascadia subduction zone having ~15 km spacing. The MTJ, which migrates to the NW, marks the ongoing transition from Cascadia subduction to the San Andreas transform system. The MTJ system has four distinct, young asthenospheres at relatively shallow depths (40 and 80 km); the slab window under the transform regime, the mantle wedge under the Cascade volcanoes, the Gorda asthenosphere, and the former mantle wedge now found beneath Great Valley-Sierra Nevada [*Liu et al*., 2012]. Using the FAME data, body-wave tomography [*Schmandt and Humphreys*, 2010], ambient noise tomography [*Porritt et al*., 2011], CCP RF [*Zhai*, 2010], and joint surface wave-RF inversion [*Liu et al*., 2012] studies have been conducted to provide better-resolved lithosphere and asthenosphere images.

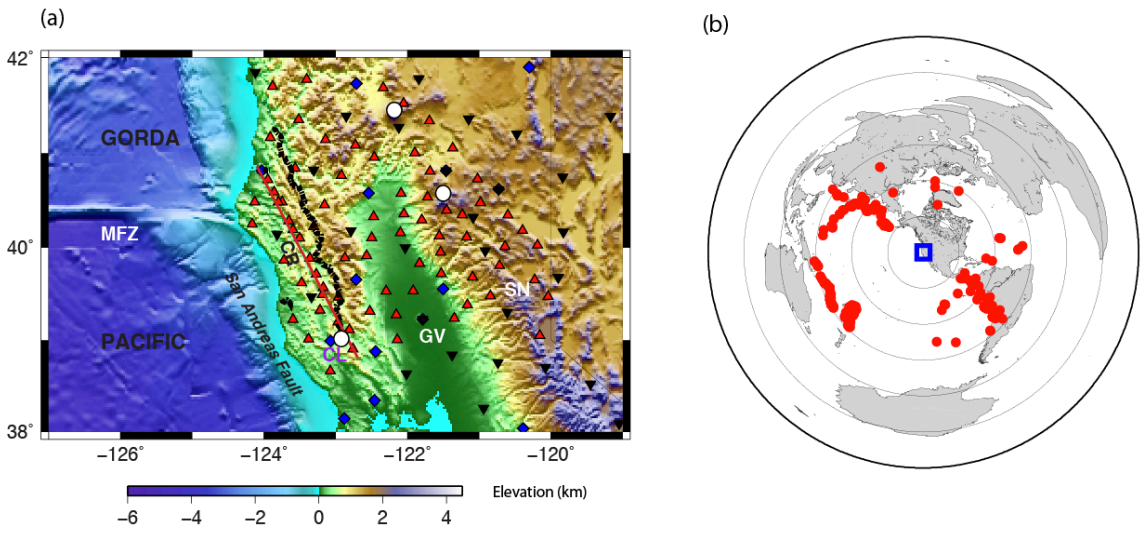

Figure 4.15 (a) Station location of the MTJ FAME experiment (FAME: red triangles; TA: inverse black triangles; BDSN: blue diamonds). White dots show the Cascadia arc and Coast Ranges volcanoes. (b) Distribution of the teleseismic events used for the radial and transverse RF calculation.

We applied the 3-D Kirchhoff method to examine the strong heterogeneity in the lithospheric and sublithospheric structures. We inverted for the Ps transmission coefficients using a total of 169 teleseismic events (Figure 4.15b). For this dataset we use the traditional RF technique to remove the source signatures in the radial and transverse components after separating the upgoing waves from the downgoing waves. As demonstrated in the 2-D GRT imaging [e.g., *Rondenay et al*., 2005], spatial aliasing distorts the images at depths above approximately twice the station spacing at 0.3 Hz. Here we focus on imaging results along the dense profile (red line in Figure 4.15a) close to the 1993-1994 MTJSE Line 9[e.g., *Beaudoin et al.*, 1996; 1998]. The station distribution along this cross-section is relatively dense (~15 km), so the Ps transmission coefficient image deeper than 30 km suffers little spatial aliasing, while the dipping resolution depends on the teleseismic source coverage. In this study, we performed the migration on a imaging grid of 0.1°×0.1°×1km and used three different migration velocity models: the IASP91 model, an averaged joint inversion model [*Liu et al*., 2012] and

a hybrid model combining the active source tomography model [*Beaudoin et al.*, 1996; 1998] in crust and the DNA body wave tomography model in upper mantle [*Obrebski et al*., 2010].

In Figure 4.16, we show the NW-SE cross-section of the Kirchhoff-GRT image, and for comparison, we include the crustal Vp model [*Beaudoin et al*., 1996], the CCP RF image [*Zhai*, 2010], as well as the joint inversion Vs structure [*Liu et al*., 2012]. The Kirchhoff GRT image shows a shallowing negative event extending from the subduction regime at ~65 km depth, to the slab window region at 30-50 km depth beneath the Clear Lake volcanic fields (Figure 4.16d). We interpret this event as the LAB, consistent with previous CCP (Figure 4.16b) and joint inversion (Figure 4.16c) studies. In the northwest, we interpret the deep LAB as the base of the subducted Gorda plate and thus estimate the lithospheric thickness of the young oceanic slab to be ~35 km. Using the magnetic anomalies offshore and plate subduction rates, we estimate the subducted plate beneath the profile to be ~8-13 Ma old. We note that the base of the plate from the Kirchhoff GRT image is ~5-10 km less than that estimated from the CCP cross-section. Relative to the CCP estimate, the Kirchhoff-GRT estimate is more consistent with both the half-space cooling model prediction (29-36 km), and the joint inversion estimate which images a slightly shallower base of the Gorda plate (high-Vs body in Figure 4.16c). Under the transform regime in the south, the extremely shallow LAB (30-50 km) supports the slab window hypothesis, which predicts that asthenospheric upwelling, following the MTJ migration, would infill the slab-gap region and thus decreases thermal/mechanical boundary layer depth significantly. We also note that the Kirchhoff-GRT and joint inversion images along this profile show that elements of the Gorda slab extend ~100 km south of the landward projection of the Mendocino Fracture zone.

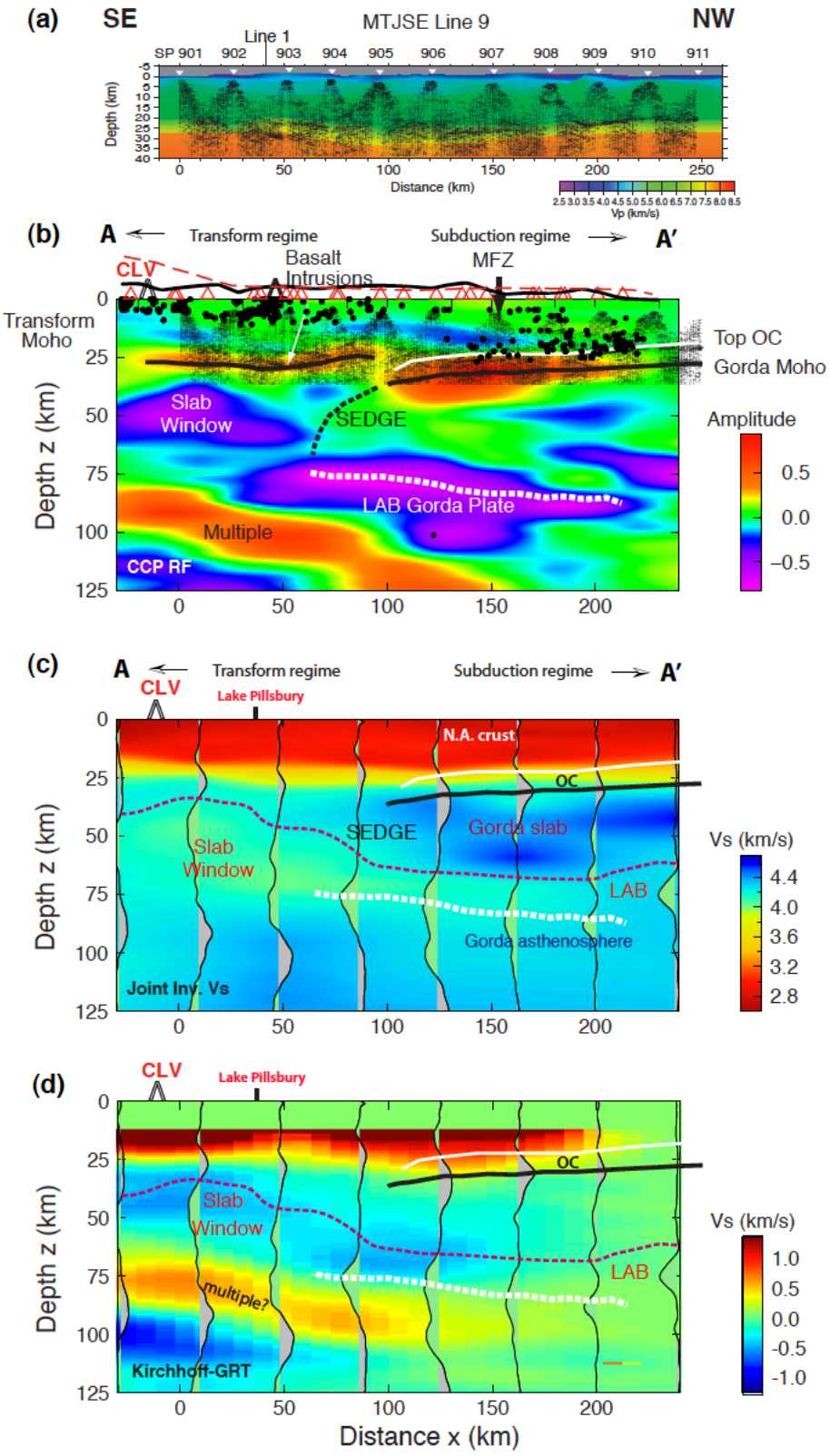

Figure 4.16 Comparison of the Kirchhoff image with Figure 2.15 in Chapter 2 along the NW-SE profile in Figure 4.15a.

4.4.3 Advantages, limitations and challenges in practical application

For both synthetic and field data, the Kirchhoff-GRT imaging technique has a higher resolving power for imaging a heterogeneous subsurface than CCP imaging. Moreover, we take full advantage of the three-component data to reconstruct high-resolution lithospheric structures, using the S_V, S_H, and P components, the last two of which are typically ignored in CCP imaging. Each component recovers comparable Ps transmission coefficient structure, although the S_V component, having the most energy, usually gives the clearest one.

Despite its successful application, the 3-D Kirchhoff technique has its own limitations due to the requirement of having a dense array and its computational cost. The Kirchhoff-GRT method functions best when both the source and receiver spaces are well sampled, the sources in azimuth and distance, and the receivers in density and array aperture. Inadequate station density or array aperture will introduce intrinsic migration artifacts to the final image that cannot be removed. In most passive experiments, the aperture requirements are only partially met giving incomplete sampling of the unit sphere in the surface integral at any imaging point (Eq. 24). One of the important factors determining image resolution is the spatial gradient of the compound traveltime. The teleseismic source distribution for the field data (Figure 4.10a and 4.15a) cannot provide ideal sampling of the total traveltime gradients, in these examples resulting from poor source coverage from the NE and south. Virtually any location on earth will suffer from a poor azimuthal and/or distance source sampling.

4.5 Summary

We have presented a 3-D Kirchhoff-approximation scattered wave imaging technique for teleseismic data for imaging upper mantle, receiver-side structure. We first derived the 3-D

P-to-S formula using the Kirchhoff-Helmholtz integral, and then rearranged the integral to identify a 3-D inverse GRT. We have tested the algorithm on several models using 3-D finite-difference synthetic seismograms. The synthetic tests demonstrate the imaging capability of the method for continuous irregular interfaces separating different elastic media, and for localized point scatterers that produce strong diffractions. In addition to the S_V component, we make use of scattered energy that is distributed in the S_H and P directions as a consequence of an inherently 3-D target geometry. This energy has been typically ignored in previous studies.

We have also applied the method to two flexible array field datasets from experiments in the western US. Application to preprocessed HLP data results in the clear imaging of Moho depth variations and three negative upper mantle events along the HLP track. The latter correlate well with the top of three low-Vs zones observed in the Rayleigh wave tomography model. The Kirchhoff GRT method resolves an abruptly deepening Moho with more reconstructed amplitudes at the western edge of the Owyhee Plateau, which is relatively poorly imaged with CCP methods. From the MTJ experiment, the new image made by the Kirchhoff GRT technique clearly identifies the rapid decrease in LAB depth from the bottom of the subducted Gorda plate into the slab window region under the transform regime. The image is consistent with a Vs model from a joint inversion of Rayleigh wave phase velocities and RFs. Although limited by logistically feasible receiver array configurations and imperfect source occurrence, the 3-D Kirchhoff-GRT technique provides a promising tool for producing more highly resolved images of complicated structures in the lower crust and upper mantle than can be made with 2-D or CCP methods.

Chapter 5 CONCLUSIONS

In this thesis, we have constructed two new 3-D Vs models and a new teleseismic imaging technique to better image the effects of Cenozoic tectonism and magmatism on the modern lithospheric structures in the western United States. Both LAB depth variations and upper mantle heterogeneity in the Mendocino Triple Junction and Colorado Plateau regions have been significantly affected by hydration and weakening of the basal lithosphere that occurred during and after the Laramide Farallon flat-slab subduction. Seismic resolution of the lower crust and uppermost mantle is greatly improved by constraints from surface wave data in both regions. We have also developed a new teleseismic imaging technique with Kirchhoff approximation to improve resolution of finer-scale structures compared to tomography images or traditional imaging methods (e.g., CCP stacking). In this study, we have integrated multiple seismic imaging techniques, including receiver functions [*Langston*, 1979; *Vinnik*, 1977; *Dueker and Sheehan*, 1997; *Ligorria and Ammon*, 1999; *Kumar et al*., 2005], ambient noise tomography [*Shapiro et al*., 2005; *Bensen et al*., 2007; *Snieder*, 2004], surface wave tomography [*Forsyth and Li*, 2005; *Yang and Forsyth*, 2006b], joint inversion of surface waves and receiver functions [*Julia et al*., 2000], and GRT imaging [*Miller et al*., 1987; *Beylkin and Burridge*, 1990; *Bostock and Rondenay*, 1999; *Bostock et al*., 2001; *Bostock*, 2002; *Poppeliers and Pavlis*, 2003a].

In the Mendocino triple junction, we have developed a new 3-D Vs model using a combined dataset with 111 stations from the USArray TA, FAME and BDSN networks. We first inverted for Rayleigh wave phase velocities (22-100 s) using finite-frequency Rayleigh wave

tomography. Then by combing ballistic phase velocities with ambient noise phase velocities, we develop a 3-D Vs model by joint inversion of Rayleigh wave phase velocities using RFs in two different frequency bands at each station. In the crust, we have observed a low-Vs zone associated with the Coast Range Franciscan Complex and a relatively high-Vs associated with the Great Valley ophiolite. Low Vs in the uppermost mantle is evidence of forearc mantle serpentinization, previously observed further north along the Cascadia margin [*Bostock et al.*, 2002]. In addition to the young Gorda asthenosphere, we have identified three additional asthenospheres resulting from different partial melting mechanisms. Removal of the Gorda slab causes mantle flow both from the suboceanic asthenosphere and from the cooling former mantle wedge, the latter is imaged here for the first time as the low-Vs 'GV-SN' anomaly. These two mantle flows started to mix in the slab-free region near the slab edge. We speculate that the 'GV-SN' anomaly provides the mantle wedge geochemical signature observed in the Coast Range volcanic rocks, and reconciles the slab window models and the geochemical data. Moreover, the proposed upwelling model explains the 3 Myr delay in the onset of Clear Lake volcanism after the MTJ migration.

In Chapter 2, we apply the surface wave tomography technique in a region (116°W-105°W, 32°N-42°N) encompassing the Colorado Plateau, Rio Grande Rift and parts of the southern Rocky Mountains and Basin and Range in the WUS, and present a new 3-D Vs model using the USArray data. We obtain the crustal and upper mantle Vs model from a regular grid inversion of Rayleigh wave phase velocity dispersion curves (20-167 s). This surface wave model provides estimates of the LAB depth that are consistent with a companion RF study [*Levander et al.*, 2011; *Levander and Miller*, submitted]. In the upper mantle, strong lateral

Vs heterogeneity is mainly attributed to 200-400 K variations in temperature and ~1% partial melt in low-Vs regions. We clearly image the upper mantle low velocities related to magmatic encroachment of the CP margins. These low velocities resulted from the convective removal of the CP lithosphere that had been rehydrated, refertilized and further destabilized. A large step in lithospheric thickness and a sharp thermal gradient between the plateau and the extended BRP and RGR drives an outside-in convective lithospheric erosion towards the Proterozoic lithospheric core of the plateau. Moreover, we image parts of a high-velocity drip under the western CP, providing another line of seismic evidence, with RFs and body wave tomography [*Levander et al*., 2011], for ongoing convective lithospheric downwelling. The regional delamination-style downwelling processes are a manifestation of widespread 3-D thermo-chemical edge convective erosion, and could thus provide additional buoyancy for the uplift of the CP margins relative to its center.

We developed a new 3-D teleseismic mode-conversion scattered wave imaging technique. As an extension of the 2-D GRT approach [*Bostock*, 2002], we develop a Kirchhoff-approximate theory to migrate scattered waves in 3-D. We first derive the P-to-S migration formula using the GRT solution and illustrate the Kirchhoff-GRT method using finite-difference synthetic seismograms from several 3-D models. Then, we apply the technique to two flexible array datasets: the FAME data described in Chapter 2 and the HLP data. The migrated Ps RF data from the FAME dataset clearly image the rapid decrease of LAB depth from 65-70 km beneath the subducting Gorda Plate to 30-50 km beneath the slab window. The final image is consistent with and complements the joint inversion model in Chapter 2. The Kirchhoff-GRT image is a significant improvement over Ps CCP stacks. From the HLP data, we use three-

component Green's functions to construct images that show a continuous, undulating Moho and three negative events at 50-80 km depth. The Moho is more clearly imaged than in a CCP study [*Eagar et al*., 2011], particularly at the western edge of the Owyhee Plateau. The three upper mantle negative events correlate well with the top of the three low-Vs zones identified in the HLP mantle by Rayleigh wave tomography [*Wagner et al*., 2010]. Another negative event (~50 km depth) immediately below the Moho (119.6°W-119.3°W) could indicate a pathway of partial melt in the middle to lower crust, as indicated by the strong negative transmission coefficient between the Newberry Volcano and Steens Mountains and other evidence, from the uppermost mantle. Using both synthetic and field data, we demonstrate that the 3-D Kirchhoff-GRT technique has the potential to image complicated lithospheric structures that are poorly resolved or unresolved by more traditional methods.

LIST OF REFERENCES

Abt, D.L., K.M. Fischer, S.W. French, H.A. Ford, H. Yuan, and B. Romanowicz (2010), North American lithospheric discontinuity structure imaged by *Ps* and *Sp* receiver functions, *J. Geophys. Res.*, *115*, B09301, doi:10.1029/2009JB006914.

Aki, K. and P.G. Richards (2002), *Quantitative Seismology* – 2nd Edition, University Science Books.

Aldrich, M.J., Jr., C.E. Chapin, and A.W. Laughlin (1986), Stress history and tectonic development of the Rio Grande Rift, New Mexico*, J. Geophys. Res.*, 91, 6199–6211.

Amante, C., and B.W. Eakins (2009), ETOPO1 1 Arc-Minute Global Relief Model: Procedures, Data Sources and Analysis, *NOAA Technical Memorandum NESDIS NGDC*-24.

Armstrong, R.L., and P. Ward (1991), Evolving geographic patterns of Cenozoic magmatism in the North American Cordillera: The temporal and spatial association of magmatism and metamorphic core complexes, *J. Geophys. Res*., 96, 13,201–13,224.

Armstrong, R.L., W.H. Taubeneck, and P.O. Hales (1977), Rb-Sr and K-Ar geochronometry of Mesozoic granitic rocks and their Sr isotopic composition, Oregon, Washington, and Idaho, *Geol. Soc. Am. Bull*., 88, 397–411.

Atwater, T. (1970), Implications of plate tectonics for the Cenozoic tectonic evolution of western North America, *Bull. Geol. Soc. Amer.*, *81*, 3513-3536.

Baig, A.M., M.G. Bostock, and J.P. Mercier (2005), Spectral reconstruction of teleseismic P Green's functions, *J. Geophys. Res.*, 110, B08306, doi:10.1029/2005JB003625.

Bailey, I.W., M.S. Miller, K.Liu, and A. Levander (2012), VS and density structure beneath the Colorado Plateau constrained by gravity anomalies and joint inversions of receiver function and phase velocity data, *J. Geophys. Res*., 117, B02313.

Beaudoin, B.C., N.J. Godfrey, S.L. Klemperer, C. Lendl, A.M. Trehu, T.J. Henstock, A. Levander, J.E. Holl, A.S. Meltzer, J.H. Luetger, and W.D. Mooney (1996), Transition from slab to slabless: Results from the 1993 Mendocino triple junction seismic experiment, *Geology*, 24, 195-199.

Beaudoin, B.C., J.A. Hole, S.L. Klemperer, and A.M. Trehu (1998), Location of the southern edge of the Gorda slab and evidence for an adjacent asthenospheric window: Results from seismic profiling and gravity, *J. Geophys. Res.*, *103*(B12), 30101-30115.

Bensen, G.D., M.H. Ritzwoller, M.P. Barmin, A.L. Levshin, F. Lin, M.P. Moschetti, N.M. Shapiro, and Y. Yang (2007), Processing seismic ambient noise data to obtain reliable broad-band surface wave dispersion measurements, *Geophys. J. Int.*, *169*(3), 1239-1260.

Bensen, G.D., M.H. Ritzwoller, and Y. Yang (2009), A 3D shear velocity model of the crust and uppermost mantle beneath the United States from ambient seismic noise, *Geophys. J. Int*., 177(3), 1177-1196.

Benz, H.M., and J. McCarthy (1994), Evidence for an upper mantle low velocity zone beneath the southern Basin and Range-Colorado Plateau transition zone, *Geophys. Res. Lett*., 21, 509–512.

Benz, H.M., G. Zandt, and D.H. Oppenheimer (1992), Lithospheric Structure of Northern California from Teleseismic Images of the Upper Mantle, *J. Geophys. Res.*, *97*(B4), 4791-4807.

Beydoun, W., and S. Jin (1994), Born or Kirchhoff migration/inversion: What is the earth's point of view?, *SPIE Proc., Mathematical Methods in Geophysical Imaging II*, 82–87.

Beylkin, G. (1985), Imaging of discontinuities in the inverse scattering problem by inversion of a causal generalized Radon transform, *J. Math. Phys*., 26, 99–108.

Beylkin, G., and R. Burridge (1990), Linearized inverse scattering problems in acoustics and elasticity, *Wave Motion*, 12, 15-52.

Bleistein, N. (1987), On the imaging of reflectors in the earth, *Geophysics*, 52, 931–942.

Bleistein, N., J.K. Cohen, and J.W. Stockwell (2000), Mathematics of multidimensional seismic inversion, Springe.

Bird, P. (1979), Continental delamination and the Colorado Plateau, *J. Geophys. Res.*, 84, 7561-7571.

Bird, P. (1988), Formation of the Rocky Mountains, western United States: A continuum computer model, *Science,* 239, 1501-1507.

Blake, M., A. Jayko and R. McLaughlin (1985), Tectonostratigraphic terranes of the northern Coast Ranges, California, *ectonostratigraphic Terranes of the Circum-Pacific Region*.

Blakely, R.J., T.M. Brocher, and R.E. Wells (2005), Subduction-zone magnetic anomalies and implications for hydrated forearc mantle, *Geology*, 33(6), 445-448.

Bostock, M.G. (2002), Kirchhoff-approximate inversion of teleseismic wavefields, *Geophys. J. Int.*, 149, 787-795.

Bostock, M.G. (2004), Green's functions, source signatures, and the normalization of teleseismic wave fields, *J. Geophys. Res*., 109, B03303.

Bostock, M.G. (2007), Teleseismic Body-Wave Scattering and Receiver-Side Structure, *Treatise on Geophysics, Volume 1, Seismology and the structure of the earth*, Elsevier, Eds. B. Romanowicz and A. Dziewonski, 219-246.

Bostock, M.G., and S. Rondenay (1999), Migration of scattered teleseismic body waves, *Geophys. J. Int*., 137(3), 732– 746.

Bostock, M., S. Rondenay, and J. Shragge (2001), Multiparamter twodimensional inversion of scattered teleseismic body waves: 1. Theory for oblique incidence, *J. Geophys. Res*., 106, 30,785– 30,796.

Bostock, M.G., R.D. Hyndman, S. Rondenay, and S.M. Peacock (2002), An inverted continental Moho and serpentinization of the forearc mantle, *Nature*, 417(6888), 536-538.

Brocher, T.M., T. Parsons, A.M. Trehu, C.M. Snelson, and M.A. Fisher (2003), Seismic evidence for widespread serpentinized forearc upper mantle along the Cascadia margin, *Geology*, *31*(3), 267-270.

Buehler, J.S., and P.M. Shearer (2010), Pn tomography of the western United States using USArray, *J. Geophys. Res.*, *115*, B09315, doi:10.1029/2009JB006874.

Burdick, S., C. Li, V. Martynov, T. Cox, J. Eakins, L. Astiz, F. Vernon, G. Pavlis, and R. van der Hilst (2008), Upper mantle heterogeneity beneath North America from travel time tomography with global and USArray transportable array data, *Seism. Res. Lett.*, 79, 384-392.

Burdick, S., R.D. van der Hilst, F.L. Vernon, V. Martynov, T. Cox, J. Eakins, L. Astiz, and G.L. Pavlis (2010), Model Update January 2010: Upper mantle heterogeneity beneath North America from travel time tomography with global and USArray Transportable Array data, *Seismol. Res. Lett.*, 81, 689–693.

Cammarano, F., S. Goes, P. Vacher, and D. Giardini (2003), Inferring upper mantle temperatures from seismic velocities, *Phys. Earth Planet. Inter*., 138, 197– 222.

Cao, A., and A. Levander (2010), High-resolution transition zone structures of the Gorda Slab beneath the western United States: Implication for deep water subduction, *J. Geophys. Res.,* 115, B07301.

Carlson, R.W., and W.K. Hart (1987), Crustal genesis on the Oregon Plateau, *J. Geophys. Res.,* 92, 6191–6206, doi:10.1029/JB092iB07p06191.

Carlson, R.W., D.E. James, M.J. Fouch, T.L. Grove, W.K. Hart, A.L. Grunder, R.A. Duncan, G.R. Keller, S.H. Harder, and C.R. Kincaid (2005), On the cause of voluminous magmatism in the northwestern United States, *Geol. Soc. Am. Abstr. Programs*, 37, 125.

Chulick, G.S., and W.D. Mooney (2002), Seismic structure of the crust and uppermost mantle of North America and adjacent oceanic basins: A synthesis, *Bull. Seismol. Soc. Am*., 92(6), 2478 – 2492, doi:10.1785/0120010188.

Cole, R.B., and A.R. Basu (1995), Nd-Sr Isotopic Geochemistry and Tectonics of Ridge Subduction and Middle Cenozoic Volcanism in Western California, *Geol. Soc. Am. Bull.*, *107*(2), 167-179.

Coney, P., and S. Reynolds (1977), Cordilleran benioff zones, *Nature*, 270, 403–406.

Cross, T.A., and R.H. Pilger (1982), Controls on subduction geometry, location of magmatic arcs, and tectonic arc and back-arc regions, *Geol. Soc. Am. Bull.*, 93, 545–562.

Crow R., K. Karlstrom, Y. Asmerom, B. Schmandt, V. Polyak, and S.A. DuFrane (2011), Shrinking of the Colorado Plateau via lithospheric mantle erosion: Evidence from Nd and Sr isotopes and geochronology of Neogene basalts, *Geology*, 39, 27-30, doi:10.1130/G31611.1.

Dalton, C.A., G. Ekström, and A.M. Dziewoński (2008), The global attenuation structure of the upper mantle, *J. Geophys. Res*., 113, B09303, doi:10.1029/2007JB005429.

Dickinson, W.R. (1997), Tectonic implications of Cenozoic volcanism in coastal California, *Geol. Soc. Am. Bull.*, *109*(8), 936-954.

Dickinson, W.R., and W.S. Snyder (1978), Plate tectonics of the Laramide Orogeny, in Laramide Folding Associated With Basement Block Faulting in the Western United States, edited by V. Matthews, *Mem. Geol. Soc. Am.,* 151, 355–366.

Dickinson, W.R., and W.S. Snyder (1979), Geometry of Subducted Slabs Related to San Andreas Transform, *J. Geol.*, *87*(6), 609-627.

Docherty, P. (1991), A brief comparison of some Kirchhoff integral formulas for migration and inversion, *Geophysics*, 56, 1164-l169.

Dueker, K.G., and A.F. Sheehan (1997), Mantle discontinuity structure from midpoint stacks of converted P to S waves across the Yellowstone hotspot track, *J. Geophys. Res.,* 102, 8313 – 8327.

Eagar, K.C., M.J. Fouch, D.E. James, and R.L. Carlson (2011), Crustal structure beneath the High Lava Plains of eastern Oregon and surrounding regions from receiver function analysis, *J. Geophys. Res.*, 116, B02313, doi:10.1029/2010JB007795.

Eakin, C.M., M. Obrebski, R.M. Allen, D.C. Boyarko, M.R. Brudzinski, and R. Porritt (2010), Seismic anisotropy beneath Cascadia and the Mendocino triple junction: Interaction of the subducting slab with mantle flow, *Earth Planet. Sc. Lett.*, *297*(3-4), 627-632.

Eaton, D.W., F. Darbyshire, R.L. Evans, H. Grütter, A.G. Jones, and X. Yuan (2009), The elusive lithosphere-asthenosphere boundary (LAB) beneath cratons, *Lithos*, 109 (1-2), 1-22.

Ekstrom, G., E.D. Humphreys, and A. Levander (1999), USArray - a tool for probing the continent, *IRIS Newsletter*, v.16, n.2, 2 & 4-6.

English, J.M., S.T. Johnston, and K.L. Wang (2003), Thermal modeling of the Laramide orogeny: testing the flat-slab subduction hypothesis, *Earth Planet. Sci. Lett*., 214, 619–632.

Faul, U.H., and I. Jackson (2005), The seismological signature of temperature and grain size variations in the upper mantle, *Earth Planet. Sci. Lett*., 234, 119–134.

Fischer, K.M., H.A. Ford, D.L. Abt, and C.A. Rychert (2010), The lithosphere-asthenosphere boundary, *Annu. Rev. Earth Planet. Sci*., 38, 551–575.

Forsyth, D.W., and A. Li (2005), Array analysis of two-dimensional variations in surface wave phase velocity and azimuthal anisotropy in the presence of multipathing interference, in *Seismic Earth: Array Analysis of Broadband Seismograms*, edited by A. Levander and G. Nolet, AGU, Washington, D. C.

Forsyth, D.W., Webb, S., Dorman, L. Shen, Y. (1998), Phase velocities of Rayleigh waves in the MELT experiment on the East Pacific Rise, *Science*, 280, 1235–1238.

Fouch, M.J., and J. West (in prep.), The mantle flow field beneath the western United States.

Frederiksen, A.W., and J. Revenaugh (2004), Lithospheric imaging via teleseismic scattering tomography, *Geophys. J. Int*., 159(3), 978-990.

Friederich, W., and E. Wielandt (1995), Interpretation of Seismic Surface-Waves in Regional Networks - Joint Estimation of Wave-Field Geometry and Local Phase-Velocity - Method and Numerical Tests, *Geophys. J. Int.*, *120*(3), 731-744.

Fulton, P.M., and D.M. Saffer (2009), Potential role of mantle-derived fluids in weakening the San Andreas Fault, *J. Geophys. Res.*, 114.

Furlong, K.P. , and R. Govers (1999), Ephemeral Crustal Thickening at a Triple Junction: The Mendocino crustal conveyor, *Geology*, 27, 127-130.

Furlong, K.P., and S.Y. Schwartz (2004), Influence of the Mendocino triple junction on the tectonics of coastal California, *Annu. Rev. Earth Pl. Sc.*, *32*, 403-433.

Furlong, K.P., J. Lock, C. Guzofski, J. Whitlock, and H. Benz (2003), The Mendocino crustal conveyor: Making and breaking the California crust, *Int. Geol. Rev.*, *45*(9), 767-779.

Gao, W., S.P. Grand, W.S. Baldridge, D. Wilson, M. West, J.F. Ni, and R. Aster (2004), Upper mantle convection beneath the central Rio Grande rift imaged by P and S wave tomography, *J. Geophys. Res*, 109, B03305, doi:10.1029/2003JB002743.

Gilbert, H.J., and A.F. Sheehan (2004), Images of crustal variations in the intermountain west, *J. Geophys. Res.*, 109, B03306, doi:10.1029/2003JB002730.

Gilbert, H., A.A. Velasco, and G. Zandt (2007), Preservation of Proterozoic terrane boundaries within the Colorado Plateau and implications for its tectonic evolution, *Earth Planet. Sci. Lett.*, 258 (1-2), 237-248. doi: 10.1016/j.epsl.2007.03.034.

Godfrey, N.J., and S.L. Klemperer (1998), Ophiolitic basement to a forearc basin and implications for continental growth: The Coast Range Great Valley ophiolite, California, *Tectonics*, *17*(4), 558-570.

Godfrey, N.J., B.C. Beaudoin, and S.L. Klemperer (1997), Ophiolitic basement to the Great Valley forearc basin, California, from seismic and gravity data: Implications for crustal growth at the North American continental margin, *Geol. Soc. Am. Bull.*, *109*(12), 1536-1562.

Grand, S.P., and D.V. Helmberger (1984), Upper mantle shear structure of North America, *Geophys. J. R. Astron. Soc.*, 76, 399–438.

Gulick, S.P. S., A.S. Meltzer, T.J. Henstock, and A. Levander (2001), Internal deformation of the southern Gorda plate: Fragmentation of a weak plate near the Mendocino triple junction, *Geology*, *29*(8), 691-694.

Guzofski, C., and Furlong, K.P. (2002), Migration of the Mendocino triple junction and ephemeral crustal deformation: Implications for California Coast Range heat flow, *Geophys. Res. Lett*., 29, 12-1 – 12-4.

Hacker, B.R., Peacock, S.M., Abers, G.A., Holloway, S.D. (2003), Subduction factory, 2, Are intermediate-depth earthquakes in subducting slabs linked to metamorphic dehydration reactions?, *J. Geophys. Res.*, 108(B1), 2030, doi:10.1029/2001JB001129.

Hales, T.C., D.L. Abt, E.D. Humphreys, and J.J. Roering (2005), A lithospheric instability origin for Columbia River flood basalts and Wallowa Mountains uplift in northeast Oregon, *Nature*, 438, 842–845, doi:10.1038/nature04313.

Hammond, W.C., and E.D. Humphreys (2000), Upper mantle seismic wave velocity: Effects of realistic partial melt geometries, *J. Geophys. Res.,* 105(B5), 10,975–10,986.

Hansen, S., and K. Dueker (2009), P- and S-wave receiver function images of crustal imbrication beneath the Cheyenne belt in south-east Wyoming, *Bull. Seismol. Soc. Am.*, 99, 1953–1961, doi:10.1785/0120080168.

Hanson-Hedgecock, S, L.S. Wagner, M.J. Fouch, and D.E. James (2012), Constraints on the causes of mid-Miocene volcanism in the Pacific Northwest US from ambient noise tomography, *Geophys. Res. Lett*., 39, doi:10.1029/2012GL051108.

Henstock, T.J., and A. Levander (2000), Lithospheric evolution in the wake of the Mendocino triple junction: structure of the San Andreas Fault system at 2 Ma, *Geophys. J. Int.*, *140*(1), 233-247.

Henstock, T.J., A. Levander, and J.A. Hole (1997), Deformation in the lower crust of the San Andreas fault system in northern California, *Science*, *278*(5338), 650-653.

Henstock, T., and the Deep Probe Working Group (1998), Probing the Archean and Proterozoic lithosphere of western North America, *GSA Today,* 8, 1-17.

Herrmann, R.B., and C.J. Ammon (2002), Surface waves, receiver functions and crustal structure, *Computer Program in Seismology*.

Hole, J.A., B.C. Beaudoin, and T.J. Henstock (1998), Wide-angle seismic constraints on the evolution of the deep San Andreas plate boundary by Mendocino triple junction migration, *Tectonics*, *17*(5), 802-818.

Humphreys, E.D. (1995), Post-Laramide removal of the Farallon slab, western United States, *Geology*, 23, 987–990.

Humphreys, E.D. (2009), Relation of flat subduction to magmatism and deformation in the western United States, *Geological Society of America Memoirs*, 204, 85-98.

Humphreys, E.D., and Dueker, K.G. (1994), Western U.S. upper mantle structure, *J. Geophys. Res.,* 99, 9615-9634.

Humphreys E., E. Hessler, K. Dueker, E. Erslev, G.L. Farmer, and T. Atwater (2003), How Laramideage hydration of North America by the Farallon slab controlled subsequent activity in the Western U.S, *Int. Geol. Rev.,* 45*,* 575– 595.

Hyndman, R.D., C.A. Currie, and S.P. Mazzotti (2005), Subduction zone backarcs, mobile belts, and orogenic heat, *GSA Today*, 15, 4-10.

James, D.E., M.J. Fouch, R.W. Carlson, and J.B. Roth (2011), Slab fragmentation, edge flow and the origin of the Yellowstone hotspot track, *Earth Planet. Sci. Lett*., 311, 124–135.

Johnson, C.M., and J.R. O'Neil (1984), Triple junction magmatism: a geochemical study of Neogene volcanic rocks in western California, *Earth Planet. Sc. Lett.*, *71*(2), 241-262.

Jordan, B.T., A.L. Grunder, R.A. Duncan, and A.L. Deino (2004), Geochronology of ageprogressive volcanism of the Oregon High Lava Plains: implications for the plume interpretation of Yellowstone*, J. Geophys. Res.*, 109, B10202. doi:10.1029/2003JB002776.

Julia, J., C.J. Ammon, R.B. Herrmann, and A.M. Correig (2000), Joint inversion of receiver function and surface wave dispersion observations, *Geophys. J. Int.*, *143*(1), 99-112.

Karato, S. (1993), Importance of anelasticity in the interpretation of seismic tomography, *Geophys. Res. Lett*., 20, 1623–1626.

Karato, S.I., and H. Jung (1998), Water, partial melting and the origin of the seismic low velocity and high attenuation zone in the upper mantle, *Earth Planet. Sci. Lett*., 157, 193–207.

Karlstrom, K.E., and G. Humphreys (1998), Influence of Proterozoic accretionary boundaries in the tectonic evolution of western North America: Interaction of cratonic grain and mantle modification events, *Rocky Mountain Geology*, 33(2), 161-179.

Karlstrom, K.E., R. Crow, L.J. Crossey, D. Coblentz, and J. van Wijk (2008), Model for tectonically driven incision of the less than 6 Ma Grand Canyon, *Geology*, 36(11), 835-838.

Kawakatsu, H., P. Kumar, Y. Takei, M. Shinohara, T. Kanazawa, E. Araki, and K. Suyehiro (2009), Seismic Evidence for Sharp Lithosphere-Asthenosphere Boundaries of Oceanic Plates, *Science*, *324*(5926), 499-502.

Kennett, B.L.N. (1991), The removal of free surface interactions from three-component seismograms, *Geophys. J. Int*., 104, 153–163.

Kennett, B.L.N., and E.R. Engdahl (1991), Travel times for global earthquake location and phase association, *Geophys. J. Int.,* 105, 429-465.

King, S.D., and D.L. Anderson (1998), Edge-Driven Convection, *Earth Planet. Sci. Lett*., 160, 289-296.

Kumar, P., X. Yuan, R. Kind, G. Kosarev (2005), The lithosphere-asthenosphere boundary in the Tien Shan-Karakoram region from S receiver functions: Evidence for continental subduction, *Geophys. Res. Lett.*, 32, L07305.

Lachenbruch, A. H., and J. H. Sass (1980), Heat-Flow and Energetics of the San-Andreas Fault Zone, *J. Geophys. Res.*, *85*(Nb11), 6185-6222.

Langston, C.A. (1979), Structure under Mount Rainier, Washington, inferred from teleseismic body waves, *J. Geophys. Res*., 84, 4749-4762.

Larsen, S.C., and D.B. Harris (1993), Seismic wave propagation through a low velocity nuclear rubble zone, *UCRL-ID-115729*.

Lastowka, L.A., A.F. Sheehan, and J.M. Schneider (2001), Seismic evidence for partial delamination model for Colorado Plateau uplift, *Geophys. Res. Lett*., 28, 1319–1322.

Lee, C.-T. A. (2005), Trace element evidence for hydrous metasomatism at the base of the North American Lithosphere and possible association with Laramide low-angle subduction, *J. Geol.*, 113, 673–685, doi:10.1086/449327.

Lee, C.-T., Q. Yin, R.L. Rudnick, and S.B. Jacobsen (2001), Preservation of ancient and fertile lithospheric mantle beneath the southwestern United States, *Nature*, 411, 69–73.

Leeman, W., J. Lewis, R. Evarts, R. Conrey, and M. Streck (2005), Petrologic constraints on the thermal structure of the Cascades arc, *J. Volcanol. Geoth. Res.*, 140(1-3), 67-105.

Levander, A. (1988), Fourth-order finite-difference P-SV seismograms, *Geophysics*, 53, 1425-1436.

Levander, A., and M.S. Miller, Evolutionary aspects of lithosphere discontinuity structure in the western U.S., *Geochem. Geophys. Geosyst.*, submitted.

Levander, A., T.J. Henstock, A.S. Meltzer, B.C. Beaudoin, A.M. Trehu, and S.L. Klemperer (1998), Fluids in the lower crust following Mendocino triple junction migration: Active basaltic intrusion?, *Geology*, *26*(2), 171-174.

Levander, A., E. Humphreys, G. Ekstrom, A. Meltzer, and P. Shearer (1999), Proposed project would give unprecedented look under North America, *Eos Trans. AGU*, 80(22), 245.

Levander, A., F. Niu, and W.W. Symes (2005), Imaging teleseismic P to S scattered waves using the Kirchhoff integral, in: A. Levander, G. Nolet (Eds.), *Array Analysis of Broadband Seismograms, AGU*, 149– 170.

Levander, A., C.A. Zelt, and M.B. Magnani (2005), Crust and upper mantle velocity structure of the Southern Rocky Mountains from the Jemez Lineament to the Cheyenne Belt, in K. Karlstrom and G.R. Keller, eds., The Rocky Mountain Region: An Evolving Lithosphere, *Geophysical Monograph Series* 154, AGU, Washington, D.C., 293-308.

Levander, A., F. Niu, C.-T.A. Lee, and X. Cheng (2006), Imag(in)ing the Continental Lithosphere, *Tectonophysics*, 416, 167-185.

Levander, A., B. Schmandt, M.S. Miller, K. Liu, K.E. Karlstrom, R.S. Crow, C.-T.A. Lee, and E.D. Humphreys (2011), Continuing Colorado plateau uplift by delamination-style convective lithospheric downwelling, *Nature*, 472, 461-465, doi:10.1038/nature10001.

Li, A., D.W. Forsyth, and K.M. Fischer (2003), Shear velocity structure and azimuthal anisotropy beneath eastern North America from Rayleigh wave inversion, *J. Geophys. Res.,* 108(B8), 2362.

Li, A., D.W. Forsyth, and K.M. Fischer (2005), Rayleigh wave constraints on shear-wave structure and azimuthal anisotropy beneath the Colorado Rocky Mountains, in *The Rocky*

Mountain Region: An Evolving Lithosphere, eds Karlstrom, K.E. Keller, G.R., 385–401, *Geophys. Monogr.*, 154, AGU, Washington DC.

Li, X, X. Yuan, and R. Kind (2007), The lithosphere-asthenosphere boundary beneath the western United States, *Geophys. J. Int.,*170:700–10.

Li, Z., C.-T. Lee, A. Peslier, A. Lenardic, and S. Mackwell (2008), Water contents in mantle xenoliths from the Colorado Plateau and vicinity: Implications for the mantle rheology and hydration-induced thinning of continental lithosphere, *J. Geophys. Res*., 113, B09210.

Ligorria, J.P., and C.J. Ammon (1999), Iterative deconvolution and receiver-function estimation, *B. Seismol. Soc. Am.*, *89*(5), 1395-1400.

Lin, F.C. and M.H. Ritzwoller (2011), Helmholtz surface wave tomography for isotropic and azimuthally anisotropic structure, *Geophys. J. Int*., 186, 1104-1120.

Lin, F.C., M.H. Ritzwoller, and R. Snieder (2009), Eikonal Tomography: surface wave tomography by phase-front tracking across a regional broad-band seismic array, *Geophys. J. Int*., 177(3), 1091-1110.

Lipman, P.W. (1992), Magmatism in the Cordilleran United States: Progress and problems, in *The Geology of North America, vol. G3, The Cordilleran Orogen, Conterminous U.S*., edited by B.C. Burchfiel, P.W. Lipman, and M.L. Zoback, 481–514, GSA, Boulder, Colo.

Liu, K.H. (2009), NA-SWS-1.1: A uniform database of teleseismic shear wave splitting measurements for North America, *Geochem. Geophy. Geosy.*, *10*.

Liu, M., and K.P. Furlong (1992), Cenozoic Volcanism in the California Coast Ranges - Numerical-Solutions, *J. Geophys. Res.*, *97*(B4), 4941-4951.

Liu, K., A. Levander, F. Niu, and M.S. Miller (2011), Imaging crustal and upper mantle structure beneath the Colorado Plateau using finite frequency Rayleigh wave tomography, *Geochem. Geophy. Geosy.*, *12*.

Liu, K., A. Levander, Y. Zhai, R.W. Porritt, and R.M. Allen (2012), Asthenospheric flow and lithospheric evolution near the Mendocino Triple Junction, *Earth Planet. Sci. Lett*., 323, 60-71, doi: 10.1016/j.epsl.2012.01.020.

Liu, L., M. Gurnis, M. Seton, J. Saleeby, R.D. Muller, and J. Jackson (2010), The role of oceanic plateau subduction in the Laramide Orogeny, *Nat. Geosci.*, 3, 353-357.

Madariaga, R. (1976), Dynamics of an expanding circular fault, *Bull. Seism. Soc. Am*., 66, 639-666.

McCarthy J., and T. Parsons (1994), Insights into the kinematic and Cenozoic evolution of the Basin and Range–Colorado Plateau transition from coincident seismic refraction and reflection data, *Geol. Soc. Am. Bull*., 106, 747–759.

McCarthy, J., S.P. Larkin, G.S. Fuis, R.W. Simpson, and K.A. Howard (1991), Anatomy of a Metamorphic Core Complex: Seismic Refraction/Wide-Angle Reflection Profiling in Southeastern California and Western Arizona, *J. Geophys. Res*., 96(B7), 12,259–12,291.

McQuarrie, N., and C.G. Chase (2000), Raising the Colorado Plateau, *Geology*, 28, 91–94.

Meigs, A., *et al.* (2009), Geological and geophysical perspectives on the magmatic and tectonic development, High Lava Plains and northwest Basin and Range, in *Volcanoes to Vineyards: Geologic Field Trips Through the Dynamic Landscape of the Pacific Northwest*, edited by J.E. O'Connor, R.J. Dorsey, and I.P. Madin, 435–470, *GSA.,* Boulder, Colo.

Meltzer, A, R. Rudnick, P. Zeitler, A. Levander, E.D. Humphreys, K. Karlstrom, G. Ekström, R. Carlson, T. Dixon, M. Gurnis, P. Shearer, and R. van der Hilst (1999), The USArray Initiative, *GSA Today*, 9, 8-10.

Mercier, J.-P., M.G. Bostock, and A.M. Baig (2006), Improved Green's functions for passive source structural studies, *Geophysics*, 71(4), SI95–SI102, doi:10.1190/1.2213951.

Miller, D., M. Oristaglio, and G. Beylkin (1987), A new slant on seismic imaging: Migration and integral geometry, *Geophysics*, 52, 943–964.

Miller, M.S., A. Levander, F. Niu, and A. Li (2009), Upper mantle structure beneath the Caribbean–South American plate boundary from surface wave tomography, *J. Geophys. Res*., 114, B01312.

Mitchell, B.J. (1995), Anelastic structure and evolution of the continental crust and upper mantle from seismic surface wave attenuation, *Rev. Geophys*., 33, 441–462.

Morgan, P., and C. Swanberg (1985), On the Cenozoic uplift and tectonic stability of the Colorado Plateau, *J. Geodyn*., 3, 39–63.

Morse, P. M., and H. Feshbach (1953), Methods of Theoretical Physics, *McGraw-Hill*, New York.

Moschetti, M.P., M.H. Ritzwoller, F. Lin and Y. Yang (2010), Seismic evidence for widespread western-US deep-crustal deformation caused by extension, *Nature*, 464, 885-889.

Moucha, R., A.M. Forte, D.B. Rowley, J.X. Mitrovica, N.A. Simmons and S.P. Grand (2008), Mantle convection and the recent evolution of the Colorado Plateau and the Rio Grande Rift valley, *Geology*, 36, 439–442.

Moucha, R., A. Forte, D.B. Rowley, J.X. Mitrovica, N.A. Simmons, and S.P. Grand (2009), Deep mantle forces and the uplift of the Colorado Plateau, *Geophys. Res. Lett.*, 36, L19310.

Nabelek, J., X. Li, S. Azevedo, J. Braunmiller, A. Fabritius, B. Leimer, A.M. Tréhu, and G. Zandt (1993), A high-resolution image of the Cascadia subduction zone from teleseismic converted phases recorded by a broad-band seismic array, *EOS, Trans. AGU*, 74 (43), 431.

Nowack, R.L., W.P. Chen and T.L. Tseng (2010), Application of Gaussian beam migration to multi-scale imaging of the lithosphere beneath the Hi-CLIMB array in Tibet, *Bull. Seis. Soc. Am.*, 100, 1743-1754.

Obrebski, M., R.M. Allen, M. Xue, and S.-H. Hung (2010), Slab-plume interaction beneath the Pacific Northwest, *Geophys. Res. Lett*., 37, L14305, doi:10.1029/2010GL043489.

Obrebski, M., R.M. Allen, F. Pollitz, and S.-H. Hung (2011), Lithosphere-asthenosphere interaction beneath the western United States from the joint inversion of body-wave traveltimes and surface-wave phase velocities, *Geophys. J. Int*., 185, 1003–1021.

Pao, Y.-H. and V. Varatharajulu (1976), Huygens' principle, radiation conditions and integral formulas for the scattering of elastic waves, *J. acoust. Soc. Am*., 59, 1361–1371.

Parsons, T., J. McCarthy, W.M. Kohler, C.J. Ammon, H.M. Benz, J.A. Hole, and E.E. Criley (1996), Crustal structure of the Colorado Plateau, Arizona: Application of new long-offset seismic data analysis techniques, *J. Geophys. Res*., 101, 11,173–11,194.

Pavlis, G.L. (2005), Direct imaging of the coda of teleseismic P waves, in *Seismic Earth: Array analysis of broadband seismograms*, edited by A. Levander and G. Nolet, AGU, Geophysical Monograph, 157, p. 171–185.

Pavlis, G. L. (2011), Three-dimensional wavefield imaging of data from the USArray: New constraints on the geometry of the Farallon slab, *Geosphere*, 7(3), 785-801.

Pierce, K.L., and L.A. Morgan (2009), Is the track of the Yellowstone hotspot driven by a deep mantle plume? — Review of volcanism, faulting, and uplift in light of new data, *J. of Volcanol. Geoth. Res.*, 188:1-25.

Piromallo, C., T.W. Becker, F. Funiciello, C. Faccenna (2006), Three-dimensional instantaneous mantle flow induced by subduction, *Geophys. Res. Lett*., 33, L08304.

Pollitz, F. (2008), Observations and interpretation of fundamental-mode Rayleigh wavefields recorded by the Transportable Array (USArray), *J. Geophys. Res*., 113, B10311.

Pollitz, F.F., and J.A. Snoke (2010), Rayleigh-wave phase-velocity maps and three-dimensional shear velocity structure of the western US from local non-plane surface wave tomography, *Geophys. J. Int*., 180, 1153–1169, doi:10.1111/j.1365-246X.2009.04441.x.

Poppeliers, C., and G.L. Pavlis (2003a), Three-dimensional, prestack, plane wave migration of teleseismic P-to-S converted phases: 1. Theory, *J. Geophys. Res*., 108(B2), 2112.

Poppeliers, C., and G.L. Pavlis (2003b), Three-dimensional, prestack, plane wave migration of teleseismic P-to-S converted phases: 2. Stacking multiple events, *J. Geophys. Res*., 108(B5), 2267, doi:10.1029/2001JB001583.

Porritt, R.W., Allen, R.M., Boyarko, D.C., Brudzinski, M.R. (2011), Investigation of Cascadia Segmentation with Ambient Noise Tomography, *Earth Planet. Sc. Lett.* 309, 67-76.

Reading, A., B. Kennett, and M. Sambridge (2003), Improved inversion for seismic structure using transformed, S-wavevector receiver functions: Removing the effect of the free surface, *Geophys. Res. Lett*., 30(19), 1981, doi:10.1029/2003GL018090.

Reid, M.R., R.A. Bouchet, J. Blichert-Toft, A. Levander, K. Liu, M.S. Miller, and F.C. Ramos (2012), Melting under the Colorado Plateau, USA, *Geology*.

Riter, J., and D. Smith (1996), Xenolith constraints on the thermal history of the mantle below the Colorado Plateau, *Geology*, 24, 267–270.

Rondenay, S. (2009), Upper Mantle Imaging with Array Recordings of Converted and Scattered Teleseismic Waves, *Surv Geophys*, *30*(4-5), 377-405.

Rondenay, S., M.G. Bostock, and K.M. Fischer (2005), Multichannel Inversion of Scattered Teleseismic Body Waves: Practical Considerations and Applicability. in: A. Levander, G. Nolet (Eds.), *Array Analysis of Broadband Seismograms*, AGU, 205– 228.

Roth, J.B., M.J. Fouch, D.E. James, and R.W. Carlson (2008), Three-dimensional seismic velocity structure of the northwestern United States, *Geophys. Res. Lett*., 35, L15304.

Roy, M., T.H. Jordan, and J.L. Pederson (2009), Colorado Plateau magmatism and uplift by warming of heterogeneous lithosphere, *Nature*, 459, 978–982, doi:10.1038/nature08052.

Ryberg, T., and M. Weber (2000), Receiver function arrays: A reflection seismic approach, *Geophys. J. Int*., 141, 1–11.

Rychert, C.A., and P.M. Shearer (2009), A global view of the lithosphere-asthenosphere boundary, *Science*, 324, 495–498.

Saito, M. (1988), DISPER80: a subroutine package for the calculation of seismic normal-mode solutions, in: *Seismological Algorithms, Computational Methods and Computer Programs*, *Academic Press*, New York, 293–319.

Saleeby, J. (2003), Segmentation of the Laramide Slab - evidence from the southern Sierra Nevada region, *Geol. Soc. Am. Bull*., 115, 655-668.

Schmandt, B., and E. Humphreys (2010), Complex subduction and small-scale convection revealed by body-wave tomography of the western United States upper mantle, *Earth Planet. Sci. Lett.*, 297, 435-445. doi:10.1016/j.epsl.2010.06.047.
Schmandt, B., K.G. Dueker, S.M. Hansen, J.J. Jasbinsek, and Z. Zhang (2011), A sporadic low-velocity layer atop the western U.S. mantle transition zone and short-wavelength variations in transition zone discontinuities, *Geochem. Geophys. Geosyst*., 12, Q08014.

Schmitt, A.K., R.L. Romer, and J.A. Stimac (2006), Geochemistry of volcanic rocks from the Geysers geothermal area, California Coast Ranges, *Lithos*, *87*(1-2), 80-103.

Schutt, D., and C. Lesher (2006), Effects of melt depletion on the density and seismic velocity of garnet and spinel lherzolite, *J. Geophys. Res*., 111, B05401.

Schutt, D.L., K. Dueker, and H. Yuan (2008), Crust and upper mantle velocity structure of the Yellowstone hot spot and surroundings, *J. Geophys. Res*., 113, B03310.

Shapiro, N.M., M. Campillo, L. Stehly, and M.H. Ritzwoller (2005), High-resolution surface-wave tomography from ambient seismic noise, *Science*, *307*(5715), 1615-1618.

Sheehan, A.F., G.A. Abers, A.L. Lerner-Lam, and C.H. Jones (1995), Crustal thickness variations across the Colorado Rocky Mountains from teleseismic receiver functions, *J. Geophys. Res*., 100, 20,391–20,404.

Sheehan, A.F., C.H. Jones, M.K. Savage, S. Ozalabey, and J. Schneider (1997), Contrasting lithosphere structure between the Colorado Plateau and the Great Basin: Initial results from Colorado Plateau-Great Basin PASSCAL experiment, *Geophys. Res. Lett.*, 242609–242612.

Shoemaker, K. (2004), The tectonomagmatic evolution of the late Cenozoic Owyhee Plateau, northwestern United States, *PhD dissertation*, Dep. of Geol., Miami Univ., Oxford, Ohio.

Shragge, J., S. Rondenay, and M.G. Bostock (2001), Multi-parameter 2-D inversion of scattered teleseismic body-waves—II. Numerical examples, *J. Geophys. Res*., 106, 30 783–793.

Sigloch, K. (2011), Mantle provinces under North America from multifrequency P wave tomography, *Geochem. Geophys. Geosyst*., 12, Q02W08, doi:10.1029/2010GC003421.

Sigloch, K., N. McQuarrie, and G. Nolet (2008), Two-stage subduction history under North America inferred from multiple-frequency tomography, *Nat. Geosci*., 1, 458–462.

Sine, C., D. Wilson, W. Gao, S.P. Grand, R. Aster, J. Ni, and W.S. Baldridge (2008), Mantle structure beneath the western edge of the Colorado Plateau*, Geophys. Res. Lett*., 35, L10303.

Smith, R.B., M. Jordan, B. Steinberger, C.M. Puskas, J. Farrell, G.P. Waite, S. Husen, W. Chang, and R. O'Connell (2009), Geodynamics of the Yellowstone hotspot and mantle

plume, Seismic and GPS imaging, kinematics, and mantle flow, *J. Volcanol. Geotherm. Res*., 188, 26–56, doi:10.1016/j.jvolgeores.2009.08.020.

Snelson, C.M., T.J. Henstock, G.R. Keller, K.C. Miller, and A. Levander (1998), Crustal and uppermost mantle structure along the Deep Probe seismic profile, *Rocky Mt. Geol*., 33, 181–198.

Snelson, C.M., G.R. Keller, K.C. Miller, H.-M. Rumpel, and C. Prodehl (2005), Regional crustal structure derived from the CD-ROM 99 seismic refraction/wide-angle reflection profile: the lower crust and upper mantle, in *The Rocky Mountain Region—An Evolving Lithosphere: Tectonics, Geochemistry, and Geophysics,* K.E. Karlstrom and G.R. Keller (Editors), AGU, Washington, D.C., 271-291.

Snieder, R. (2004), Extracting the Green's function from the correlation of coda waves: A derivation based on stationary phase, *Phys. Rev. E.*, *69*(4).

Snyder W.S., W.R. Dickinson, and M.L. Silberman (1976), Tectonic implications of space-time patterns of Cenozoic magmatism in the western United States, *Earth Planet. Sci. Lett.,* 32, 91–106.

Spencer, J.E. (1996), Uplift of the Colorado Plateau due to lithosphere attenuation during Laramide low-angle subduction, *J. Geophys. Res.,*101, 13,595-13,609.

Takei, Y. (2000), Acoustic properties of partially molten media studied on a simple binary system with a controllable dihedral angle, *J. Geophys. Res.*, 105(B7), 16,665–16,682.

Tarantola, A., and B. Valette (1982), Generalized non-linear problems solved using the least-squares criterion, *Rev. Geophys. Sp. Phys*., 20, 219–232.

Thompson, G.A., and M.L. Zoback (1979), Regional geophysics of the Colorado Plateau, *Tectonophysics*, 61, 149–181.

Thurber, C., H.J. Zhang, T. Brocher, and V. Langenheim (2009), Regional three-dimensional seismic velocity model of the crust and uppermost mantle of northern California, *J. Geophys. Res.*, *114*.

Tian, Y., Y. Zhou, K. Sigloch, G. Nolet, and G. Laske (2011), Structure of North American mantle constrained by simultaneous inversion of multiple-frequency SH, SS, and Love waves, *J. Geophys. Res*., 116, B02307, doi:10.1029/2010JB007704.

Trehu, A.M., I. Asudeh, T.M. Broher, J.H. Luetgert, W.D. Mooney, J.I. Nabelek, and Y. Nakamura (1994), Crustal architecture of the Cascadia Forearc, *Science*, 266, 237–243.

van der Lee, S., and G. Nolet (1997), Upper mantle S-velocity structure of North America, *J. Geophys. Res*., 102, 22,815–22,838.

van Wijk, J., J. Van Hunen, S. Goes (2008), Small-scale convection during continental rifting: evidence from the Rio Grande rift, *Geology*, 36, 575–578.

van Wijk, J., W. Baldridge, J. van Hunen, S. Goes, R. Aster, D. Coblentz, S.P. Grand, and J. Ni (2010), Small-scale convection at the edge of the Colorado Plateau; implications for topography, magmatism, and evolution of Proterozoic lithosphere, *Geology*, 38 (7), 611-614.

Vinnik, L.P. (1977), Detection of waves converted from P to SV in the mantle, *Phys. Earth Planet. Inter.*, 15, 39-45.

Wagner, L.S., D.W. Forsyth, M.J. Fouch, and D.E. James (2010), Detailed three-dimensional shear wave velocity structure of the northwestern United States from Rayleigh wave tomography, *Earth Planet. Sci. Lett.,* 299, 273–284, doi:10.1016/j.epsl.2010.09.005.

West, M., J. Ni, W. Baldridge, D. Wilson, R. Aster, W. Gao, and S. Grand (2004), Crust and upper mantle shear-wave structure of the southwest United States: Implications for rifting and support for high elevation, *J. Geophys. Res*., 109, B03309, doi:10.1029/2003JB002575.

West, J.D., M.J. Fouch, J.B. Roth, and L.T. Elkins-Tanton (2009), Vertical mantle flow associated with a lithospheric drip beneath the Great Basin, *Nat. Geosci*., 2.

Whitlock, J.S., K.P. Furlong, C.E. Lesher, and T. Furman (2001), The Juan de Fuca Slab-window and Coast Range Volcanics, California: correlation between subducted slab age and mantle wedge geochemistry, *EOS Trans. AGU,* 82:F1186 (Abstr.).

Wilson, D., and R. Aster (2005), Seismic imaging of the crust and uppermantle using regularized joint receiver functions,frequency.wave number filtering, and multimode Kirchhoff migration, *J. Geophys. Res.*, 110, B05305, doi:10.1029/2004JB003430.

Wilson, D., R. Aster, J. Ni, S. Grand, M. West, W. Gao, W.S. Baldridge, S. Semken (2005a), Imaging the seismic structure of the crust and upper mantle beneath the Great Plains, Rio Grande Rift, and Colorado Plateau using receiver functions, *J. Geophys. Res*., 110, B05306.

Wilson, D., R. Aster, M. West, J. Ni, S. Grand, W. Gao, W. Baldridge, S. Semken, and P. Patel (2005b), Lithospheric structure of the Rio Grande rift, *Nature*, 433, 851–855.

Wilson, D.C., R. Aster, S. Grand, J. Ni, and W.S. Baldridge (2010), High-resolution receiver function imaging reveals Colorado Plateau lithospheric architecture and mantle-supported topography, *Geophys. Res. Lett.*, *37*, L20313, doi:10.1029/2010GL044799.

Wolf, L.W., and J.J. Cipar (1993), Through thick and thin: a new model for the Colorado plateau from seismic refraction data from Pacific to Arizona crustal experiment*, J. Geophys. Res.*, *98*, 19881–19894.

Yang, Y. and D.W. Forsyth (2006a), Rayleigh wave phase velocities, small-scale convection, and azimuthal anisotropy beneath southern California, *J. Geophys. Res*., 111, B07306.

Yang, Y., and D.W. Forsyth (2006b), Regional tomographic inversion of amplitude and phase of Rayleigh waves with 2-D sensitivity kernels, *Geophys. J. Int*., 166, 1148–1160.

Yang Y., and D.W. Forsyth (2008), Attenuation in the upper mantle beneath Southern California: physical state of the lithosphere and asthenosphere, *J. Geophys. Res.*, 113, B03308, doi:10.1029/2007JB005118.

Yang, Y., and M.H. Ritzwoller (2008), Teleseismic surface wave tomography in the western U.S. using the Transportable Array component of USArray, *Geophys. Res. Lett*., 35, L04308.

Yang, Y., M. H. Ritzwoller, F.-C. Lin, M. P. Moschetti, and N. M. Shapiro (2008), Structure of the crust and uppermost mantle beneath the western United States revealed by ambient noise and earthquake tomography, *J. Geophys. Res*., 113, B12310.

Yao, H.J., R.D. van der Hilst, and M.V. de Hoop (2006), Surface-wave array tomography in SE Tibet from ambient seismic noise and two-station analysis - I. Phase velocity maps, *Geophys. J. Int.*, *166*(2), 732-744.

Yuan, H. and B. Romanowicz (2010), Lithospheric Layering in the North American Continent, *Nature*, 466, 1063-1069.

Zandt, G., and K.P. Furlong (1982), Evolution and Thickness of the Lithosphere beneath Coastal California, *Geology*, *10*(7), 376-381.

Zandt, G., and E. Humphreys (2008), Toroidal mantle flow through the western US slab window, *Geology*, *36*(4), 295-298.

Zandt, G., S.C. Myers, and T.C. Wallace (1995), Crust and mantle structure across the Basin and Range-Colorado Plateau boundary at 37°N latitude and implications for Cenozoic extensional mechanism, *J. Geophys. Res*., 100, 10,529–10,548, doi:10.1029/94JB03063.

Zandt, G., H. Gilbert, T.J. Owens, M. Ducea, J. Saleeby, C.H. Jones (2004), Active Foundering of a Continental Arc Root Beneath the Southern Sierra Nevada, California, *Nature* 432, 41-46.

Zhai, Y. (2010), The Lithospheric Structure of the Mendocino Triple Junction: Implications of Receiver Function Analysis, *Master thesis*, Rice University, Houston.

Zhou, Y., F.A. Dahlen, and G. Nolet (2004), Three-dimensional sensitivity kernels for surface wave observables, *Geophys. J. Int.*, *158*(1), 142-168.

Zucca, J.J., G.S. Fuis, B. Milkereit, W.D. Mooney, and R.D. Catchings (1986), Crustal Structure of Northeastern California, *J. Geophys. Res.*, *91*(B7), 7359-7382.